NOVEL CAVITIES IN ULTRAFAST VERTICAL EXTERNAL CAVITY SURFACE EMITTING LASERS FOR HIGH POWER HARMONIC GENERATION

By

Jason T. Meyer

A Dissertation Submitted to the Faculty of the

JAMES C. WYANT COLLEGE OF OPTICAL SCIENCES

In Partial Fulfillment of the Requirements

For the Degree of

DOCTOR OF PHILOSOPHY

In the Graduate College

THE UNIVERSITY OF ARIZONA

2021

THE UNIVERSITY OF ARIZONA
GRADUATE COLLEGE

As members of the Dissertation Committee, we certify that we have read the dissertation prepared by **Jason Timothy Meyer**, titled *Novel Cavities in Ultrafast Vertical External Cavity Surface Emitting Lasers for High Power Harmonic Generation* and recommend that it be accepted as fulfilling the dissertation requirement for the Degree of Doctor of Philosophy.

_____*M.Fallahi*_____ Date: _5/5/21_____
Professor Mahmoud Fallahi

_____*Stanley K H Pau*_____ Date: __5/5/21_____
Professor Stanley K. H. Pau

____Ewan M. Wright_____ Date: _5/5/21____
Professor Ewan M. Wright

_____*Chris Hessenius*_____ Date: ___5/5/21____
Professor Chris A. Hessenius

Final approval and acceptance of this dissertation is contingent upon the candidate's submission of the final copies of the dissertation to the Graduate College.

I hereby certify that I have read this dissertation prepared under my direction and recommend that it be accepted as fulfilling the dissertation requirement.

_____*M.Fallahi*_____ Date: _5/5/2021____
Professor Mahmoud Fallahi
Dissertation Committee Chair
Wyant College of Optical Sciences

Acknowledgements

This work is the culmination of nearly sixteen years spent in higher education. I have benefited from my experiences with so many individuals and I want to immediately offer my apologies to anyone that is missed that deserves to be mentioned.

First, I want to thank my wife, Jessica. Without your emotional support over these many years, I never would have gone this far in my academic pursuits. You forever have my unconditional love.

Second, I want to thank my mother, Mary Anne. Sixteen years ago, you told me to go to college and made the beginning of this entire journey possible. It's been quite the adventure since then, but I made it!

Third, I need to recognize the importance of Dr. Anthony Pitucco during my early years at Pima Community College. Your insanely difficult physics courses, ridiculous classroom antics, and demonizing of the "Muppets" gave me a focus and arrogance that was central to surviving the transition to university and my eventual doctoral studies. I speak often of my many experiences in your class.

I would also like to recognize Dr. Lonnie Burke, a chemistry professor at Pima Community College. You gave me the opportunity to become a tutor at a time when I was still very unsure of myself and it forced me to break out of my shell. You were the first to recognize that I was bound to get a doctorate. Well, I guess you were right!

To my committee members, Professor Mahmoud Fallahi, Professor Ewan M. Wright, Professor Stanley Pau, and Dr. Chris Hessenius... Thank you for taking the time to review and provide advice on this dissertation. I would also like to thank Mahmoud and Chris for providing me with all the research opportunities that have allowed me to develop my diverse skill set.

A special thanks goes to Ewan for the many semesters of independent studies and years of research discussions. You devoted a significant amount of time to my success and I greatly appreciate it.

For Michal L. Lukowski and Chris, thanks for the years of interesting discussions involving lasers, politics, sports, etc. It has been quite the ride in this lab group!

I also feel compelled to single out Roland Himmelhuber for all the time he spent helping me in the cleanroom with numerous annoying equipment failures. Thank you. You can throw away the Denton now. I don't need it anymore.

Now, for everyone else I am about to list, I would like to thank you for being a part of my academic life in some way, big or small, that gave me a new perspective, helped me grow professionally, or simply offered friendship during this long journey: Darryl Graham, Dale Karas, Allison Huff, Ameé Hennig, Majid Behabadi, Melissa Sarmiento, Gregg Curé, Soha Namnabat, Nathan Gottesman, Erica Bosset, the Manley family, and all the former tutors at PCC East Campus.

Dedication

For all the high school dropouts that didn't know where they would end up...

Contents

List of Figures

List of Tables

Abstract

Vertical external cavity surface emitting lasers (VECSELs) have seen tremendous growth and development over the the past twenty years since its initial demonstration. A key feature that has driven its development is the direct access to the external laser cavity. When combined with various cavity elements, these continuous wave semiconductor lasers can provide high output powers, tunability, high-quality diffraction-limited beams, and nonlinear frequency conversion to different spectral regions that are difficult, or impossible, to reach with more traditional laser technology. Passively mode locked, or ultrafast, VECSELs are able to combine many of the same features in ultrashort pulses with high output powers and fast repetition frequencies.

The vast majority of work that has been published on ultrafast VECSELs has been at its fundamental wavelength. This is in stark contrast to its continuous wave counterpart, which has seen nonlinear frequency conversion utilized to target spectral regions from the UV to mid-IR with excellent results. It is the primary objective of this dissertation to explore the combination of intracavity nonlinear frequency conversion with ultrafast VECSELs to achieve high peak power, ultrashort pulses in the visible and UV spectral regions. This work is concluded with a new wafer and cavity design for an ultrafast VECSEL for telecommunications applications and, finally, initial results are presented for an ultrafast VECSEL generating higher order Hermite-Gaussian modes.

This dissertation begins with an introduction to continuous wave VECSELs, including their origin and applications, semiconductor gain chip design, microfabrication process, and general operating principles. This is followed by an in-depth look at passive mode locking of VECSELs, the fundamentals and cavity design criteria that lead to stable mode locking, and the characterization of ultrashort pulses. The methods of resonator cavity design and pulse simulation are detailed, along with an introduction to second harmonic generation with ultrashort pulses and the dominant criteria for pulse broadening effects.

These introductory sections are followed by the demonstration of a record-setting ultrafast VECSEL utilizing intracavity second harmonic generation for high peak power, sub-picosecond pulse duration in the green spectral region. This was accomplished by careful optimization of the resonator cavity to satisfy key lasing parameters simultaneously. This work was then expanded upon with an overlapped cavity design that fully encloses the high peak power of the second harmonic within its own high Q resonator cavity for all-intracavity fourth harmonic generation into the UV spectral region.

This work is followed by a discussion and analysis of the gain chip design process and parameters for a new multi-quantum well wafer emitting in the 1550 nm spectral region that will be used in passively mode locked VECSELs. Finally, this dissertation concludes with the initial results for an ultrafast VECSEL generating higher order Hermite-Gaussian (HG) modes for conversion into Laguerre-Gaussian (LG) modes, with a brief discussion about future work to further develop this concept and combine it with other VECSEL technology for the next generation of laser systems.

Chapter 1

Introduction to VECSELs

1.1   Brief History

Semiconductor lasers have seen enormous growth in the decades since their first demonstration by Robert N. Hall in 1962. They are ubiquitous in applications spanning multiple diverse fields, including telecommunications, consumer electronics, medicine, and defense [1–3]. This is no doubt a result of the semiconductor laser's design wavelength flexibility spanning the visible, infrared, and terahertz spectral regions [4–7]. Regardless of the application, these lasers are typically separated into two distinct groups: edge-emitting and surface-emitting semiconductor lasers.

Edge-emitting semiconductor lasers utilize a heterojunction structure where the gain material is sandwiched between two cladding layers (Fig. 1.1). The cladding layers restrict the propagation of the laser radiation to the gain region, with each facet of the cleaved semiconductor acting as a flat mirror. Typically, one of the facets will be coated for transmission of a small percentage of the circulating laser power. Achieving high power operation with this type of semiconductor laser requires a wider and/or longer gain section to handle the increased thermal load of the device, leading to a more elliptical beam profile [8].

The surface-emitting laser is also a semiconductor heterojunction structure, but the light propagates orthogonally to the semiconductor layers (Fig. 1.2). The vertical cavity surface emitting laser (VCSEL) is similar to a edge-emitting laser
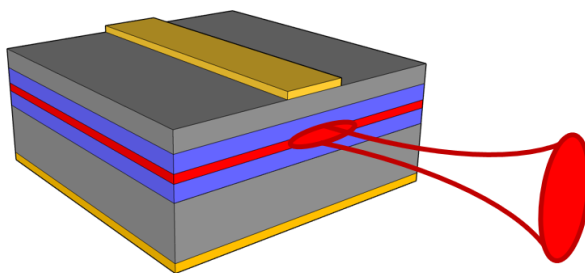
Figure 1.1: Edge-emitting semiconductor laser.

in that it also has a gain, or "active" region, sandwiched between two flat mirrors. However, in the case of the VCSEL, these mirrors take the form of distributed Bragg reflectors (DBRs), which can be designed to have a specific reflectivity. The VCSEL is electrically pumped, with the diffusion of electrons through the active region determining the mode profile. Various techniques have been employed to power scale the VCSEL, but the primary issue remains inefficient heat dissipation out of the structure through the thermally resistant DBR mirrors which can impact generation of high power, high quality TEM_{00} beams [9]. However, arrays of individual low power VCSELs, each with excellent beam quality, have been demonstrated to deliver high power and high speed operation in applications including telecommunications and thermal treatment of materials [10, 11].
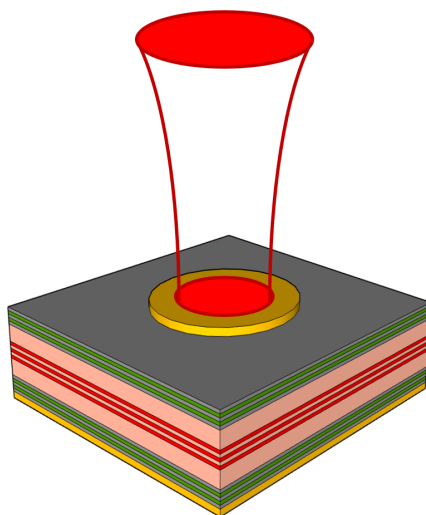
Figure 1.2: Surface-emitting semiconductor laser.

The vertical external cavity surface emitting laser (VECSEL) was able to overcome many of the deficiencies in both edge-emitting and electrically-pumped

surface-emitting lasers by offering high power, diffraction-limited TEM_{00} beams
[12]. A VECSEL layer structure is very similar to that of a VCSEL, in that they
both utilize a multi-quantum well active region for their gain medium. However, a
VECSEL structure has no doped layers, and only contains a single DBR section.
The second mirror, necessary for completion of the laser cavity, is *external* to the
chip structure, as seen in Fig. 1.3.
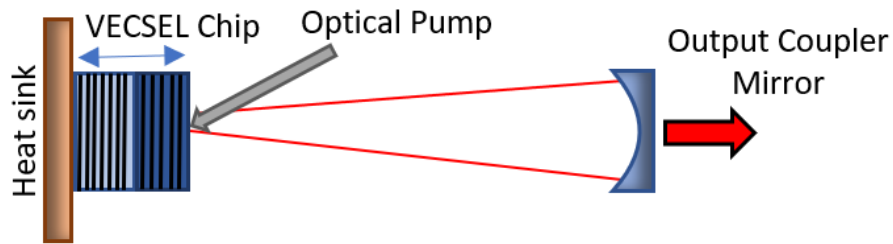
Figure 1.3: VECSEL linear cavity. The VECSEL chip contains a DBR mirror and
the gain section, and the laser cavity is completed by the external output coupler
mirror and optical pump.

A VECSEL can be optically pumped, which allows for a uniform distribu-
tion of photons across the surface of the chip. The size of the pump beam can
also be scaled to pump larger areas of the chip to achieve higher output power
while maintaining single mode operation by appropriate cavity design [13, 14].
This feature of optically-pumped VECSELS simply cannot be accomplished by
electrically-pumped VCSELs because of adverse thermal effects and poor guiding
of electrons through the active region for larger beam sizes, resulting in low power,
multi-mode operation.

Along with generating high power, high quality TEM_{00} beams, the primary
strength of the VECSEL is direct access to the external laser cavity. Access to
this cavity allows for insertion of various optical elements to achieve different
results, such as [15, 16]:

- Birefringent filters for wavelength tuning

- Polarizers to rotate the polarization of the laser beam

- Nonlinear optical crystals for frequency conversion to various harmonics

- Etalons for narrowing of the optical spectrum

- Saturable absorber mirrors for passive mode locking

- Dichroic mirrors and beamsplitters for beam combining/splitting

Different groups have been able to exploit this inherent flexibility to achieve a variety of results. This includes high power harmonic generation from the ultraviolet (UV) to mid-infrared spectral regions, ultra-narrow laser linewidths, high power TEM_{00} beams with high brightness, generation of high order Hermite-Gaussian and Laguerre-Gaussian modes, and high power ultrashort pulse generation [3, 5, 17–21].

1.2 Semiconductor Chip Structure

At the core of any VECSEL system is the multi-quantum well semiconductor (MQW) gain chip. This heterojunction structure combines an active region, with quantum wells sandwiched between barrier sections, with a distributed Bragg reflector (DBR) mirror for high reflectivity of the generated fundamental photons. The surface of the chip is typically anti-reflection (AR) coated to provide protection and increase absorption of the pump photons. A typical VECSEL gain chip layer structure can be observed in Fig. 1.4.
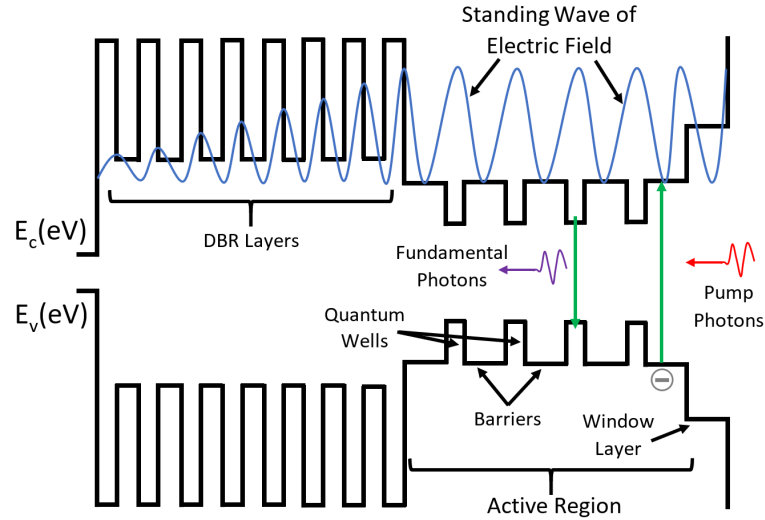
Figure 1.4: Multi-quantum well semiconductor structure. The "active" gain region contains barriers and quantum wells for absorption of incoming pump photons and emission of fundamental photons. The DBR mirror provides >99.9% reflectivity of the fundamental photons.

1.2.1 Active Region

The gain of a VECSEL is contained within the active region of the multi-quantum well semiconductor chip structure, with the wells acting as the gain elements. Each quantum well is sandwiched between barrier sections, with the band gap energy of the barrier being greater than that of the well. The quantum well also has a narrow width sufficient for quantum confinement of electrons in one dimension [22]. If an incoming pump photon has an energy that exceeds the band gap energy of the barrier, it will be absorbed in this region. When a pump photon is absorbed, it will excite an electron from the valence band to the conduction band. The excited electron will diffuse from the barrier region into a quantized energy level within the well. When the electron transitions from the quantized energy level in the conduction band well to an energy level in the valence band well, a *fundamental* photon will be emitted with a wavelength corresponding to the energy lost by the electron in this transition (Fig. 1.5). This fundamental photon will travel through the active region and be reflected by the DBR mirror which has been designed for high reflectivity (>99.9%) around the fundamental wavelength.
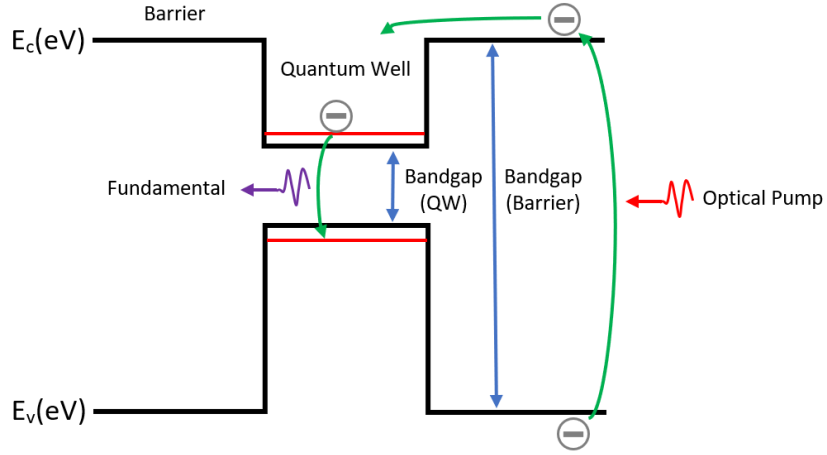
Figure 1.5: Section of active region depicting a single quantum well sandwiched between two barrier sections. A pump photon is absorbed in the barrier, exciting an electron from the valence band to the conduction band. This electron diffuses into the quantum well, with its transition to the valence band well emitting a photon at the fundamental design wavelength.

Typically, the quantum wells are positioned at the locations of the antinodes of the standing electric field, as seen in Fig. 1.4, resulting in a condition known as resonant periodic gain. This has the effect of overlapping the strongest portion of the electric field with the quantum well gain element, doubling the effective gain while significantly reducing amplified spontaneous emission [23]. Alternative designs have utilized groups of tightly-spaced quantum wells around each antinode, which can provide a tolerance for layer thickness variations during the growth process and account for a thermal shift of the antinodes off center of the quantum well during operation [24, 25].

Early models of quantum well gain in a VECSEL were based on a simplified phenomenological logarithmic dependence of the gain on the carrier density

$$g = g_0 \ln \left(N/N_0 \right) \tag{1.1}$$

where g_0 is the material-gain parameter, N is the carrier density, and N_0 is the transparency carrier density [26]. Using this model, the threshold condition for lasing is expressed as

$$R_1 R_2 T_{loss} \exp\left(2\Gamma g_{th} N_w L_w\right) = 1 \tag{1.2}$$

where R_1 and R_2 are the reflectivities of the cavity mirrors (output coupler and DBR), T_{loss} is the transmissivitiy of the cavity, g_{th} is the material gain at threshold, N_w is the number of quantum wells, and L_w is the width of each well [26]. The longitudinal confinement factor, Γ, defines the overlap of the optical field standing wave with the quantum well and can be expressed as

$$\Gamma_z = \frac{\int_{L_a} n_a^2 |E(z)|^2 \, dz}{\int_L n^2(z)|E(z)|^2 \, dz} \tag{1.3}$$

where the numerator expresses the section of the optical field overlapped with the quantum wells and the denominator expresses the entire optical field, with n_a and $n(z)$ representing the refractive indices of the quantum well and additional layers in the z-direction, and L_a and L representing the length of the quantum wells and total length of the active region [27]. The carrier density N can be determined by

$$N = \frac{\eta_{abs} P_p}{h\nu N_w L_w A_p} \tag{1.4}$$

with η_{abs} the pump absorption efficiency, $h\nu$ the photon energy, A_p the pump spot area, and τ the carrier lifetime [26]. We can determine the carrier lifetime using the carrier density in

$$\frac{1}{\tau(N)} = A + BN + CN^2 \tag{1.5}$$

where A, B, and C are the monomolecular, bimolecular, and Auger recombination coefficients, respectively.

1.2.2 DBR Region

The DBR mirror is a stack of $\lambda/4$ layer pairs of alternating refractive index. When a series of these layer pairs is combined, it can result in nearly perfect reflectivity

at the fundamental design wavelength. A greater refractive index contrast between the layers will result in fewer layer pairs needed to achieve >99.9% reflection. After reflection from the DBR mirror, the fundamental photon will travel back through the active region and exit through the surface (window layer) of the chip, into the external cavity.

1.2.3 Thermal Considerations

Excessive heating of the gain chip is one of the most important considerations in maintaining a stable VECSEL system. The strong focusing of the optical pump onto the surface of the chip results in concentration of a significant amount of energy in a small area during high power operation. Waste heat is primarily generated by the quantum defect, which is the difference in energy between the absorbed pump photons and the emitted fundamental photons. Furthermore, any pump photons not absorbed in the active region will be absorbed in the DBR section, further adding to waste heat. The buildup of this thermal energy can lead to a condition known as thermal rollover [28]. The material gain peak and microcavity resonance shift to higher wavelengths as a function of increasing temperature at rates of 0.3 nm/K and 0.1 nm/K, respectively [26]. At high temperature, the gain peak will "rollover" the microcavity resonance entirely, ceasing operation of the laser. Without the laser in operation, nearly all of the incoming optical pump energy becomes waste heat that needs to be extracted from the chip to prevent catastrophic failure and damage to the chip structure.

To mitigate adverse performance from thermal loading, several design strategies should be considered. First, the active region of the MQW chip should include enough barrier length to ensure absorption of all of the incoming pump photons. Second, the quantum defect should be minimized by identifying an ideal balance between optical pump photon energy, fundamental photon energy, and the minimum barrier height needed to prevent thermal leakage of electrons out of the quantum well. The DBR mirror thickness should be minimized by using materials

with a high refractive index contrast, which will result in fewer layer pairs needed to achieve high reflectivity. This is especially important for MQW wafers designed longer wavelength operation near the telecommunication C-band (1530-1565 nm), where the DBR section can account for more than 85% of the total chip thickness and act as a massive thermal impedance, reducing the performance of the laser [25]. Finally, the gain chip should be mounted to a heat sink for efficient dissipation of waste heat. A common method involves solder-bonding the gain chip to a chemical vapor deposition (CVD) diamond heat sink, which has a very high thermal conductivity of 1000-2000 W/mK, and using liquid-cooling or thermo-electric cooling (TEC) to remove the waste heat.

1.2.4 Microfabrication Procedure

In a bottom-emitter layer design, the active region is grown first on the substrate, followed by the DBR section. To expose the active region and heat sink the DBR region, the VECSEL gain chip needs to undergo a substantial microfabrication process. This process involves cleaning, metallization, solder bonding, selective chemical wet etching, and AR coating (Fig. 1.6). The following procedure is utilized for GaAs wafers, but the same metallization steps can be applied to wafers grown on any material system, such as InP/InGaAsP. However, the selective chemical wet-etch steps would need to be altered to use chemicals that are selective to the InP/InGaAsP material system rather than the InGaAs/GaAs/AlGaAs material system described below.

To begin the process, a small piece of wafer ($\sim 4 - 5$ mm^2) and a piece of chemical vapor deposition (CVD) diamond heat sink are thoroughly cleaned with acetone, isopropyl alcohol, and deionized (DI) water. These pieces are then loaded into an electron beam evaporator and a 50 nm layer of titanium, followed by a 200 nm layer of gold, is evaporated onto the DBR-side of the chip and the polished side of the heat sink (Step 1). The samples are then transferred to a thermal evaporator for deposition of $\sim 4 - 6$ μm of indium (Step 2). The indium on both
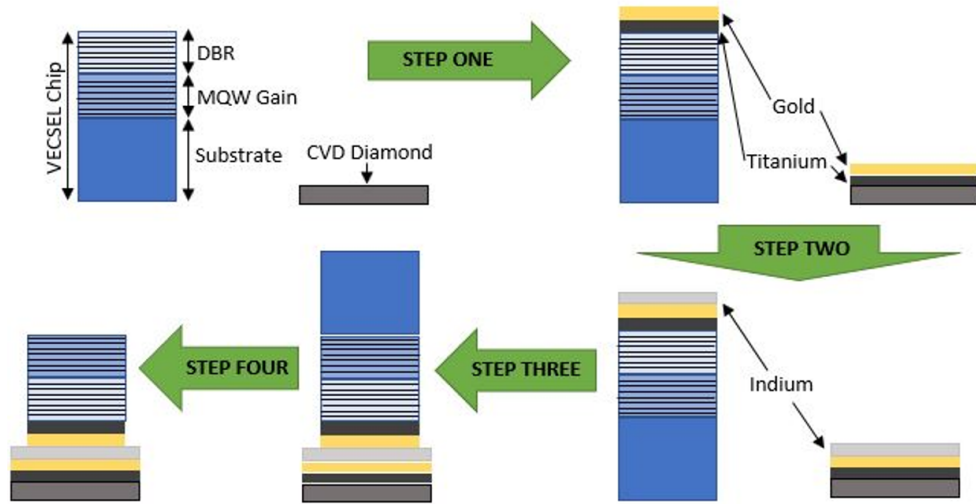
Figure 1.6: Flowchart of the microfabrication procedure used to solder-bond the MQW gain chip to a CVD diamond heat sink for efficient heat dissipation. This process requires a bottom-emitter wafer design, where the active region is grown first on the substrate, followed by the DBR section.

the chip and diamond heat sink are cleaned again in acetone, isopropyl alcohol, and DI water. This is followed deoxidizing the indium in a 1:1 solution of DI water and 30% concentrated hydrochloric acid. The chip is then flip-chip mounted to the heat sink and solder-bonded at 170°C for 30 minutes (Step 3).

After solder-bonding is completed, the 500 μm thick GaAs substrate needs to be removed through selective chemical wet-etching (Step 4). This first involves a fast etch step where a 1:1:8 solution of DI water, 98% concentrated sulfuric acid, and 30% concentrated hydrogen peroxide removes approximately 400 μm of the substrate. This is followed by a slow etch step with a 1:4 solution of 30% concentrated hydrogen peroxide and citric acid. This slow etch will cease when it encounters the first of several etch-stop layers which prevents further etching. This layer is etched with a 1:9 solution of hydrofluoric acid and DI water. The successive etch stop layers are etched by alternating the citric acid solution and the hydrofluoric acid solution. This careful etch-stop procedure ensures that etching stops exactly at the window layer, preserving the microcavity of the active region.

The final step in the microfabrication procedure involves using electron beam evaporation to deposit a 165 nm layer of silicon dioxide as an anti-reflection coat-

ing. This coating protects the surface of the chip and also reduces reflectivity of 808 nm pump laser to less than 5%.

1.3 Basics of Operation

Any laser system requires the same three fundamental components: a cavity, a pump, and a gain medium. The MQW semiconductor chip contains the VECSEL gain medium in the form of quantum wells, along with a DBR mirror. In the case of a simple linear cavity, the cavity is completed with an external mirror that also serves as the output coupler. The pump source can be electrical or optical, but for the purposes of this dissertation, we will focus on VECSEL cavities utilizing optical pumping. Electrically pumped VECSELs have been demonstrated, but they suffer from the same issues as VCSELs: power scalability and mode control issues [29–31]. The primary benefit of electrically pumped VECSELs is the elimination of the fiber-coupled diode pump laser, which can result in a more compact VECSEL package size for potential mass commercialization.

The linear VECSEL resonator cavity (Fig. 1.3) is designed to support the Gaussian beam standing wave. For this cavity configuration, the beam spot size, beam radius of curvature, and divergence can be calculated from the set of standard equations for laser resonators [32],

$$w(z) = w_0 \sqrt{1 + (z/z_R)^2} \tag{1.6}$$

$$R(z) = z[1 + (z_R/z)^2] \tag{1.7}$$

$$\phi(z) = \tan^{-1}(z/z_R) \tag{1.8}$$

where w_0 is the beam waist, z_R is the Rayleigh range, and z is the position within the cavity. The optical pump diameter, or "spot" size, on the chip is

designed to closely match that of the beam waist at that location. For standard fiber-coupled diode pump lasers, a collimator lens and focusing lens is attached to the fiber output to collimate and refocus the fiber laser onto the surface of the chip. The spot size on the chip can be calculated from the following equation,

$$w_{chip} = \frac{f_{f.l.}}{f_{c.l.}} w_{fiber} \tag{1.9}$$

where $f_{f.l.}$ is the focal length of the focusing lens, $f_{c.l.}$ is the focal length of the collimation lens, and w_{fiber} is the diameter of the fiber core. The pump spot size on the chip is typically selected to be approximately 10% larger than the cavity mode size to ensure uniform pump photon distribution across the mode area.

Chapter 2

Introduction to Ultrafast VECSELs

2.1 Brief History

Ultrafast lasers sources, which exhibit a pulse length in the picosecond-femtosecond range and repetition rates in the MHz-GHz range, have seen incredible growth over the past two decades. These lasers have found use in a wide variety of fields and roles, including photodynamic therapy, corneal surgery, material abalation, and exploration of nonlinear processes in atomic, molecular, plasma, and solid-state physics [33–38]. However, solid-state lasers with broad gain bandwidth utilizing saturable absorbers for passive mode locking have a tendency toward Q-switching instabilities due to their typically low gain cross-section which limits their performance [39]. An exception is the Ti:Sapphire laser, but its use is limited due to its significant financial expense. Semiconductor saturable absorber mirrors (SESAMs) incorporated with solid state lasers were demonstrated to be capable of delivering picosecond pulses at multi-GHz repetition rates, but these approaches do not scale well to high power, high repetition rate operation. This limitation occurs because the larger mode size required on the gain medium (solid state crystal) again leads to Q-switching instability and break-up of the pulse train [40].

The VECSEL was the ideal laser platform to suppress the Q-switching instability issue because of its larger gain cross section and smaller gain saturation fluence of quantum wells [41, 42]. Since the first demonstration of a passively mode locked VECSEL utilizing a SESAM in 2000, the laser platform has demonstrated kilowatt

peak powers, watt-level average output powers, multi-GHz operation, and pulses in the femtosecond regime [43–48].

The vast majority of passively mode locked VECSELs are demonstrated in the 900-1200 nm spectral region due to the well-established InGaAs/GaAs material system. However, researchers have also demonstrated their viability in the visible, telecommunications, and mid-IR spectral regions using more complicated material systems including AlGaInP/GaInP, InGaAsP/InP, and InGaSb/GaSb, respectively [49–54]. Some of the limitations of these systems include poor carrier confinement within the quantum wells, complex thermal management due to the quantum defect and thick DBR section, and limited availability of diagnostic tools to characterize laser performance.

2.2   SESAM Design

Active mode locking requires a feedback system to modulate the pulse characteristics, which results in longer pulses than what is possible with passive mode locking, because there is a limit to the response time from electronic equipment [55]. The semiconductor saturable absorber mirror (SESAM) is a passive element, in that it requires no electronic equipment to modulate its performance. This allows it to generate substantially shorter pulse durations, typically in the picosecond-femtosecond regime. This is possible because the pulse itself is responsible for modulation and pulse shaping.

The SESAM has a very similar structure to that of a MQW VECSEL gain chip. The SESAM has a DBR stack for high reflectivity at the fundamental wavelength and an "active" region that typically only contains a single quantum well sandwiched between barrier regions, as see in Fig. 2.1 [56]. The quantum well is designed for absorption of the center wavelength λ_0. The modulation depth, ΔR, of the SESAM is the difference in reflectivity between its saturated and unsaturated state. The nonsaturable loss, ΔR_{ns}, is the total excess loss in the

SESAM caused by scattering or absorption, regardless of the state of saturation. Finally, the saturation fluence, F_{sat}, is the pulse fluence required to saturate, or bleach, the SESAM [8].
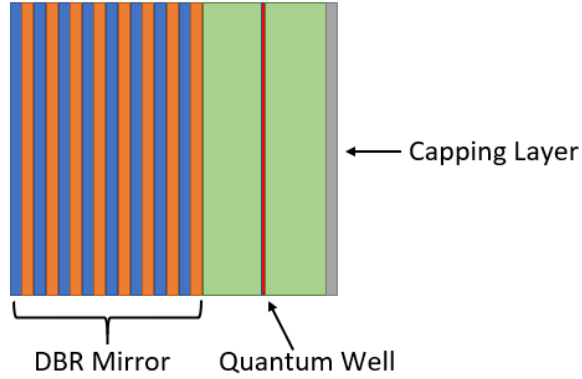
Figure 2.1: Layer schematic of SESAM. The DBR stack is high reflectivity for the fundamental wavelength. The single quantum well acts as the absorber. There is typically a thin capping layer applied to protect the chip from damage.

A SESAM can be designed to be a fast or slow absorber, which refers to the recovery time being faster or slower than the generated pulse duration. A semiconductor structure grown with standard parameters exhibits a recovery time in the nanosecond range. To reduce the recovery time to picoseconds, the growth temperature can be reduced, which increases the prevalence of point defects in the absorber that exhibit fast carrier trapping [57]. Fast saturable absorbers have the benefit of a faster recovery time, but this also has an adverse gain filtering effect for shorter pulse duration in the femtosecond regime caused by the interaction between the gain and the pulse shortening mechanism of the SESAM [58].

The multi-layer structure of the SESAM allows for analysis of the overlap of the intracavity standing wave pattern with respect to the layer structure. The spacer thickness between the DBR stack and the absorber section is designed to position an antinode of the field over the absorber section. The spacer thickness after the absorber section is then designed to result in a resonant or anti-resonant SESAM specified by the round-trip phase change in this final spacer layer [8, 56]. Anti-resonant SESAMS are more common due to their broader reflectivity bandwidth around the center wavelength, but they exhibit higher saturation fluences. Res-

onant SESAMs have reduced saturation fluences and are used in cavities where multi-GHz repetition frequencies are desirable, but its parameters are strongly wavelength dependent.

The carrier and saturation dynamics of a SESAM can be described using a basic semiconductor physics band gap model (Fig. 2.2). At low fluence, photons entering the active region are absorbed in the quantum well, exciting an electron from the valence band to the conduction band (1)-(2). This excited electron will transition back to the valence band during the recovery time (3)-(4). This process will continue for fluences below the saturation fluence. Once the saturation fluence has been reached, a bleaching effect occurs in the absorber, where all available electrons are excited into the conduction band. At this point, the loss of the absorber is reduced by the modulation depth ΔR, and the next incoming photons will pass through the transparent active region. The excited electrons will transition back to the valence band during the recovery time for the process to start again. It is this passive process which leads to ultrafast operation of passively mode locked VECSELs.
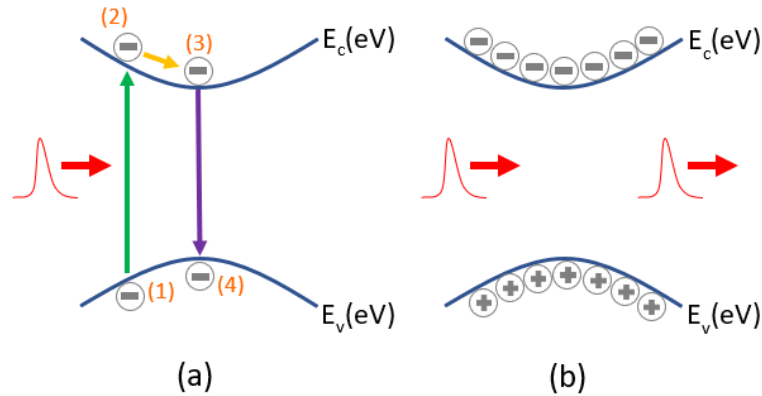
Figure 2.2: Basic functionality of a SESAM acting as a slow saturable absorber. In (a), incoming photons excite an electron from the valence to conduction band. This electron eventually transitions back to the valence band following the recovery time. In (b), the saturation fluence has been reached and the absorber is bleached.

2.2.1 Basics of Operation

While an optically-pumped passively mode locked VECSEL looks very similar to a CW VECSEL cavity, there are additional parameters that must be considered to induce stable mode locking. One of the primary challenges involves balancing the VECSEL's dynamic gain saturation against the SESAM's dynamic absorption saturation, behavior which can be observed in Fig. 2.3 [8, 42, 59].
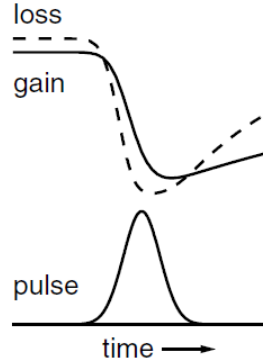
Figure 2.3: Pulse formation with dynamic gain and absorption, such as that with a passively mode locked VECSEL utilizing a SESAM.

In this type of laser system, it is imperative that the absorber saturates before the gain. This will result in a net gain window forming where the loss of the absorber is temporarily reduced below the gain. The region where this behavior occurs is defined by the mode area ratio S_{area} and is expressed as

$$S_{area} = \frac{E_{sat,g}}{E_{sat,a}} = \frac{F_{sat,g}A_g}{F_{sat,a}A_a} = \frac{A_g}{A_a} \gg 10 \tag{2.1}$$

where $E_{sat,g}$, $E_{sat,a}$, $F_{sat,g}$, $F_{sat,a}$, A_g, and A_a are the saturation energies, saturation fluences, and mode areas of the VECSEL gain and SESAM absorption, respectively [42, 60]. The same material system is generally used for the quantum wells in both the gain chip and SESAM absorber, resulting in a similar saturation fluence for both devices. This reduces S_{area} to be the ratio between the physical mode area on the gain chip versus the SESAM. It has been demonstrated that for stable passive mode locking to have a gain advantage over CW operation when using a slow saturable absorber, the mode area ratio should be between 10-30 [61]. This

means that the cavity design needs to have a mode area 10-30X larger on the gain chip than the SESAM.

For passive mode locking with slow saturable absorbers, where the recovery time of the absorber is long compared to the pulse duration, the net gain window can be up to 10X longer than the actual pulse duration and still achieve stability. The leading edge of the pulse will be absorbed in the SESAM during each round-trip, and the noise trailing the pulse will lead to a further increase in the pulse energy. This process allows the pulse to "walk backwards" every round-trip and results in the trailing noise eventually becoming merged into the pulse, preventing the noise from overtaking the pulse formation process [60]. This has a cleaning effect on the pulse formation, although the generated pulse is typically chirped and has a somewhat imperfect sech^2 pulse shape [42]. Every time the circulating pulse within the resonator hits the output coupler mirror, a portion of the pulse will be ejected from the cavity with a repetition rate equal to $\Delta \nu = c/2L$, where c is the speed of light and L is the length of the resonator.

2.2.2 Cavity Design

The most common resonator cavity layouts for a passively mode locked VECSEL are the V- and Z-cavities (Fig. 2.4). These are frequently used because the supported Gaussian beam within the resonator will have multiple beam waist locations, which is ideal for achieving a larger spot size on the gain chip and a substantially smaller spot size on the SESAM. The Z-cavity offers more freedom in design than the V-cavity, but typically at the expense of a larger cavity and lower repetition frequency. While both cavity configurations allow for a double-pass of the gain chip for power enhancement, the Z-cavity will provide greater flexibility in design by providing substantially different Gaussian beam diameters at the location of the VECSEL chip and SESAM. Furthermore, gain broadening has been demonstrated by folding the beam off the gain chip in this manner [62].

While a V-cavity design was used to demonstrate 50 GHz operation using a
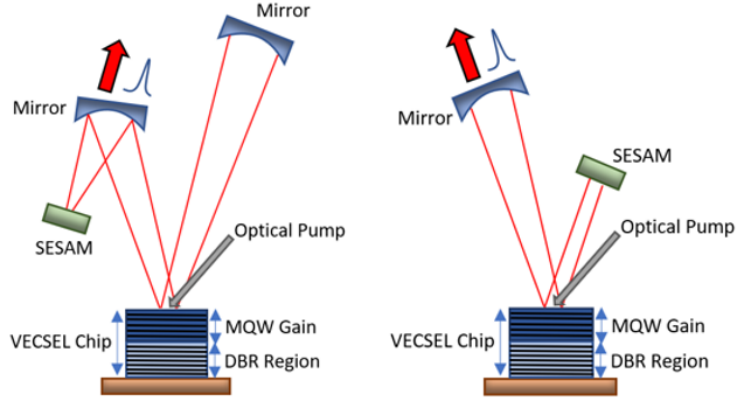
Figure 2.4: Passively mode locked VECSEL in Z- and V-cavity configurations. The SESAM is acting as an end mirror in both of these configurations, which allows for designing a different mode area on the gain and absorber.

3 mm cavity length, there are practical limitations as to how to continue to scale this approach for commercial applications when considering the cavity geometry and mirror dimensions [44]. One promising approach has been the wafer-scale integration of the saturable absorber structure of the SESAM onto the VECSEL MQW gain chip [61]. This novel device is referred to as a mode-locked integrated external-cavity surface-emitting laser (MIXSEL) and takes advantage of a simple linear cavity (Fig. 2.5) [63].
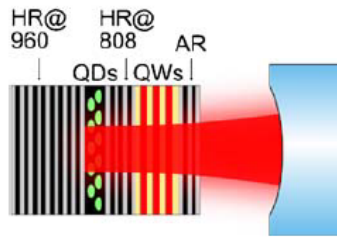
Figure 2.5: Linear cavity incorporating a mode-locked integrated external-cavity surface-emitting laser. The semiconductor chip incorporates the gain (quantum wells) and absorber (quantum dots) onto the same structure.

Other cavity geometries are used to generate a smaller beam spot on the SESAM than on the VECSEL chip to achieve the desired mode area ratio for stable mode locking. This is based on quantum wells being used in both the saturable absorber and gain chip, which exhibit similar saturation fluences due to similar material parameters. The MIXSEL gets around this limitation by utiliz-

ing quantum dots for the saturable absorber and quantum wells for the gain. The quantum dots have carrier confinement in three dimensions, which lowers the density of states and thus the optical intensity needed for saturation. This results in a device that has the same beam diameter throughout the structure, but saturates the saturable absorber before the gain [63]. The MIXSEL has been demonstrated to deliver multi-watt average powers and ultrashort sub-picosecond pulses [64, 65].

2.2.3 Characterization

The characterization of an ultrafast laser involves four standard measurements: the pulse duration, the RF frequency of the pulse train, the optical spectrum, and the average output power. Additional testing can be conducted based on the availability of diagnostic equipment, such as a fast oscilloscope trace of the pulse train or direct measurement of the pulse energy. For the purposes of this dissertation, the available diagnostic tools for pulse characterization were:

- APE pulseCheck USB 150 autocorrelator for free-space pulse measurement from 50 fs - 35 ps. Interchangeable optics kits allow measurement of pulse duration in the 200-360 nm, 420-500 nm, 700-1100 nm, and 1000-1600 nm range.

- HP 8593E RF spectrum analyzer for pulse repetition measurement from 9 kHz - 22 GHz.

- HP 70950B and Avaspec optical spectrum analyzers for measurement of wavelengths from 200-1700 nm.

- Thorlabs thermal power meter for average laser power measurements.

These tools have been used to characterize the laser cavities described in this dissertation. As an example, the following set of data was obtained from an early build of a passively mode locked VECSEL in a Z-cavity configuration. As seen below in Fig. 2.6, this cavity has an end mirror M1, fold mirror M2, a long arm length L1+L2, and short arm length of L3.
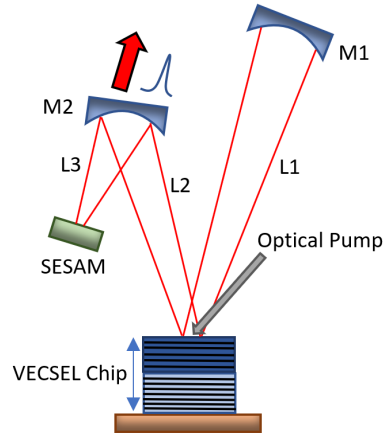
Figure 2.6: Z-cavity configuration used for demonstration of the measurement techniques for characterization of passively mode locked lasers.

Mirrors M1 and M2 have a 30 cm and 7.5 cm radius of curvature, respectively, with similar 99% reflectivity coating at ∼1064 nm. The SESAM has a 25 ps recovery time, with a modulation depth ΔR of 2% and nonsaturable loss of 1%. The long arm length was 25 cm and the short arm length was 3 cm. This results in a total cavity loss 4%. The mode diameter on the chip was ∼440 μm and the mode diameter on the SESAM was ∼120 μm, for a mode area ratio of 14. The chip was pumped with an fiber-coupled 808 nm diode laser with a 504 μm diameter on the chip. Both the chip and SESAM were maintained at a temperature of 20°C. Stable mode locking was achieved at approximately 26.5 W of optical pump power.
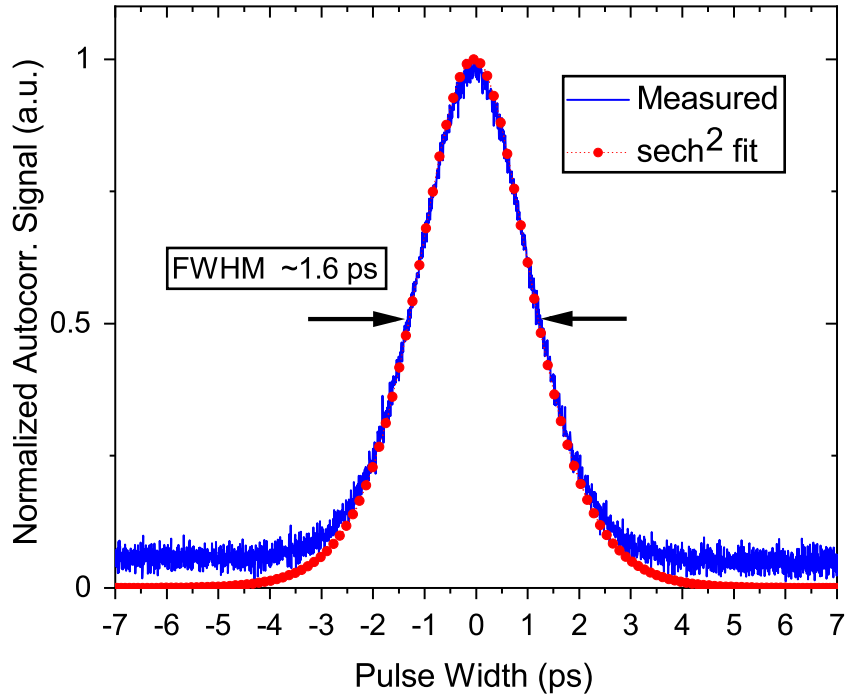
Figure 2.7: Autocorrelation measurement of the fundamental pulse. This pulse had a sech^2 pulse fit of 1.6 ps.

The autocorrelation measurement of the pulse observed in Fig. 2.7 was obtained with the APE pulseCheck using the optics kit for near-IR wavelengths. The data was overlapped with a sech^2 pulse with a width of 1.6 ps. The similar overlap between the measurement and the fit demonstrates the tendency for the pulse shape from passively mode lock VECSELs to resemble sech^2 profiles, rather than Gaussian profiles.
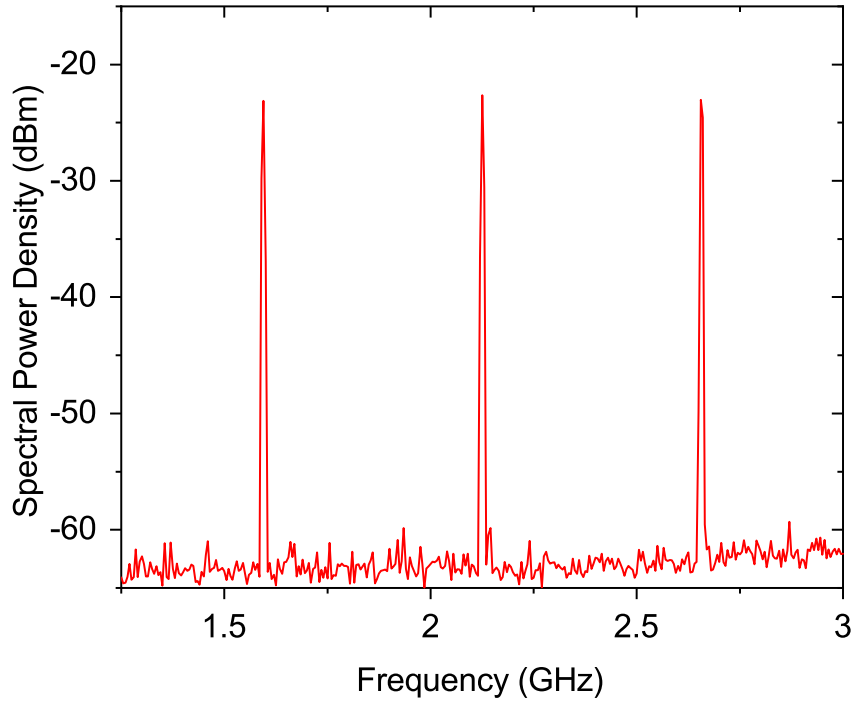
Figure 2.8: RF spectrum of the fundamental pulse demonstrating a repetition frequency of 530 MHz.

The repetition rate of the laser is determined by an RF frequency measurement using a fast photodiode and RF spectrum analyzer. The repetition frequency should have a clear signal to noise floor of >30 dBm, without any additional intensity peaks between the primary repetition frequency peaks which would indicate an unstable cavity. The RF spectrum measurement observed in Fig. 2.8 has a peak separation of ∼530 MHz. The cavity was designed to have a total length of 28 cm, which would lead to a calculated repetition frequency $\Delta\nu$ of 535 MHz. This indicates that our measured repetition frequency represents a stable passively mode locked VECSEL.
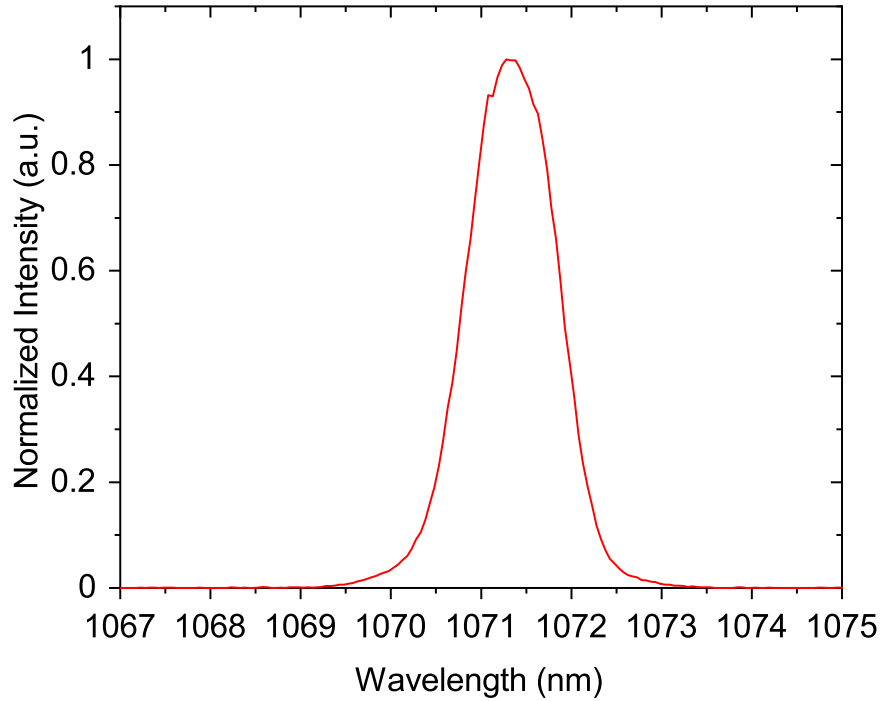
Figure 2.9: Optical spectrum of the fundamental lasing wavelength centered at ~1071.5 nm.

The optical spectrum of the Z-cavity was centered near 1071.5 nm, as observed in Fig. 2.9. The full width at half maximum (FWHM) bandwidth of the spectrum was approximately 1 nm. This is typical of VECSELs, which have less overall gain than other laser sources, such as solid state or dye lasers. This has a direct limiting effect on how short of a pulse width is achievable with a VECSEL, due to the inverse relationship between pulse width and spectral bandwidth [66].

Chapter 3

Ultrafast VECSEL Resonator Design and Pulse Modeling

3.1 ABCD Transfer Matrix Method for Resonator Design

A VECSEL resonator needs to be designed and modeled to determine the behavior of the Gaussian beam within the cavity to ensure TEM_{00} operation. Different cavity configurations, use of various optical elements, and specific laser operation requirements necessitate modeling the Gaussian beam to determine the beam diameter and divergence at different points within the resonator. In a cavity configuration with fold mirrors with optical power, astigmatism will be introduced which will alter the shape of the Gaussian beam from circular to elliptical. This ellipticity can be advantageous on the gain chip because the optical pump is typically angled at 20-30° with respect to the chip, creating an elliptical pump spot which should match the ellipticity on the gain chip to maximize the efficiency of the pump laser. For stable passive mode locking, it is necessary to model the spot sizes at the gain chip and SESAM to ensure that the saturation parameter is within the acceptable range of 10-30 [61]. The length of the resonator will determine the repetition frequency of the laser, which can be compared against data obtained from the RF spectrum analysis to determine proper mode locked behavior. Other important parameters can also be deduced from the Gaussian beam model.

3.1.1 Theory

The standard approach for modeling a Gaussian beam within a resonator cavity is the ABCD ray transfer matrix method [67]. This method takes advantage of the paraxial approximation, where for small angles, $sin(\theta) \approx \theta$, $tan(\theta) \approx \theta$, and $cos(\theta) \approx 1$. This allows for the use of two linear algebra equations to describe an arbitrary ray before and after passage through any optical element that can be described by a 2x2 matrix element that acts on the ray (Fig. 3.1) [68].
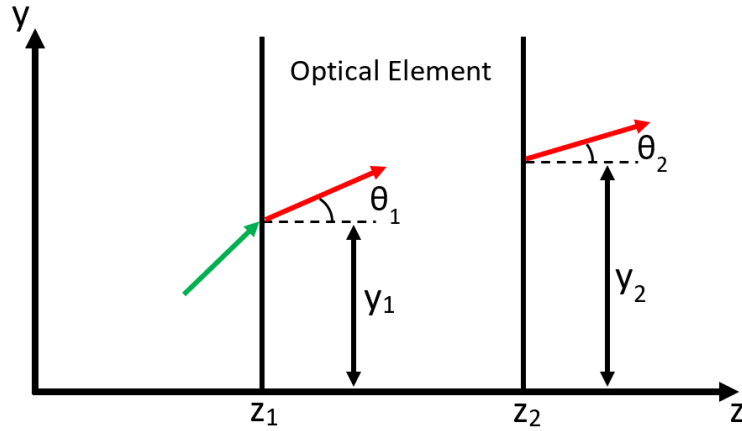
Figure 3.1: The matrix transfer method takes any incoming ray (green arrow) and transforms it with a 2x2 matrix representing the optical element, resulting in the ray seen exiting from the plane at z_2.

The simplified optical system depicted in Fig. 3.1 can be described by the following equations

$$y_2 = Ay_1 + B\theta_1 \tag{3.1}$$

$$\theta_2 = Cy_1 + D\theta_1 \tag{3.2}$$

where $y_1, y_2, \theta_1, \theta_2$ are the ray height and ray angle for the initial and final rays, respectively, and A,B,C, and D represent real numbers. This set of equations can be expressed in matrix form as

$$\begin{bmatrix} y_2 \\ \theta_2 \end{bmatrix} = \begin{bmatrix} A & B \\ C & D \end{bmatrix} = \begin{bmatrix} y_1 \\ \theta_1 \end{bmatrix} \tag{3.3}$$

44

$$\mathbf{M} = \begin{bmatrix} A & B \\ C & D \end{bmatrix}. \tag{3.4}$$

The internal matrix in Equation 3.3 is the generic matrix $\mathbf{M}$ that is used to describe different optical elements, such as free-space propagation, refraction at planar boundaries, refraction a spherical boundary, or reflection from mirrored surfaces. These elements are expressed by the following derived set of matrices [32, 67, 68]:

$$\textbf{Free space propagation}: \mathbf{M} = \begin{bmatrix} 1 & d \\ 0 & 1 \end{bmatrix} \tag{3.5}$$

$$\textbf{Refraction at planar boundary}: \mathbf{M} = \begin{bmatrix} 1 & 0 \\ 0 & \frac{n_1}{n_2} \end{bmatrix} \tag{3.6}$$

$$\textbf{Refraction at spherical boundary}: \mathbf{M} = \begin{bmatrix} 1 & 0 \\ -\frac{(n_2 - n_1)}{n_2 R} & \frac{n_1}{n_2} \end{bmatrix} \tag{3.7}$$

$$\textbf{Reflection from spherical mirror}: \mathbf{M} = \begin{bmatrix} 1 & 0 \\ -\frac{2}{R} & 1 \end{bmatrix} \tag{3.8}$$

$$\textbf{Reflection from planar mirror}: \mathbf{M} = \begin{bmatrix} 1 & 0 \\ 0 & 1 \end{bmatrix} \tag{3.9}$$

where d is the propagation distance, n_1 and n_2 are the refractive indices of the media, and R is the radius of curvature of the mirror.

The matrix in Equation 3.9 is a special case of reflection from a spherical mirror when the radius of curvature $R \to \infty$. There is another important consideration for reflection from spherical mirrors that have different focal points in the tangential (vertical) and sagittal (horizontal) planes due to astigmatism introduced by a folded mirror, a common design feature in VECSEL cavity configurations. These different focal lengths can be described as by:

$$f_x = f/cos(\theta) \tag{3.10}$$

$$f_y = fcos(\theta) \tag{3.11}$$

where θ is the half fold angle off of the mirror, and f_x and f_y are the focal lengths in the sagittal and tangential planes, respectively [69]. Using the simple geometrical optics relation $R = 2f$, the matrix $\mathbf{M}$ for a spherical mirror introducing astigmatism into the resonator must now be represented by two separate matrices, depending on the plane of propagation being modeled:

$$\textbf{Reflection from spherical mirror (sagittal)} : \mathbf{M} = \begin{bmatrix} 1 & 0 \\ -\frac{2cos(\theta)}{R} & 1 \end{bmatrix} \tag{3.12}$$

$$\textbf{Reflection from spherical mirror (tangential)} : \mathbf{M} = \begin{bmatrix} 1 & 0 \\ -\frac{2}{Rcos(\theta)} & 1 \end{bmatrix}. \tag{3.13}$$

This this set of matrices, any arrangement of optical elements can be modeled by multiplying them together according to the reverse order in which the circulating beam encounters them: $\mathbf{M_T} = \mathbf{M}_N...\mathbf{M_3}\mathbf{M_2}\mathbf{M_1}$. The elements A, B, C, and D from the system matrix $\mathbf{M}_T$ can then be extracted for further analysis, including the resonator stability condition expressed as [67]:

$$-1 < \frac{1}{2}(A + D) < 1. \tag{3.14}$$

For a Gaussian beam in a laser resonator, where stability requires that the beam replicate itself in a fixed plane after a round-trip, the so-called "q parameter" can be related to the system matrix elements by

$$q_2(z) = \frac{Aq_1 + B}{Cq_2 + D} \quad \rightarrow \quad q(z) = \frac{Aq(z) + B}{Cq(z) + D} \tag{3.15}$$

and the q parameter can be directly related to the Gaussian beam radius of cur-

vature $R(z)$ and beam radius $w(z)$ by

$$\frac{1}{q(z)} = \frac{1}{R(z)} - j\frac{\lambda}{\pi w^2(z)} \tag{3.16}$$

which allows for simple algebra to be used to solve for $R(z)$ and $w(z)$ if the system matrix elements are known [70, 71]. After some algebraic manipulation of Equation 3.15, we arrive at

$$\frac{1}{q(z)} = \frac{A - D}{2B} - j\frac{\sqrt{1 - (A + D)^2/4}}{B} \tag{3.17}$$

where we made use of the determinant of the system matrix, $AD - BC = 1$. The real and imaginary parts in Equations 3.16 and 3.17 can now be equated to directly determine $R(z)$ and $w(z)$ with only the system matrix elements and the laser wavelength. This extremely powerful result can be easily modeled in simulation software, such as Mathworks MATLAB, to determine the beam radius at any defined plane within any arbitrary resonator cavity.

3.1.2   Linear Cavity

A VECSEL linear cavity is composed of a flat mirror (the VECSEL gain chip) and a single curved end mirror, or output coupler. Figure 3.2 demonstrates a stable Gaussian beam within this resonator cavity, with a beam waist of approximately 440 μm located at the chip. This cavity was simulated for a fundamental wavelength of 1064 nm, 30 cm radius of curvature (RoC) mirror, and a cavity length of 8 cm. The sagittal and tangential beams overlap because there is no astigmatism in this cavity.
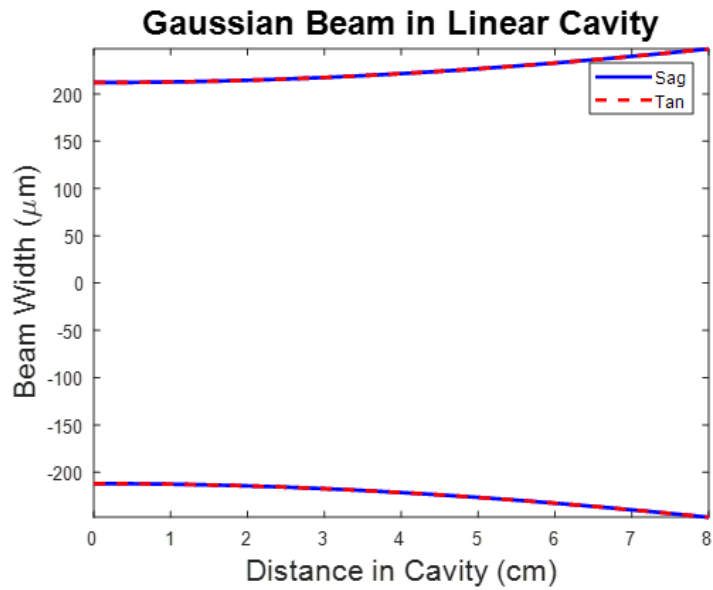
Figure 3.2: VECSEL linear cavity demonstrating a stable Gaussian beam.

3.1.3 V-Cavity

A V-cavity configuration is slightly more complicated, in that it typically includes a spherical "fold" mirror between the VECSEL chip and the flat end mirror. The fold mirror introduces astigmatism to the cavity. Furthermore, the cavity is usually referred to as having a "long arm" and a "short arm" which represent the cavity length between the chip and fold mirror, and fold mirror and end mirror, respectively (Fig. 3.3).
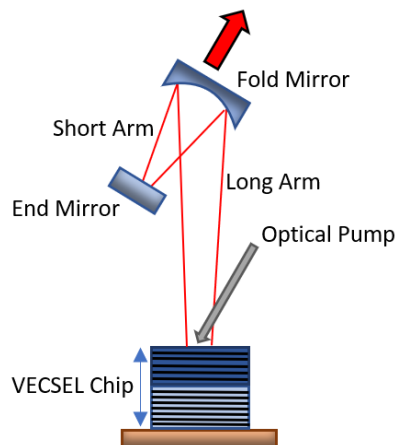
Figure 3.3: VECSEL V-cavity configuration with a fold and end mirror. The short arm can typically be adjusted by several millimeters to fine-tune the Gaussian beam parameters.

The short arm is typically adjusted by some millimeters to achieve specific Gaussian beam spot sizes on the chip, fold, and end mirrors. This is important to make sure that the spot size on the chip closely matches the pump spot size to ensure TEM$_{00}$ operation and efficient optical pumping. The same transfer matrix method can be used to observe the evolution of the beam diameter at specific locations within the cavity as a function of another varying parameter, such as the short arm length.
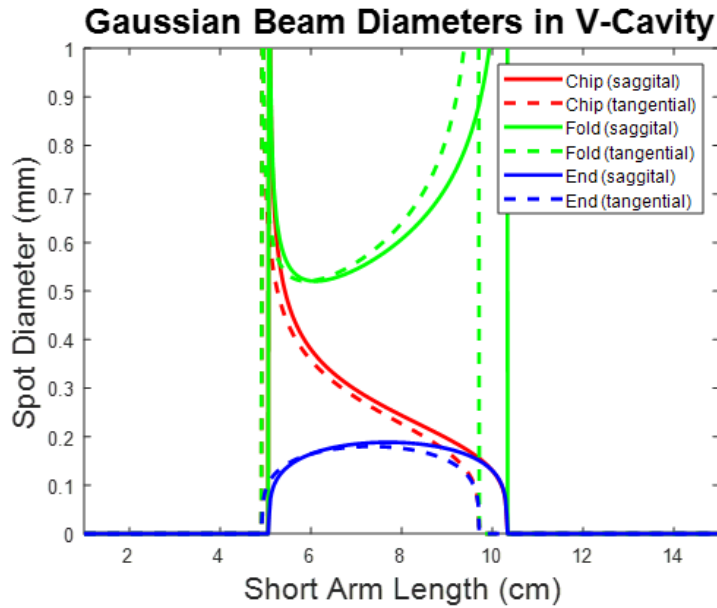
Figure 3.4: Gaussian beam diameter within the V-cavity for both the sagittal and tangential planes. The beam size is modeled at the chip, fold mirror, and end mirror for a varying short arm length.

The beam in Figure 3.4 was modeled for a V-cavity with a fundamental wavelength of 1064 nm, a fold mirror RoC of 10 cm, a full fold angle of 20°, and a long arm length of 10 cm. From this plot, a specific short arm length can be selected and it is immediately clear what the beam diameter will be at the three different locations within the cavity in both the sagittal and tangential planes. This makes it possible to select a short arm length of 6 cm that results in a circular, rather than elliptical, spot at the end mirror (Fig. 3.5).
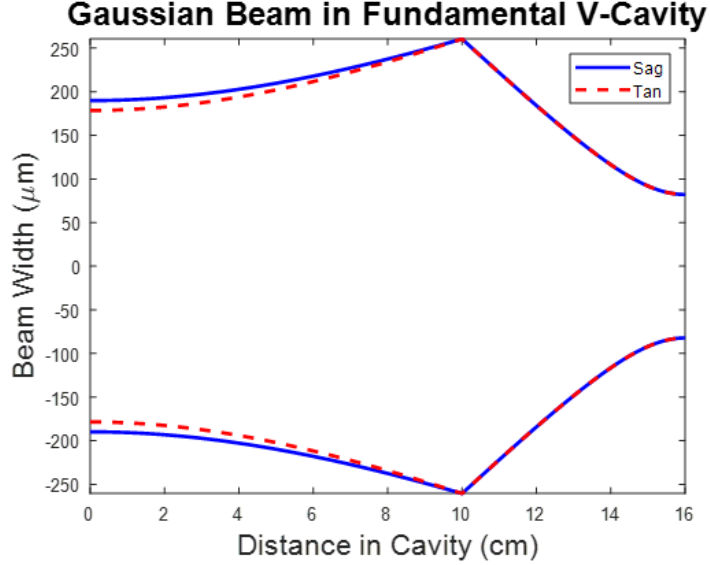
Figure 3.5: Gaussian beam propagation within the V-cavity for a short arm length of 6 cm. Note that the astigmatism caused by the fold mirror has resulted in slightly different beam characteristics in the sagittal and tangential planes.

3.1.4 Z-Cavity

For a passively mode locked VECSEL, the Z-cavity configuration is ideal because it allows for designing Gaussian beam characteristics necessary to achieve a saturation parameter of 10-30 while also folding off of the gain chip for gain enhancement. The Z-cavity in Figure 3.6 is essentially a V-cavity with an extra fold on the gain chip. The chip acts as a flat mirror without adding optical power to the beam. This provides flexibility for positioning the chip in the "long arm" between mirrors M1 and M2 where there is variability in the beam diameter for a fixed beam diameter on the SESAM.

The Gaussian beam diameter characterization in Figure 3.7 demonstrates the beam size at mirrors M1 and M2, along with M3 which represents the SESAM. This simulation was performed for a fundamental wavelength of 1064 nm, full fold angle of 20°, a long arm length (L1+L2) of 20 cm, and mirror RoC of 30 cm and 7.5 cm for M1 and M2, respectively. A short arm length, L3, was selected to be 3.3 cm.
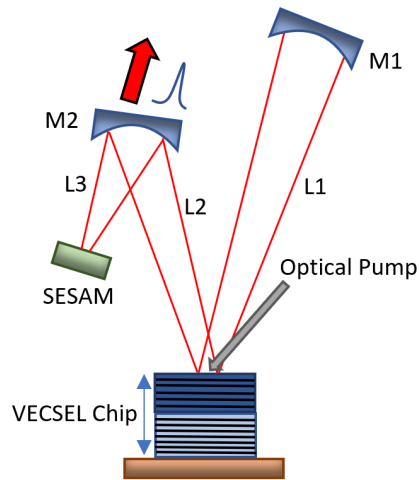
Figure 3.6: VECSEL Z-cavity configuration commonly used for passively mode locked VECSELs.
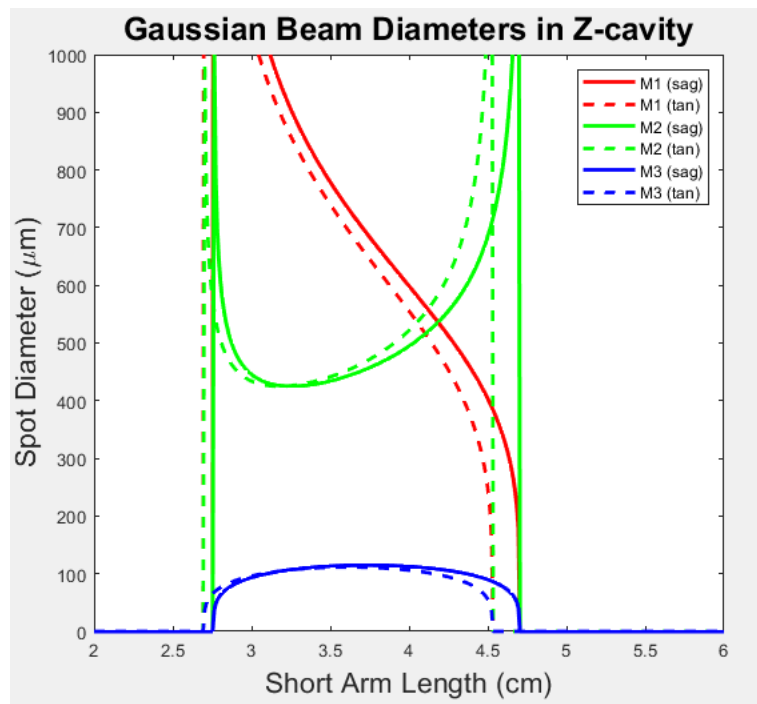
Figure 3.7: Gaussian beam diameter within the Z-cavity for both the sagittal and tangential planes. M3 represents the SESAM. A short arm length of 3.3 cm is selected to model the full Gaussian beam within the cavity and determine the location of the chip to achieve a desired saturation parameter.

The full Gaussian beam can now be modeled for this Z-cavity (Fig. 3.8). The location of the chip can be placed anywhere between M1 and M2. The lower plot observed in Figure 3.8 shows the mode area ratio for different positions of the chip throughout the cavity. By careful examination of these two plots, an ideal location for the chip can be determined to achieve the aforementioned parameters for a stable resonator for a passively mode locked VECSEL.
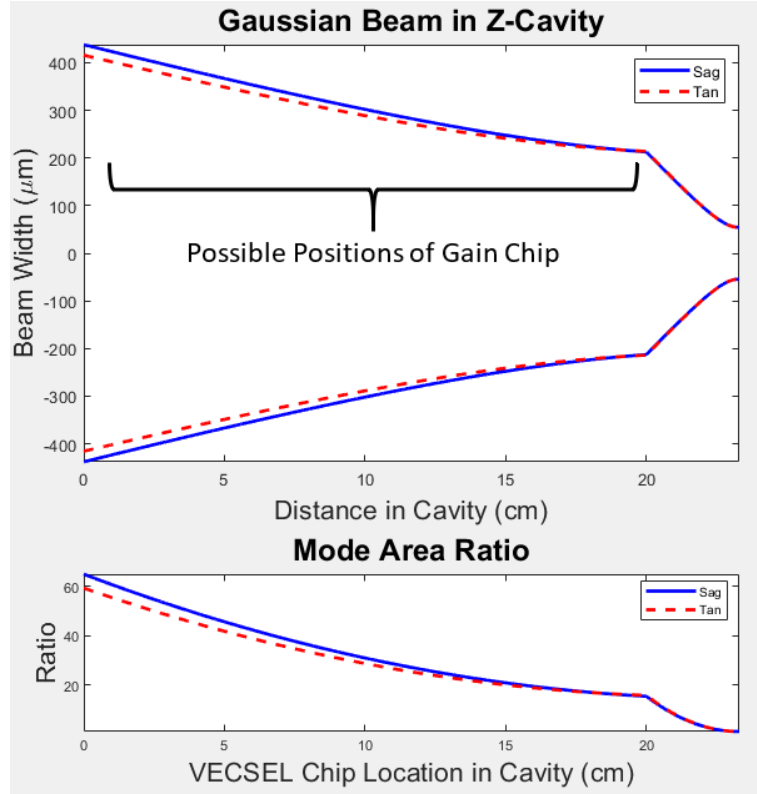
Figure 3.8: Gaussian beam propagation through the Z-cavity for both the sagittal and tangential planes for a short arm length of 3.3 cm. The bottom plot shows the various mode area ratios possible depending on the position of the gain chip.

3.2   Operator Method for Pulse Modeling

Before a resonator cavity is constructed for passive mode locking of a VECSEL, it is necessary to model pulse formation and stability. One of the earliest efforts to model mode locked pulse formation within a resonator is the Haus Master Equation, where the gain, loss, chromatic dispersion, and optical nonlinearities act on a circulating pulse in the form of $A(t)$, which represents a complex am-

plitude [55, 72]. The primary benefit of the Master Equation is that it provides an analytical solution for pulse formation. For every trip through the resonator, each parameter slightly modifies the pulse shape. After many thousands of round trips, a stable pulse forms (if a solution exists). The caveat is that no single pulse shaping mechanism can have a strong effect on the pulse during any single pass through the resonator, and any parameter must be sufficiently simple to model to result in an analytical solution. For a passively mode locked VECSEL, this model encounters trouble because of the strong saturation effect of the SESAM.

3.2.1 Theory

A new approach was developed to specifically model pulse formation for a resonator of a passively mode locked VECSEL based on quasi-soliton behavior, which results in a $sech^2(t/\tau)$ pulse shape. This numerical method utilizes the slowly varying envelope approximation (SVEA),

$$\tilde{E}(t) = Re\{A(t)exp(-\omega_0 t)\} \tag{3.18}$$

$$P(t) = |A(t)|^2 \tag{3.19}$$

where $\tilde{E}(t)$ is the electric field, $A(t)$ is the complex envelope, $P(t)$ is the instantaneous power of the pulse, and ω_0 is the fundamental frequency [42, 73]. If we discretize the time step ΔT such that $A(t)$ is essentially constant during this time step, the SVEA is valid for this numerical method. This allows us to focus exclusively on the evolution of $A(t)$.

Each element within the resonator that has a pulse-shaping mechanism is now described by an "operator" which acts on the pulse during each round-trip through the cavity. These operators will include the gain saturation of the chip, loss saturation of the absorber, group delay dispersion (GDD), gain filtering, second harmonic generation, and noise effects.

3.2.2 Operator Definitions

The dynamic gain of a passively mode locked VECSEL can be described by

$$\frac{dg(t)}{dt} = \frac{g_0 - g(t)}{\tau_g} - g(t)\frac{P(t)}{E_{sat,g}} \tag{3.20}$$

where g_0 is the small signal gain, τ_g is the recombination time, and $E_{sat,g}$ is the saturation energy of the gain [42]. For a discretized time step Δt, the gain is modeled as

$$\Delta g_g = g(t + \Delta t) = g(t) + \Delta t \left[\frac{g_0 - g(t)}{\tau} - g(t)\frac{P(t)}{E_{sat,g}} \right]. \tag{3.21}$$

The saturation of the SESAM is handled similarly to the saturation of the chip

$$\frac{dg(t)}{dt} = \frac{-\frac{\Delta R}{2} - g(t)}{\tau_s} - g(t)\frac{P(t)}{E_{sat,s}} \tag{3.22}$$

where τ_s is the recovery time of the SESAM, $E_{sat,s}$ is the saturation energy of the SESAM, and the small signal gain g_0 has been approximated by $-\Delta R/2$, where ΔR is the modulation depth [8]. For clarity, the numerical model for the loss saturation is

$$\Delta g_s = g(t + \Delta t) = g(t) + \Delta t \left[\frac{\frac{(-\Delta R)}{2} - g(t)}{\tau_s} - g(t)\frac{P(t)}{E_{sat,s}} \right]. \tag{3.23}$$

Both the gain and loss saturation act upon the pulse in the time domain.

The dynamic nature of the gain saturation of both the VECSEL chip and SESAM will lead to a nonlinear phase change. This nonlinear phase change is related to the changing carrier densities, which is in turn related directly to the gain or loss [73]. A change in the carrier densities also results in a change in the refractive index of the material. This effect leads to a broadening of the linewidth by a factor of $1+\alpha^2$, where α is known as the linewidth enhancement factor [74]. A larger value of α represents excitation closer to the band gap in the VECSEL chip

or SESAM. The value of α for a SESAM should be less than that of a VECSEL chip since excitation of carriers in the SESAM is expected to happen higher above its respective band gap. The nonlinear phase change associated with the linewidth enhancement can be modeled as

$$\Delta\phi(t) = \frac{\alpha}{2}g(t). \tag{3.24}$$

This phase modification to the pulse shape is implemented in code as two separate operators, one for the VECSEL chip and another for the SESAM, since each one will have its own respective linewidth enhancement factor. These operators are modeled in code as

$$r_{g,s}(t) = exp\big[(1 - i\alpha)\Delta g_{g,s}\big] \tag{3.25}$$

where $r_g(t)$ and $r_s(t)$ are the complex reflectivities of the gain and saturable absorber, respectively. As can be seen above, the gain and loss saturation is calculated and inserted into the complex amplitude reflectivity, and it is this reflectivity that finally operates on the incoming optical pulse in the time domain.

Another operator is needed to model the finite gain bandwidth of the VECSEL chip, which will determine the wavelength of the output pulses and limits the pulse duration [1]. This is a rather simple filtering operator, modeled as

$$g_{filter}(\omega) = exp\left[-\left(\frac{\omega}{\omega_c}\right)^2\right] \tag{3.26}$$

where ω is our predefined frequency grid and ω_c is the limited frequency bandwidth of the gain [75]. This operator is applied in the frequency domain, which requires a Fourier transform of the incoming pulse into frequency space, application of the operator, and then inverse Fourier transforming back into the time domain.

The pulse duration and cavity stability are also affected by group delay dispersion (GDD), which is a change in the spectral phase of the pulse and is modeled as

$$\phi(\omega) = \frac{1}{2}D_2(\omega)^2 \tag{3.27}$$

where D_2 is the GDD coefficient. In operator form, the GDD can be expressed as

$$GDD = exp\left[iD_2\left(\frac{\omega^2}{2}\right)\right] \tag{3.28}$$

with fs^2 being the unit of the GDD coefficient. As with the gain filter operator, the GDD operator is applied to the pulse in the frequency domain through use of a Fourier transform.

Cavity loss is modeled as the accumulated total of all sources of loss within the laser cavity, including mirror losses, nonsaturable absorption within the SESAM, and various defects within the VECSEL chip. This operator functions in the time domain and is represented simply as

$$L = exp[-l_0] \tag{3.29}$$

where l_0 is the total loss of the cavity.

Finally, an operator is necessary to initiate the pulse formation process and another operator is necessary to keep the pulse centered on the time grid. The initial pulse operator definition can be modeled as either random noise, or as a small Gaussian-shaped "starter" pulse if computation time is of concern. In the case of a small Gaussian input, we have modeled the starter pulse as

$$Gaussian\ Input = A\,exp\left[-\frac{1}{2}\left(\frac{T}{T_0}\right)^2\right] \tag{3.30}$$

where A is a small scalar, T is the time grid, and T_0 is the pulse width. The centering operator is necessary because the saturable absorber will absorb the leading edge of each pulse, causing the pulse to shift backwards continuously if not re-centered after each pass [8].

3.2.3 Pulse Formation Models

For the following example pulse simulations, a set of parameters was compiled that is a combination of known values and approximations based on typical values available in literature and can be observed in Table 3.1. Stable pulse formation is demonstrated in Fig. 3.9 with an initial pulse definition that was a very weak starter pulse. After approximately 700 passes in the resonator cavity, a stable pulse has been formed. In Fig. 3.10, noise is used to initiate the pulse formation. Stability is reached much faster because the order of magnitude of the noise is larger than that of the weak starter pulse.

Pulse Simulation Parameters	
GDD Parameter	2000 fs^2
Cavity Loss	3%
Cavity Gain	10%
Recombination Time (VECSEL)	2 ns
Recombination time (SESAM)	15 ps
Saturation Energy (VECSEL)	20e^{-8} J
Saturation Energy (SESAM)	4e^{-8} J
Linewidth Enhancement Factor (VECSEL)	3
Linewidth Enhancement Factor (SESAM)	1
Modulation Depth	1%
Gain Bandwidth	30 nm
Reference Wavelength	1064 nm

Table 3.1: Pulse simulation parameters for demonstration of stable pulse formation.

Fundamental Pulse
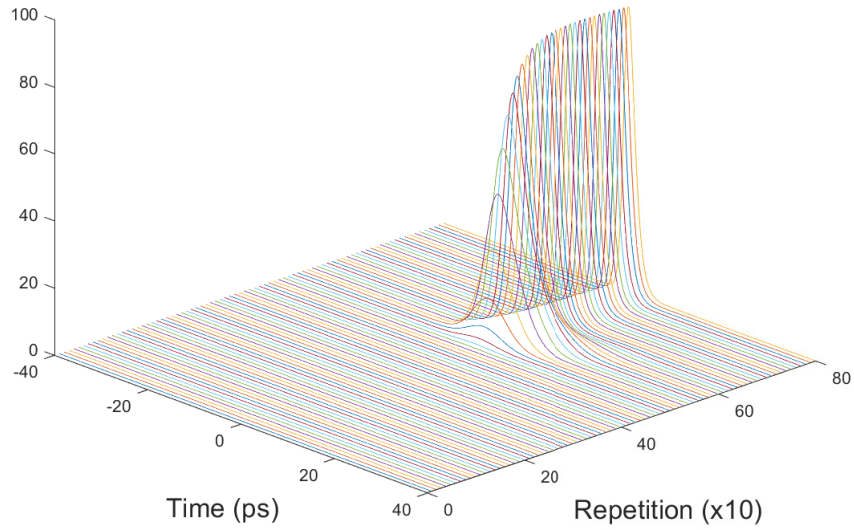
Figure 3.9: Stable pulse formation with the simulation initiated with a weak "starter" pulse.

Fundamental Pulse
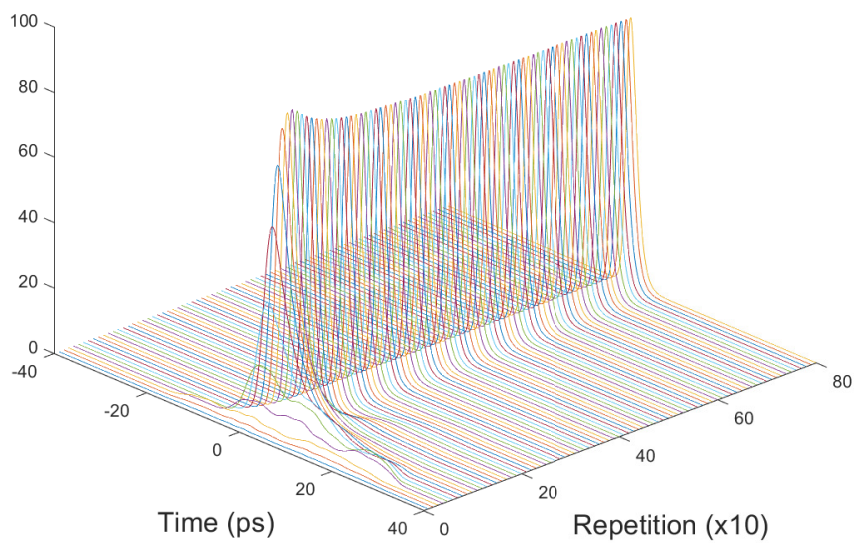
Figure 3.10: Stable pulse formation with the simulation initiated with noise.

Chapter 4

Nonlinear Frequency Conversion

4.1 Second Harmonic Generation

The earliest demonstration of nonlinear optical phenomena was second harmonic generation by Franken *et al.* in 1961 [76]. They demonstrated that certain optical properties of a material could be modified by a sufficiently strong optical field. This opened a floodgate into the exploration and development of laser sources and materials that could be combined with nonlinear frequency conversion processes to target specific wavelength regions that are difficult, or impossible, to reach directly with existing gain media at fundamental wavelengths [18, 19, 77–79].

Starting from Maxwell's Equations for an electric field $\vec{E}$ and magnetic field $\vec{H}$ in a medium,

$$\nabla \cdot \vec{D} = \rho \tag{4.1}$$

$$\nabla \cdot \vec{B} = 0 \tag{4.2}$$

$$\nabla \times \vec{E} = -\frac{\partial \vec{B}}{\partial t} \tag{4.3}$$

$$\nabla \times \vec{H} = \vec{J} + \frac{\partial \vec{D}}{\partial t} \tag{4.4}$$

where ρ is the charge density, $\vec{J}$ is the current density, and $\vec{D}$ and $\vec{B}$ are the electric and magnetic flux densities, respectively [75, 80]. These flux densities are related to the magnetization density $\vec{M}$, polarization density $\vec{P}$, permittivity of free space

ϵ_0, and permeability of free space μ_0, by equations

$$\vec{D} = \epsilon_0 \vec{E} + \vec{P} \tag{4.5}$$

$$\vec{B} = \mu_0(\vec{H} + \vec{M}). \tag{4.6}$$

For nonlinear frequency conversion in typical nonmagnetic optical media, there are no free currents or charges. This results in $\vec{M} = \vec{J} = \rho = 0$. Furthermore, $\vec{P}$ can be expressed by a power series expansion as

$$\vec{P} = \epsilon_0[\chi^{(1)} \vec{E} + \chi^{(2)} \vec{E}^2 + \chi^{(3)} \vec{E}^3 + ...\chi^{(n)} \vec{E}^n] \tag{4.7}$$

$$\vec{P} = \vec{P_L} + \epsilon_0[\chi^{(2)} \vec{E}^2 + \chi^{(3)} \vec{E}^3 + ...\chi^{(n)} \vec{E}^n] \tag{4.8}$$

$$\vec{P} = \vec{P_L} + \vec{P_{NL}} \tag{4.9}$$

where $\chi^{(n)}$ is the optical susceptibility of the material. For second harmonic generation, the second-order nonlinear susceptibility $\chi^{(2)}$ is of primary interest which results in $\vec{P}$ being expressed as

$$\vec{P} = \vec{P}_{NL} = \vec{P}^{(2)}(z,t) = \epsilon_0 \chi^{(2)} \vec{E}^2(z,t) \tag{4.10}$$

with the electric field represented as

$$\vec{E}(z,t) = \vec{E}_1(z,t) + \vec{E}_2(z,t) \tag{4.11}$$

where $\vec{E}_1$ is the pump pulse and $\vec{E}_2$ is the second harmonic generated wave. The nonlinear polarization and electric field satisfy the wave equation in nonlinear optical media given by

$$\nabla^2 \vec{E} - \left(\frac{n^2}{c^2}\right)\frac{\partial^2 \vec{E}}{\partial t^2} = \left(\frac{1}{\epsilon_0 c^2}\right)\frac{\partial^2 \vec{P}_{NL}}{\partial t^2} \tag{4.12}$$

where n and c are the refractive index of the material and the speed of light,

respectively. The pump and second harmonic waves can be described by

$$\vec{E}_1 = \left(\frac{1}{2}\right)\left[A(z,t)\exp\left[-i(\omega t - k_1 z)\right] + c.c.\right] \tag{4.13}$$

$$\vec{E}_2 = \left(\frac{1}{2}\right)\left[B(z,t)\exp\left[-i(2\omega t - k_2 z)\right] + c.c.\right]. \tag{4.14}$$

Using these equations, we can solve for the wave equations for fundamental and second harmonic pulse envelope functions [80, 81]. These pulse envelope functions form the basis for the operator required to model second harmonic generation and are represented as

$$\frac{\partial A}{\partial z} + \frac{1}{\nu_1}\frac{\partial A}{\partial t} = i\beta_1 A * B\exp\left(-i\Delta k z\right) \tag{4.15}$$

$$\frac{\partial B}{\partial z} + \frac{1}{\nu_2}\frac{\partial B}{\partial t} = i\beta_2 A^2 \exp\left(i\Delta k z\right) \tag{4.16}$$

where ν_1 and ν_2 are the group velocities of the fundamental and second harmonic, respectively. The constants β_1 and β_2 are expressed as

$$\beta_1 = \frac{2i\omega_1^2 d_{eff}}{k_1 c^2} \tag{4.17}$$

$$\beta_2 = \frac{i\omega_2^2 d_{eff}}{k_2 c^2} \tag{4.18}$$

where ω_1 is the fundamental frequency, ω_2 is the second harmonic frequency, and k_1 and k_2 are the angular wavenumbers of the fundamental and second harmonic, respectively. The degree of phase matching is expressed by $\Delta k = 2k_1 - k_2$. The constant d_{eff} is known as the effective nonlinear coefficient and varies according to the optical media used. Solving the set of coupled equations 4.15 and 4.16 will yield the propagation behavior of the fundamental and second harmonic pulses through a nonlinear medium.

4.2 Angle Phase Matching

The efficiency of the second harmonic process is driven by phase matching, which is the extent to which the polarization of the second harmonic is in phase with the fundamental that created it [82]. For the second harmonic process observed in Fig. 4.1, phase matching is achieved when $\Delta k = 0$, which requires that $n(\omega_F) = n(\omega_{SHG})$.
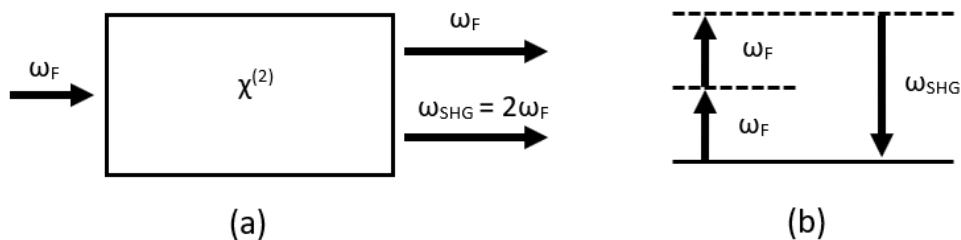
Figure 4.1: The nonlinear second harmonic process observed in (a) results in the generation of a fundamental photon with twice the frequency of the fundamental that created it. The energy schematic in (b) demonstrates the conservation of energy in this process.

It is difficult to find a material that satisfies the phase matching condition required for efficient second harmonic generation since, under normal dispersion, the refractive index increases for increasing frequency. However, special materials that exhibit birefringence are able to accomplish this by providing different refractive indices along different crystal axes, where the polarization of the higher frequency wave is aligned along the direction of a lower refractive index, and the polarization of the lower frequency wave is aligned along the direction of a higher refractive index. Nonlinear optical crystals are classified based on the relationship between their refractive index components n_x, n_y, n_z along the x, y, z coordinate directions, as observed in Table 4.1 and Fig. 4.2.

For the purposes of this dissertation, we focus on Type I second harmonic generation (SHG) where the two lower frequency fundamental components in $\omega_1 \leq \omega_2 < \omega_3$ have the same polarization state, with the second harmonic frequency having an orthogonal polarization state. For completeness, Type II occurs

	Uniaxial	**Biaxial**
Positive	$n_x = n_y < n_z$	$n_x < n_y < n_z$
Negative	$n_x = n_y > n_z$	$n_x > n_y > n_z$

Table 4.1: Classification of nonlinear optical crystals that exhibit different refractive indices along the different coordinate axes.
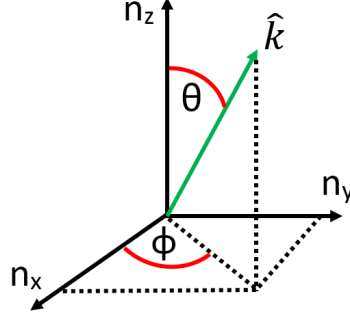
Figure 4.2: General layout of the refractive indices within a biaxial crystal with wave propagation in direction k.

when these two lower frequency components have orthogonal polarization states. Following a renaming convention where, considering the direction of propagation in a biaxial or uniaxial crystal, there will exist two refractive indices n_{fast} and n_{slow} where $n_{fast} < n_{slow}$ [83]. This results in phase matching for Type I SHG when

$$n_{SHG}^{(fast)} \omega_{SHG} = 2 n_{fund}^{(slow)} \omega_{fund} \tag{4.19}$$

with $\omega_{fund} < \omega_{SHG}$.

Exploiting the benefits of angle phase matching within a birefringent nonlinear optical crystal requires aligning the polarization direction of the fundamental and second harmonic waves that results in $\Delta k = 0$. Lithium triborate (LBO) is commonly used for second harmonic generation of visible wavelengths and is classified as a negative biaxial crystal, where $n_x \neq n_y \neq n_z$ and θ is 90°, resulting in the wave propagation vector k being in the n_x, n_y plane and angle ϕ defining the difference in refractive index between the fundamental and second harmonic waves. For beta

barium borate (BBO) crystals, which are frequently used for frequency doubling to the UV spectral region, ϕ is $0°$ and the wave propagation is in the n_x, n_z plane. This flexibility enables angle phase matching using different materials to target different spectral regions for second harmonic generation.

4.3 Considerations for Ultrashort Pulses

4.3.1 Group Velocity Dispersion

Ultrashort pulses that have a duration less than several picoseconds can experience significant perturbation from propagation through a transparent nonlinear optical crystal. This can be most readily seen by applying a Taylor series expansion to the propagation vector k, resulting in [75, 80]

$$k(\omega) = k(\omega_0) + \frac{dk}{d\omega}(\omega - \omega_0) + \frac{1}{2}\frac{d^2k}{d\omega^2}(\omega - \omega_0)^2 + \cdots \qquad (4.20)$$

where we assign k_1 and k_2 to represent the derivatives

$$k_1 = \left(\frac{dk}{d\omega}\right)_{\omega=\omega_0} \qquad (4.21)$$

and

$$k_2 = \left(\frac{d^2k}{d\omega^2}\right)_{\omega=\omega_0}. \qquad (4.22)$$

When considering the propagation of an individual pulse, the major effect is group velocity dispersion (GVD). This describes the dependence of the group velocity ν_g, on the optical frequency ω, expressed as

$$\frac{1}{\nu_g(\omega_0)} = \left(\frac{dk}{d\omega}\right)_{\omega=\omega_0} = k_1 \qquad (4.23)$$

$$GVD = \left(\frac{d^2k}{d\omega^2}\right)_{\omega=\omega_0} = \frac{d}{d\omega}\left(\frac{1}{v_g(\omega)}\right)_{\omega=\omega_0}. \qquad (4.24)$$

Ultrashort pulses can possess a large frequency bandwidth, with each frequency component having a slightly different group velocity. This results in temporal broadening of the pulse as a result of the group velocity dispersion as the pulse propagates through the dispersive medium. Under normal dispersion, the GVD effect diminishes for smaller optical frequencies (longer wavelengths). This is crucial for second harmonic generation, since the harmonic will experience a greater effect of GVD than the fundamental that created it, potentially resulting in a broadened second harmonic pulse duration compared to the fundamental.

4.3.2 Group Velocity Mismatch

While each pulse can experience temporal broadening by GVD within a dispersive medium, it is also important to consider the potential broadening of the second harmonic pulse as a result of "walking away" from the fundamental pulse while propagating through a medium. This is the result of the fundamental and second harmonic pulses having different group velocities, with group velocity mismatch (GVM) expressed as the difference between these group velocities, or [75, 84]

$$GVM = \frac{1}{v_{g,1}} - \frac{1}{v_{g,2}} = \Delta(v_g^{-1}). \qquad (4.25)$$

The temporal effect of GVM is equivalent to the frequency domain phase matching bandwidth. The effect that GVM has on second harmonic pulse broadening is characterized by the temporal walk-off length, or quasistatic interaction length (L_{qs}), which defines the distance over which one pulse temporally separates from the other, expressed as

$$L_{qs} = \frac{\tau}{GVM} = \frac{\tau}{|\Delta(v_g^{-1})|} \qquad (4.26)$$

where τ is the pulse duration. This parameter is material dependent and limits the length of crystal that can be used for second harmonic generation without substantially increasing the pulse duration.

4.4 Second Harmonic Pulse Modeling

The pulse simulation code developed for modeling stable pulse formation of the fundamental can be expanded to also model single pass second harmonic generation. For every pass through the resonator cavity, the SHG operator takes the incoming pulse field and propagates it through the nonlinear crystal. The operator uses a split-step method to solve the coupled equations 4.15 and 4.16 and accounts for the effects of GVD and GVM. These effects are applied in frequency space to the Fourier transform of the fundamental and second harmonic pulses and are expressed as

$$\Gamma_F = \exp\left(\frac{-iD_F\omega^2\Delta z}{2}\right) \tag{4.27}$$

and

$$\Gamma_{SHG} = \exp-\left(\frac{iD_{SHG}\omega^2\Delta z}{2} + i\omega\Delta(v_g^{-1})\Delta z\right) \tag{4.28}$$

where D_F and D_{SHG} are the GVD coefficients for the fundamental and second harmonic, respectively, and Δz is the propagation step through the nonlinear optic. Finally, ω is the frequency domain equivalent of the time grid.

The following simulations observed in Figs. 4.3 and 4.4 demonstrate the capability of the code to model stable pulse formation with the inclusion of a nonlinear optical crystal within the cavity. They were performed with the same set of parameters collected from literature and material specification sheets. It is important to note that these simulations are not modeling exact behavior we expect to measure from an actual experiment, but rather demonstrate that stable mode locking is possible within a certain parameter space.

Fundamental Pulse
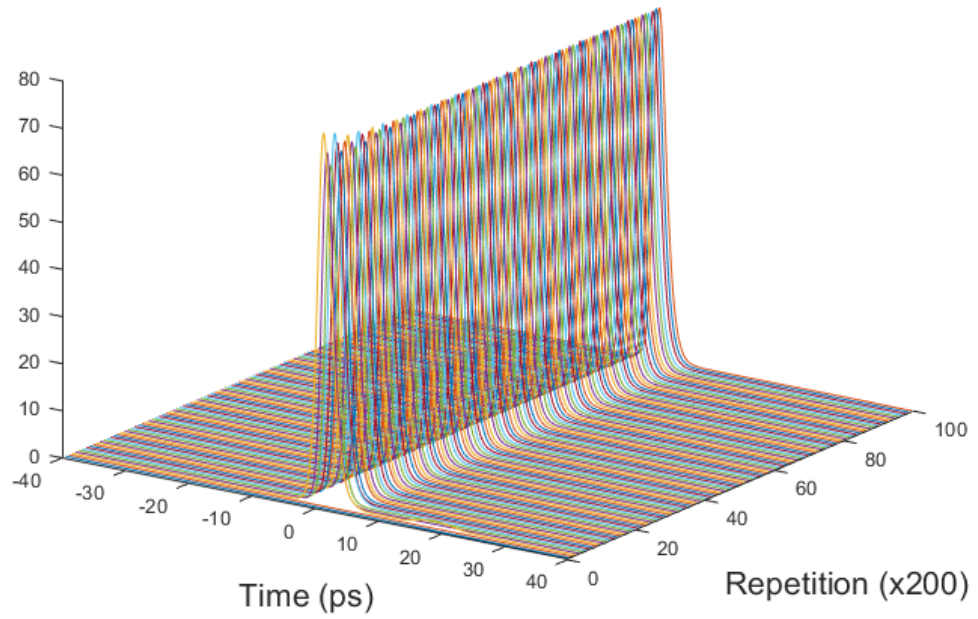
Figure 4.3: Demonstration of stable fundamental pulse formation with a nonlinear optic in the cavity.

Second Harmonic Pulse
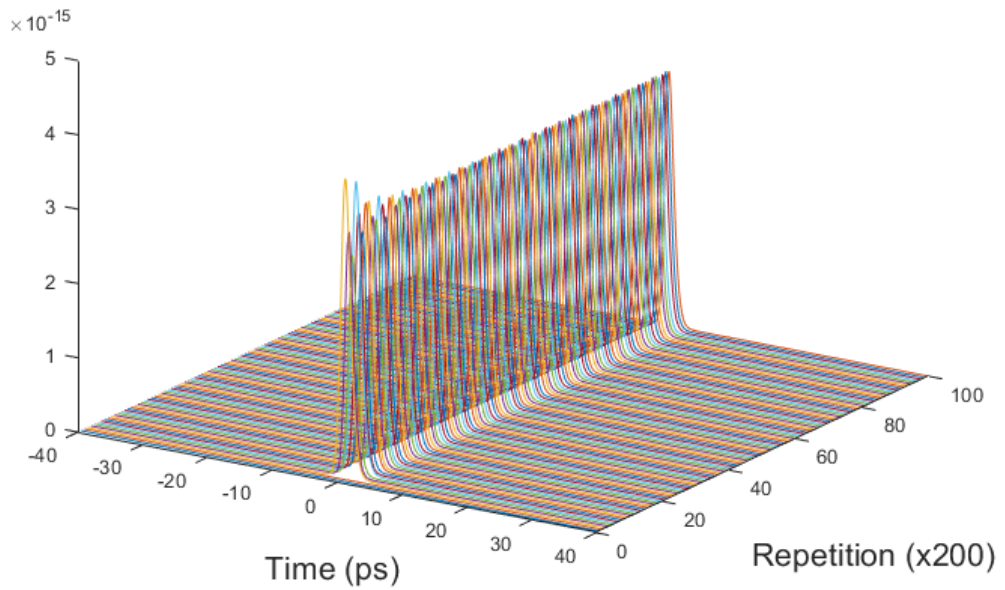
Figure 4.4: Simulation of single pass second harmonic generation. The SHG pulse behavior follows that of the fundamental.

Chapter 5

High Peak Power Second Harmonic Generation in an Ultrafast VECSEL

5.1 Brief History

As discussed in Chapter 2, passively mode locked VECSELs have been demonstrated to be capable of delivering multi-watt average output power, kilowatt peak pulse power, multi-GHz repetition rates, and ultrashort pulses in the picosecond to femtosecond range. However, the majority of this work was accomplished at fundamental wavelengths in the 900-1550 nm spectral region using the GaAs and InP material systems. The limits of available gain material for direct access to UV, visible, and mid-IR wavelengths has seen the proliferation of nonlinear frequency conversion methods to access these otherwise inaccessible spectral regions under continuous wave operation. Band gap engineering of the VECSEL gain chip adds additional flexibility in targeting a specific wavelength when combined with these nonlinear processes. However, intracavity frequency conversion in a passively mode locked VECSEL remains a relatively unexplored area.

There are a few important reasons for why intracavity frequency conversion has seen limited growth in a passively mode locked VECSEL. First, nonlinear optical crystals add dispersion to the resonator which can lead to substantial pulse

broadening, especially for ultrashort pulses in the femtosecond region. Second, the pulses need to be aligned spatially and temporally at the entry facet of the crystal for any frequency conversion process to occur. Third, especially for second harmonic generation, the harmonic will have a different group velocity which will see it walk off from the fundamental which can also result in pulse broadening. The last major consideration is depletion of the fundamental within the resonator through a highly efficient conversion process. Passively mode locked VECSELs have dynamic gain which needs to be carefully balanced against the saturable loss of the SESAM. Strong depletion of the fundamental has the potential to destabilize the mode lock as a result of the crystal absorbing the most intense portion of the pulse, which will change the bleaching behavior of the SESAM.

Intracavity second harmonic generation (SHG) in a passively mode locked VECSEL has only been previously demonstrated twice. The first demonstration in 2005 used an InGaAs-based gain chip in a V-cavity configuration with the SESAM as an end mirror [85]. They placed the 5 mm LBO crystal in front of the SESAM for intracavity SHG of 489 nm. They were only able to generate 6 mW at this wavelength. The second demonstration game a decade later with an AlGaInP-based gain chip in a V-cavity configuration [86]. This group also placed their nonlinear crystal (BBO) in front of the SESAM for intracavity SHG of 325 nm. Their power at the second harmonic was only 0.5 W.

The primary issue with both of these approaches involves placing the nonlinear optical crystal in front of the SESAM. In the V-cavity geometry that was used, the SESAM is at the position of the smallest beam waist. If the SESAM was an ordinary flat mirror, this would be the ideal location for the crystal for efficient SHG. However, the DBR within the SESAM is not designed for reflection at the second harmonic, and, instead, will absorb it. This can lead to damage of the SESAM and eventual failure from thermal effects if the generated second harmonic is too intense. The solution is to place the nonlinear optic in a separate arm from the SESAM in a cavity optimized for passive mode locking simultaneously with

highly efficient SHG. This work was funded by the National Science Foundation grant (1709918).

5.2 W-Cavity Resonator Design and Optimization

The ideal resonator cavity design for intracavity second harmonic generation in a passively mode locked VECSEL is a W-cavity configuration, as observed in Fig. 5.1. This cavity can be designed to be symmetric, with similar arm lengths for L1 and L3, which results in a similar small beam waist at the SESAM and M1. This design also allows for the arbitrary placement of the VECSEL chip along L2 in order to achieve the desired mode area ratio for stable passive mode locking, as observed in the Gaussian beam simulation in Fig. 5.2. Finally, we can take advantage of gain bandwidth enhancement by folding the cavity off of the chip. With the LBO crystal placed at the beam waist in front of a high reflectivity mirror M1, we are able to achieve double-pass SHG for increased conversion to the harmonic with full extraction out of the resonator through output coupler mirror M2. A small portion of the circulating fundamental can be extracted through mirror M3 for separate characterization of the fundamental and second harmonic beams.
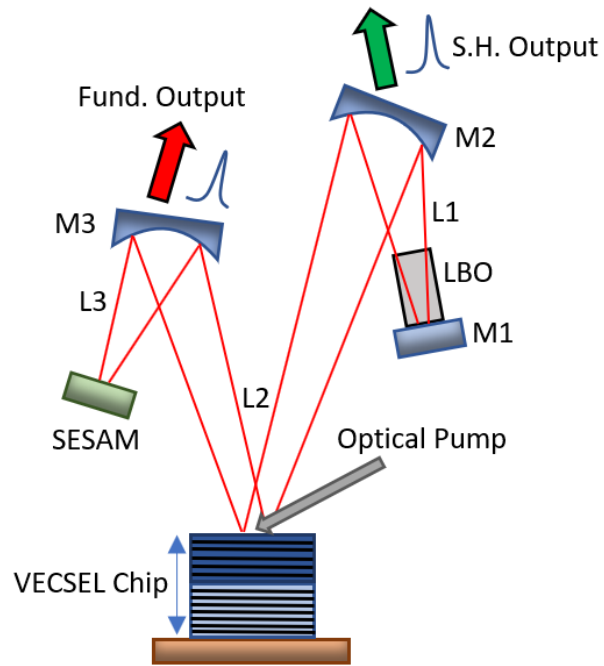
Figure 5.1: Schematic of the W-cavity resonator used for high peak power second harmonic generation.
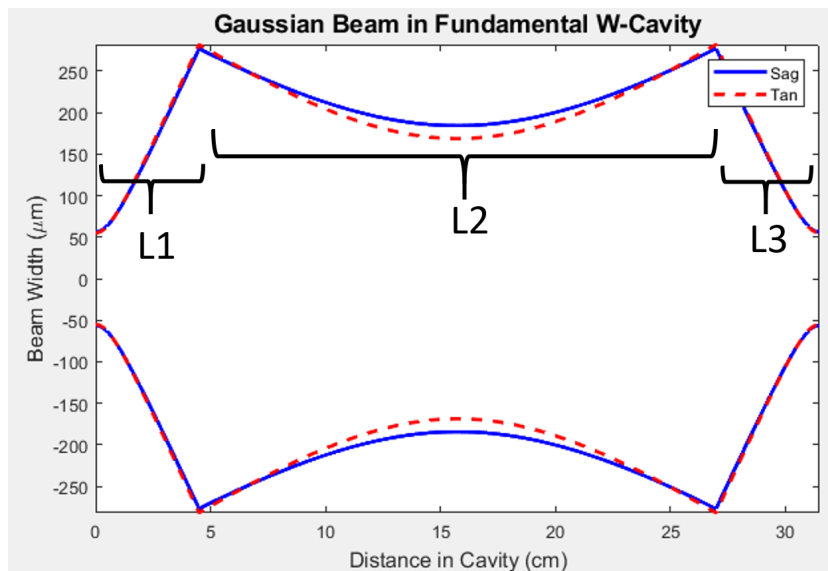
Figure 5.2: Simulation of the Gaussian beam within the W-cavity resonator. Note that the cavity is symmetric with similar beam diameters at both ends.

A W-cavity following the layout in Fig. 5.1 was first designed and simulated. Mirror M1 was a broadband flat mirror with 99.9% reflectivity from 400-1200 nm. Mirrors M2 and M3 have similar 7.5 cm radii of curvature with 99.9% reflectivity at ~1064 nm. Mirror M2 also has an anti-reflectivity coating at ~532 nm to allow for complete extraction of the second harmonic from the cavity. The SESAM used has a modulation depth ΔR of 4%, nonsaturable loss of 1%, and a 15 ps recovery time. The 5x4x4 (LxWxH) LBO crystal has both facets AR coated at 1064 nm and 532 nm. The VECSEL chip is a strain-compensated InGaAs/GaAs/GaAsP multi-quantum well semiconductor heterostructure with DBR designed for emission at ~1070 nm. The active region consists of 12 compressively strained quantum wells sandwiched between GaAs/GaAsP barriers and the DBR section consists of 25 pairs of alternating AlGaAs/AlAs layers for 99.9% reflectivity. The processed chip was clamped to a copper water block maintained at a temperature of 10°C and pumped with a fiber-coupled 808 nm diode laser with a spot diameter on the chip of ~500 μm.

As can be observed in Fig. 5.2, the Gaussian beam is symmetric with beam waists of ~110 μm at both M1 and the SESAM when L1 and L3 are 4.5-5 cm long and L2 is 22.5 cm long. The chip will be placed approximately 5 cm in front of M3 for a beam diameter of ~440 μm, which results in a mode area ratio of 14-15, which is in the ideal range for passive mode locking. Pulse stability was simulated for single pass intracavity SHG and can be observed in Fig. 5.3. It is again important to note that the pulse simulations demonstrate that stable mode locking is expected for both the fundamental and second harmonic with slight broadening of the second harmonic. However, the simulation is not a prediction of exact pulse shape or duration.
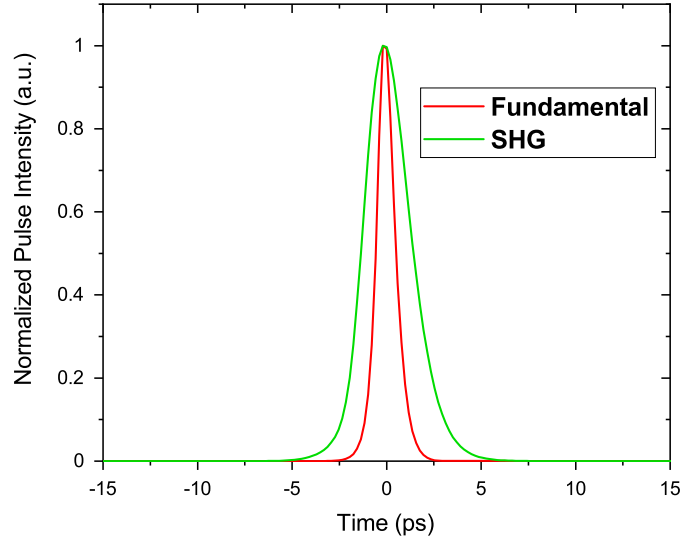
Figure 5.3: Pulse simulations for both the fundamental and second harmonic. The second harmonic is expected to broaden from the fundamental pulse width.

5.3 Experimental Results

5.3.1 Fundamental Characterization

The W-cavity was constructed and tested first without the LBO crystal in order to characterize the fundamental pulse [87]. The pulse was measured on an APE pulsecheck 150 autocorrelator with a sech^2 function fit to the data which demonstrates a full width at half maximum (FWHM) pulse duration of ∼700 fs, as observed in Fig. 5.4. The repetition of the frequency was measured to be approximately 465 MHz, as observed in Fig. 5.5, which is in good agreement with the cavity design of 460-470 MHz. The absence of any secondary peaks in the RF spectral plot, along with a stable pulse measurement, is an indicator of a stable mode lock. The optical spectrum of fundamental pulse was centered at ∼1057 nm, as seen in Fig. 5.6, which demonstrates a blue shift of the fundamental from the chip design wavelength. This is an indicator of an up-chirped pulse as the optical spectrum drifts from the gain maximum as a result of the SESAM absorbing the low frequency components of the leading edge of the pulse [42]. The average

output power of the fundamental was measured to be 180 mW, which results in a peak pulse power of ∼490 W.
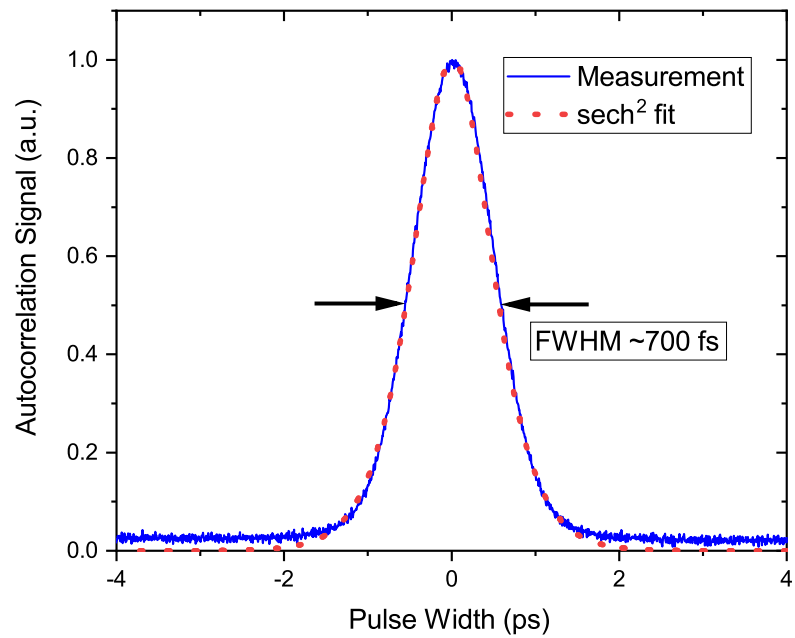
Figure 5.4: Fundamental pulse measurement demonstrating a FWHM pulse duration of 700 fs.
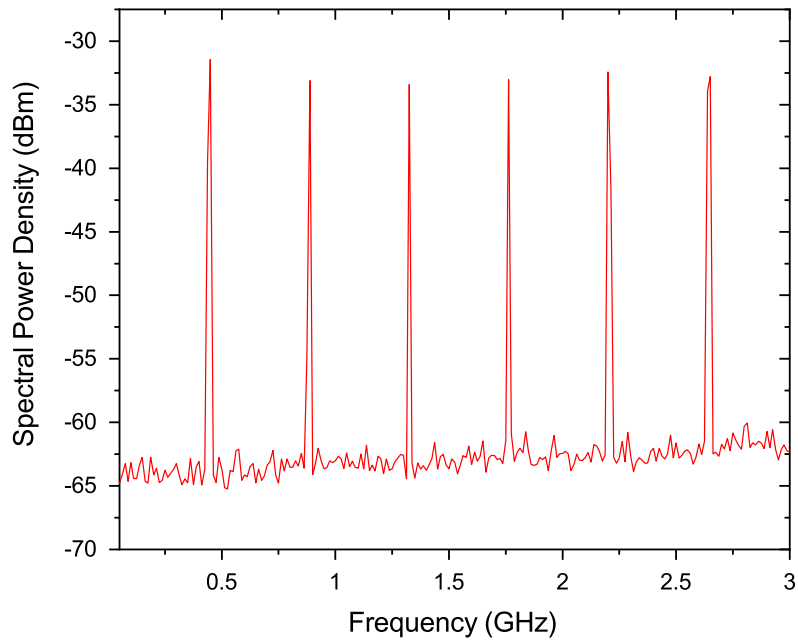
Figure 5.5: RF spectrum of the fundamental demonstrating a repetition frequency of 465 MHz.
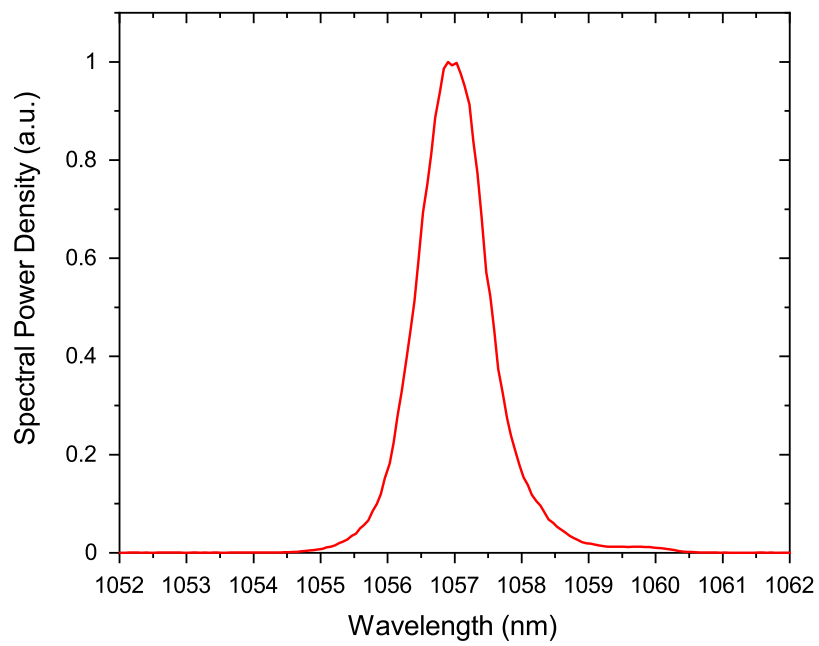
Figure 5.6: Optical spectrum of the fundamental centered at 1057 nm.

5.3.2 Second Harmonic Characterization

With the fundamental fully characterized, the LBO crystal was inserted into the cavity in front of mirror M1 and adjusted for phase matching and pulse stability. When the crystal was moved close to M1 for tight focusing and greater conversion to the second harmonic, the mode lock began to destabilize. This was most likely the result of strong depletion of the fundamental, which changed the gain/loss dynamics between the chip and SESAM. The crystal was adjusted to maintain operation within the weak saturation regime to avoid this issue. A picture of the operational W-cavity can be observed in Fig. 5.7.
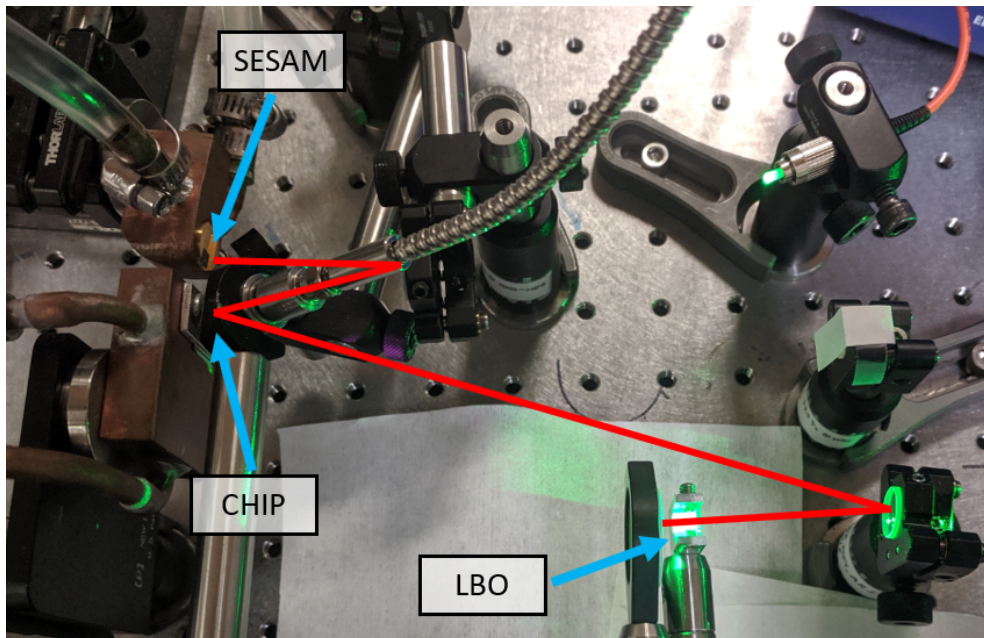
Figure 5.7: Picture of the operational W-cavity with intracavity LBO crystal for second harmonic generation. The red lines denote the W-cavity resonator path.

The second harmonic pulse was measured and fit with a sech^2 function that demonstrates a FWHM pulse duration of $\sim$760 fs, as observed in Fig. 5.8. For a LBO crystal with a 700 fs fundamental pulse duration and a GVM coefficient of 44 fs/mm between the fundamental and second harmonic, the quasistatic interaction length is 16 mm. A 10 mm LBO crystal length (double pass with an actual 5 mm crystal length) is well below this criteria, so pulse broadening was not expected and is likewise not substantially present in Fig. 5.8. The repetition

rate of the second harmonic matched that of the fundamental, with its optical spectrum centered near 528 nm, as observed in Figs. 5.9 and 5.10, respectively. The measured average output power of the second harmonic was ~230 mW, which resulted in a record-setting peak pulse power of 580 W in a passively mode locked VECSEL utilizing intracavity SHG. This is a substantial improvement over the previously reported results and demonstrates the potential for intracavity SHG in an optimal cavity design.
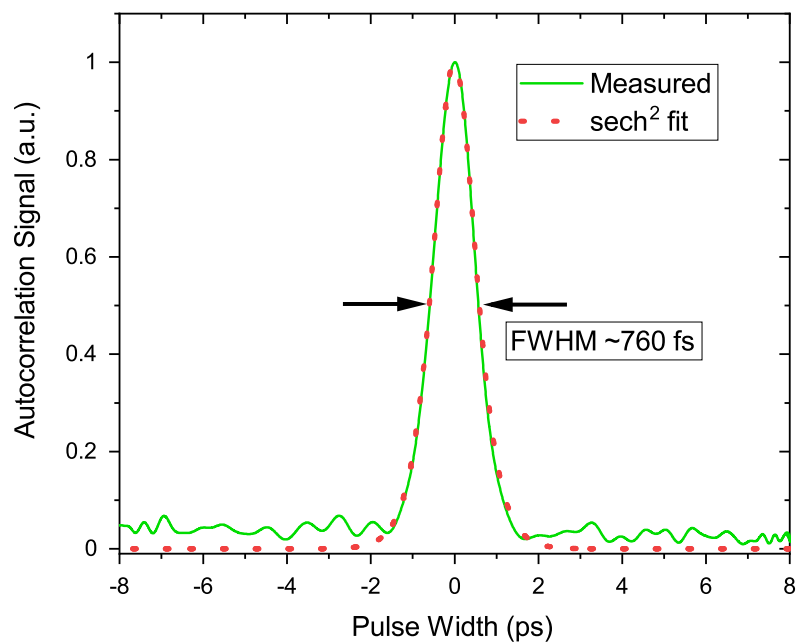
Figure 5.8: Fundamental pulse measurement demonstrating a FWHM pulse duration of 760 fs, which is slightly broader than the fundamental.
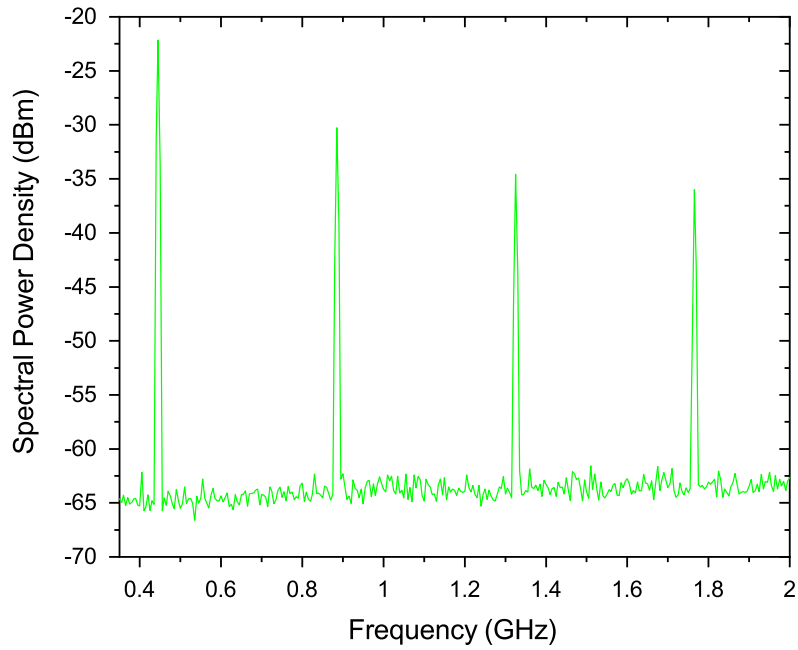
Figure 5.9: RF spectrum of the second harmonic demonstrating a repetition frequency of 465 MHz, which matches that of the fundamental.
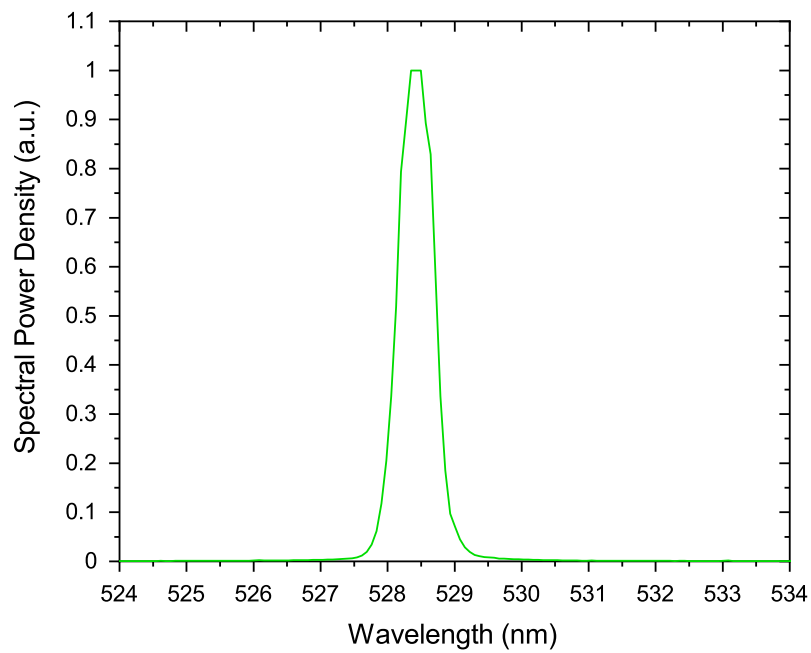
Figure 5.10: Optical spectrum of the second harmonic centered at 528.5 nm.

While the second harmonic result was record-setting, it is still possible to improve it further. The beam waist was approximately 110 μm at the LBO crystal. However, for ideal second harmonic generation, the calculated beam waist should be approximately 60 μm. As mentioned previously, tighter focusing in the crystal could result in destabilization of the mode lock caused by strong depletion of the pump beam. This could be compensated by replacing output coupler mirror M3 with a high reflectivity mirror at the fundamental wavelength, which would reduce the total cavity loss by 2%. Furthermore, the entire cavity can be scaled down in size to make it more compact while still maintaining the symmetry needed.

Chapter 6

All-Intracavity Fourth Harmonic Generation in an Ultrafast VECSEL for Deep UV Emission

6.1   Brief History

There is growing demand for ultrafast laser sources operating in the deep UV spectral region near 266 nm for applications involving chemistry, biology, medicine, and other industrial applications [88, 89]. These lasers are almost exclusively based on decades-old technology involving Excimer and Ti:Sapphire lasers, or more recently developed Yb-doped fiber lasers [90–94]. This existing laser technology always involves a trade-off in terms of performance metrics (e.g. femtosecond pulses at low MHz repetition rates, or high output power with nanosecond pulses), are excessively large, or expensive. Furthermore, active stabilization equipment is commonly used which adds additional size and cost to ultrafast UV lasers.

A passively mode locked VECSEL emitting in the deep UV spectral region through all-intracavity fourth harmonic generation can provide an alternative to this existing technology. The published work discussed in Chapter 5 demonstrates the capability of intracavity second harmonic generation. This work was expanded upon by enclosing the high output power of the second harmonic within its own high Q Z-cavity resonator for power enhancement. The inclusion of a beta barium

borate (BBO) crystal within the Z-cavity allows for second harmonic generation of the circulating "green" pulse, effectively frequency quadrupling the initial fundamental pulse. This work was funded by the National Science Foundation grant (1709918).

6.2   Overlapped Resonator Cavity Design

The VECSEL designed for ultrafast deep UV emission can be observed in Fig. 6.1. The fundamental is enclosed in a W-cavity resonator (red lines) with the second harmonic enclosed in a Z-cavity resonator (green lines). The SESAM has a 15 ps recovery time, modulation depth ΔR of 3%, 1% nonsaturable loss, and was maintained at a temperature of 20°C.
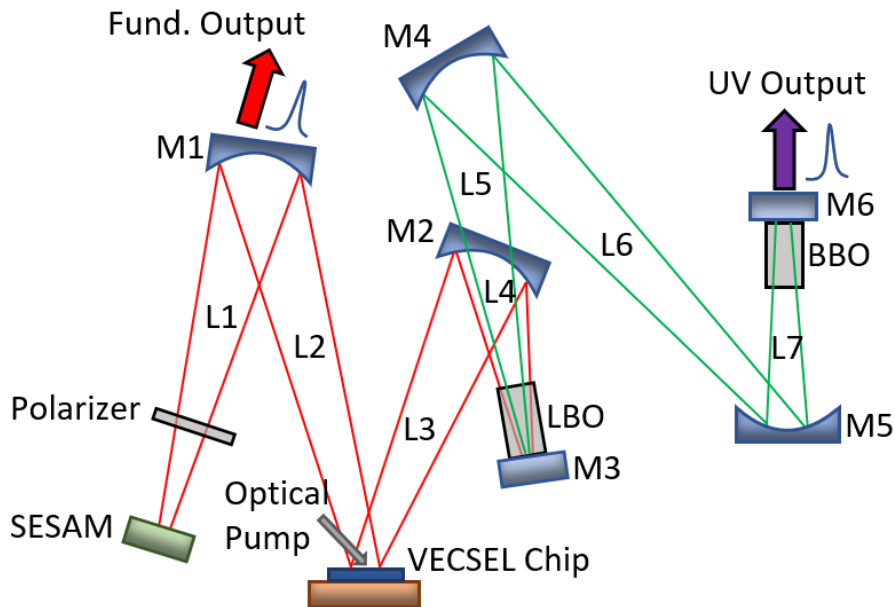
Figure 6.1: Schematic of the overlapped fundamental W-cavity (red lines) and second harmonic Z-cavity (green lines). The two cavities were designed to be symmetric.

Mirror M1 has a radius of curvature (RoC) of 10 cm with a ~99% reflectivity coating at 1064 nm. Mirror M2 has a 5 cm RoC with an high reflectivity (HR) coating at 1064 nm and an anti-reflectivity (AR) coating at 532 nm. Mirror M3 is a flat mirror with a broadband HR coating from 400-1200 nm. Mirror M4 has a 10 cm RoC with an HR coating at 532 nm. Mirror M5 has a 5 cm RoC with an

HR coating at 532 nm and <10% reflectivity coating at 266 nm. Mirror M6 is a flat mirror with an HR coating at 532 nm and <10% reflectivity at 266 nm. The LBO crystal is a 5x4x4 mm (LxWxH) with facets AR coating for 1064 nm and 532 nm and the BBO crystal is 5x4x4 mm (LxWxH) with facets AR coating for 532 nm and 266 nm. A thin polarizer is included between the SESAM and M1 to force a gain preference on the fundamental beam to prevent polarization hopping while angle tuning the LBO crystal. The VECSEL chip is from the same wafer described in Chapter 5 based on InGaAs/GaAs/GaAsP with 12 compressively strained InGaAs quantum wells sandwiched between GaAs/GaAsP barrier regions, with a DBR stack containing 25 pairs of alternating AlGaAs/AlAs layers for 99.9% reflectivity at 1070 nm. The VECSEL chip was optically pumped with a fiber-coupled 808 nm diode laser focused to a 550 μm spot size with the temperature of the chip maintained at 10°C.

For the fundamental cavity, distance L1 is 6.5 cm, L2+L3 is 20 cm, and L4 is 2.5 cm. For the second harmonic cavity, distance L5 is 6.5 cm, L6 is 20 cm, and L7 is 2.5 cm. The chip was placed approximately 10.5 cm from M1 (distance L2), which resulted in a spot diameter of ∼500 μm on the chip. The spot diameter was ∼110 μm at the SESAM and M3, which results in a mode area ratio of approximately 20. As can be seen, the Z-cavity was designed to be symmetric to the W-cavity, with mirrors M1/M4 and M2/M5 having the same RoC, along with L1/L5, (L2+L3)/L6, and L4/L7 having the same length. This symmetry was necessary to ensure nearly identical cavity lengths (i.e. repetition frequency) for the W-cavity and Z-cavity for pulse overlapping of the fundamental and second harmonic at the entry facet of the LBO crystal. This symmetry also ensures that the circulating fundamental and second harmonic beams in their respective resonators have similar beam characteristics in the shared cavity length between mirrors M2 and M3 for approximate mode matching within the LBO crystal.

6.3 Experimental Results

The fundamental pulse was characterized through mirror M1 which has 1% transmission at 1070 nm. The pulse duration was measured using autocorrelation and fit with a sech^2 function which demonstrates a FWHM pulse duration of 1.4 ps, as observed in Fig. 6.2. The RF spectrum of the fundamental pulse can be observed in Fig. 6.3, which demonstrates a repetition frequency of approximately 510 MHz without any secondary peaks and is in close agreement with the calculated repetition frequency of 517 MHz. Finally, the optical spectrum of the fundamental pulse, as observed in Fig. 6.4, is centered near 1060 nm with a bandwidth of approximately 1 nm.
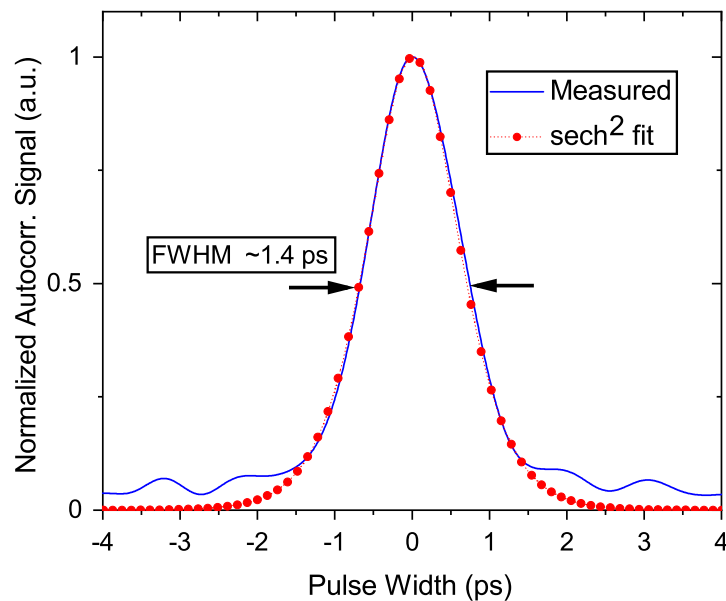
Figure 6.2: Autocorrelation measurement of the fundamental pulse. The sech^2 function fit demonstrates a FWHM pulse duration of 1.4 ps.
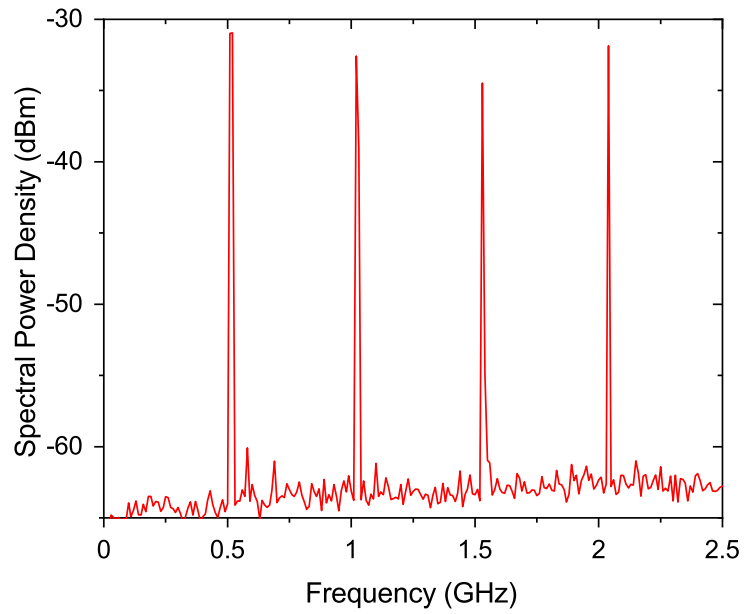
Figure 6.3: RF spectrum plot of the fundamental pulse demonstrating a repetition frequency of 510 MHz, which is in good agreement with the calculated frequency of 517 MHz.
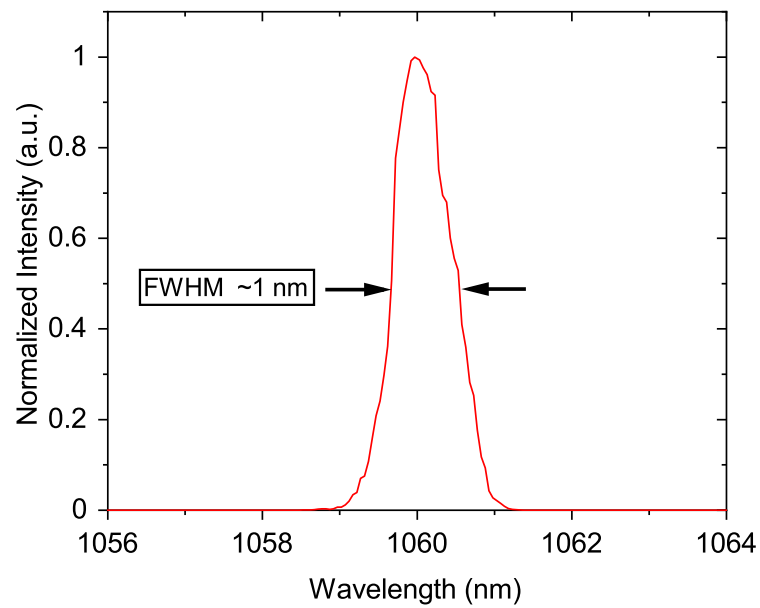
Figure 6.4: Optical spectrum of the fundamental centered near 1060 nm with a FWHM bandwidth of approximately 1 nm.

With the fundamental fully characterized, the LBO crystal was inserted into the cavity in front of mirror M3 and adjusted for phase matching and pulse stability, as seen in the Fig. 6.5 which depicts the operational W-cavity. The output power of the second harmonic was approximately 50-60 mW, which was too weak to measure with our autocorrelator with the included photodiode module. However, as was detailed in Chapter 5 and other work, the LBO crystal length is less than the quasistatic interaction length that would otherwise result in pulse broadening [49, 85, 87]. Therefore, we expect that the second harmonic pulse shape and duration to closely match that of the fundamental. After stable mode locking had been achieved with the LBO crystal, the Z-cavity was completed with mirrors M4, M5, and M6 to create the high Q resonator for the second harmonic. A small portion of the circulating second harmonic was picked off between mirrors M4 and M5 for measurement of the RF and optical spectra, which can be observed in Figs. 6.6 and 6.7, respectively. The picture in Fig. 6.8 demonstrates the power enhancement of the second harmonic in the high Q Z-cavity resonator.
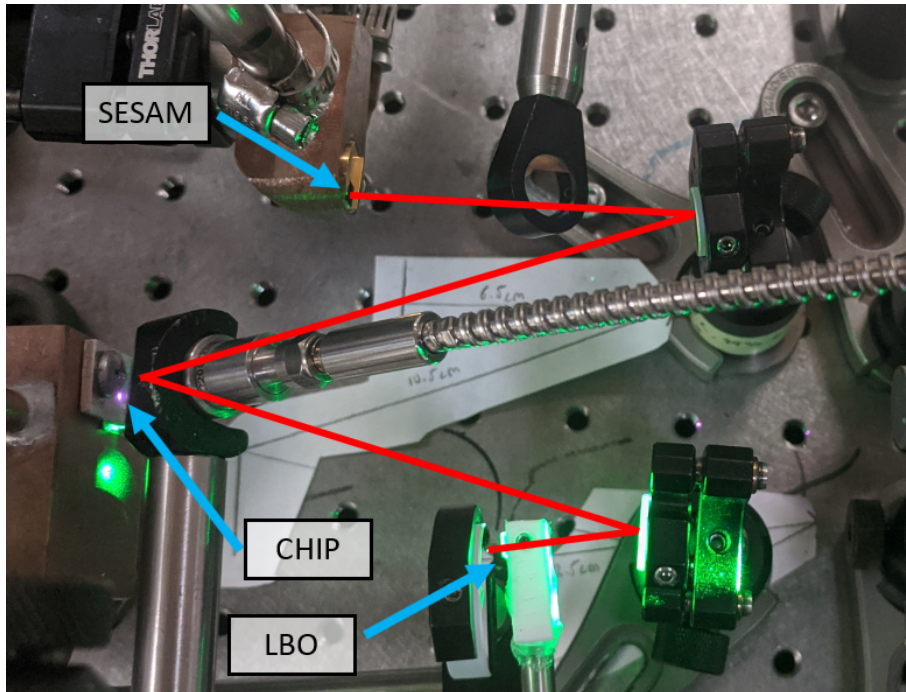
Figure 6.5: Picture of the operational W-cavity with LBO crystal inserted.
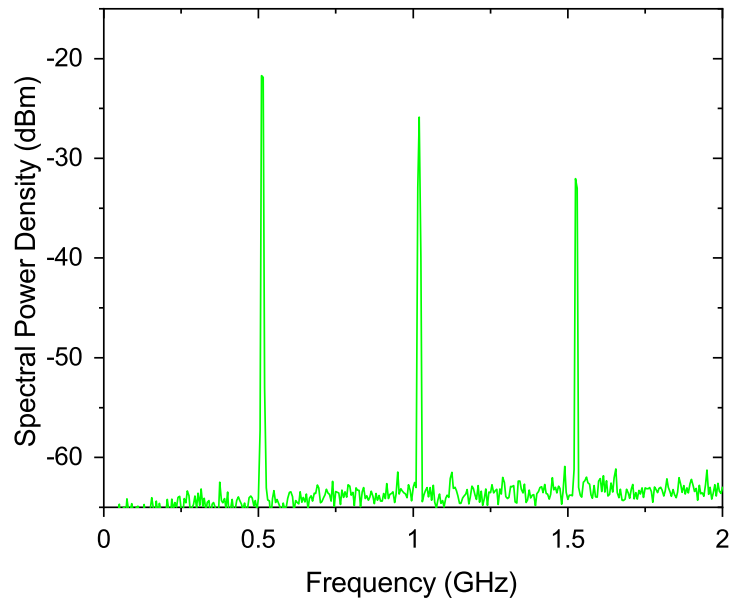
Figure 6.6: RF spectrum of the second harmonic pulse in the high Q Z-cavity resonator. The repetition was adjusted to 510 MHz to match the repetition rate of the fundamental W-cavity.
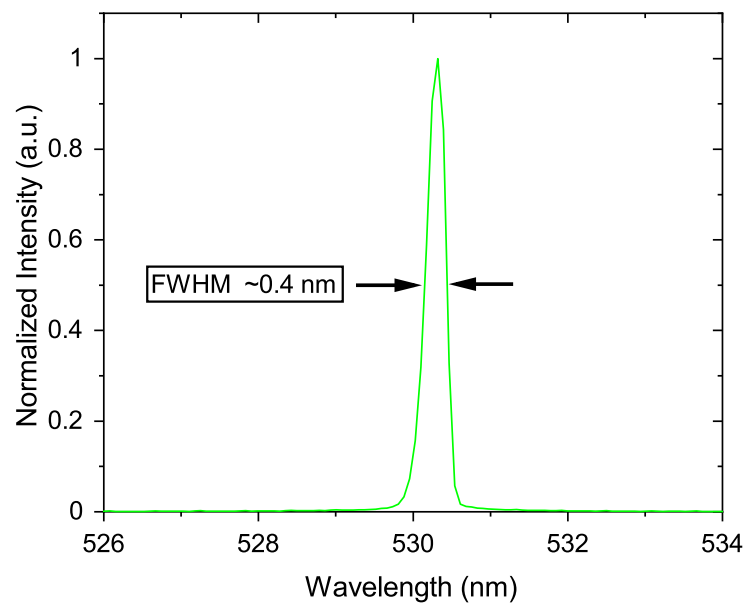
Figure 6.7: Optical spectrum of the second harmonic centered near 530 nm with a FWHM of approximately 0.4 nm.
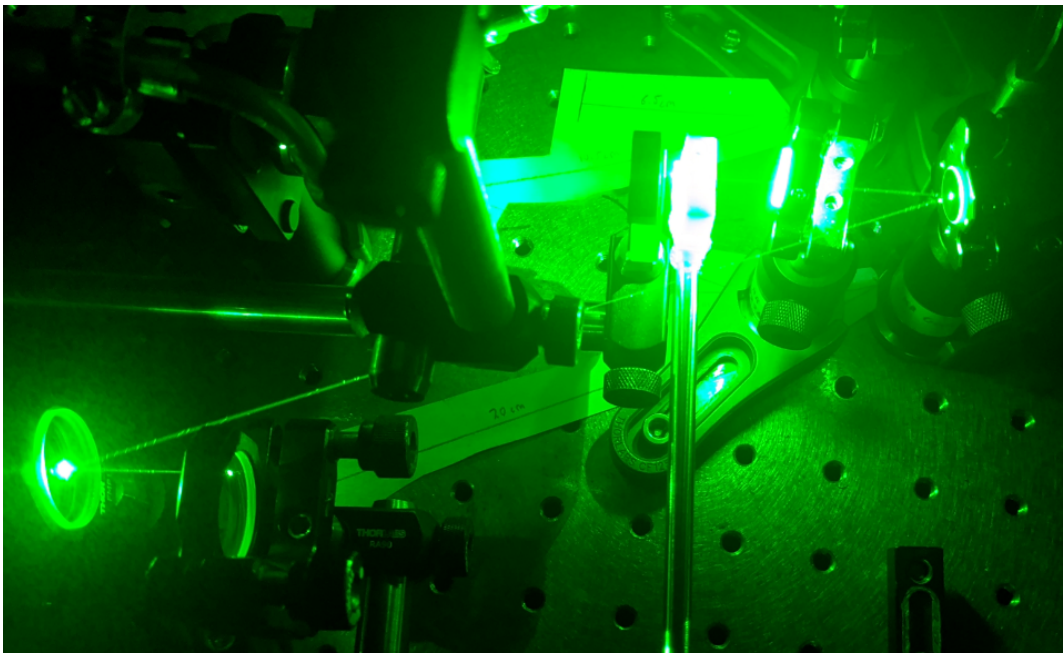
Figure 6.8: Picture of the high Q Z-cavity resonator demonstrating the power enhancement of the second harmonic.

Mirror M6 was adjusted slightly ensure that the repetition frequency of the Z-cavity matched the W-cavity for pulse overlapping of the fundamental and second harmonic at the LBO crystal. The BBO crystal was then inserted in front of mirror M6 for second harmonic generation of the circulating 530 nm pulse, which effectively frequency quadrupled the 1060 nm fundamental pulse. The overlapped W-cavity and Z-cavity can be observed in Fig. 6.9 where the red lines denote the fundamental cavity and the green lines denote the second harmonic cavity. There was no mirror available with an HR coating at both 532 nm and 266 nm, which resulted in the use of M6 which has an HR coating at 532 nm but <10% reflectivity at 266 nm. Therefore, we were only able to achieve single pass SHG to the deep UV spectral region with ejection of this pulse immediately out of the cavity through M6. For the second harmonic in a BBO crystal utilizing SHG to the UV spectral region, the GVM coefficient is approximately 600-650 fs/mm, which will result in broadening of the UV pulse duration by 2-3 ps. The optical spectrum of the UV pulse was centered near 265 nm, as observed in Fig. 6.10, which is the fourth harmonic of the fundamental 1060 nm pulse.
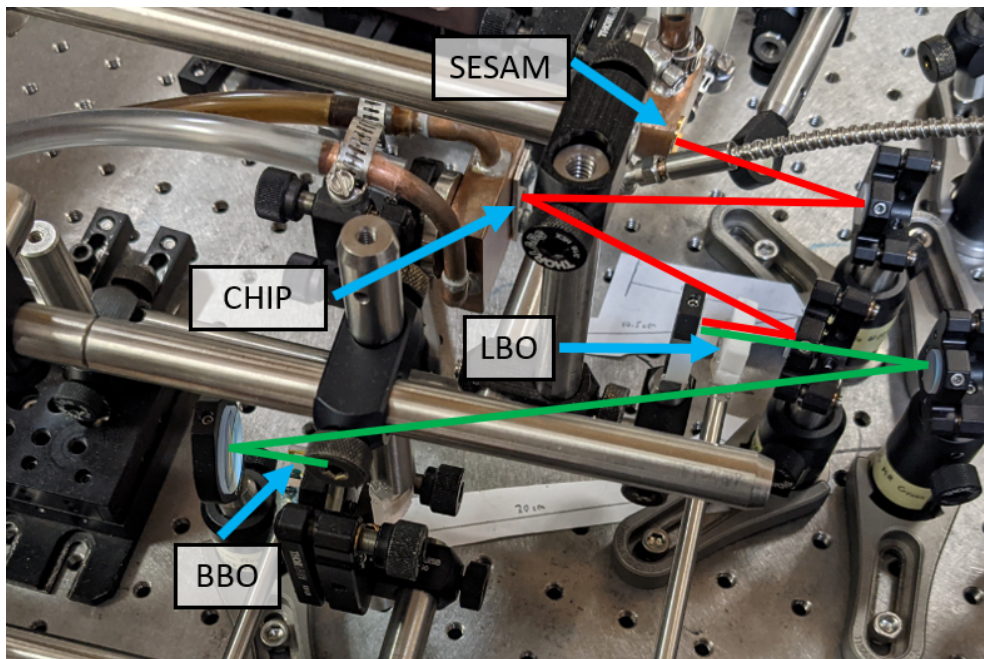
Figure 6.9: Picture of the overlapped fundamental W-cavity (red lines) and second harmonic Z-cavity (green lines).
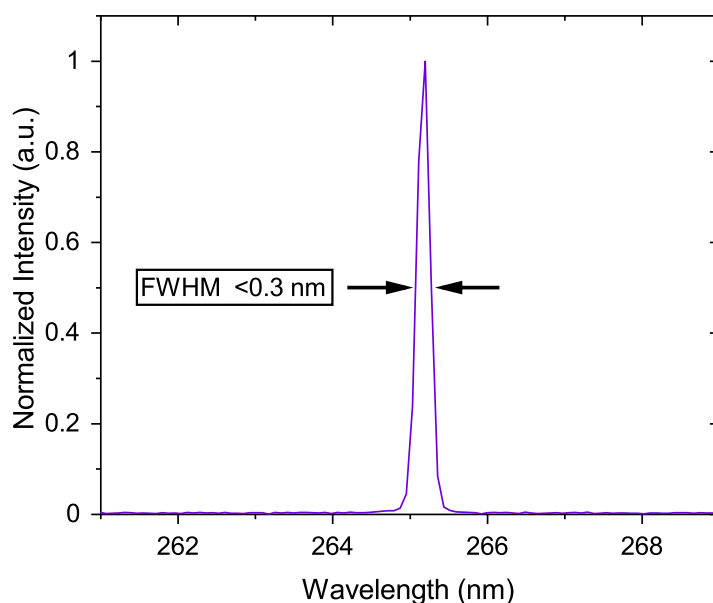
Figure 6.10: Optical spectrum of the fourth harmonic pulse centered near 265 nm with a FWHM of <0.3 nm.

The output power power of the UV was measured to be approximately 525 μW. When considering that the repetition rate of the UV pulse has to match the repetition rate of the second harmonic of 510 MHz, and a broadened pulse duration of 3-4 ps, the peak power of the UV pulse is calculated to be approximately 250-300 mW. To determine the amount of power enhancement achieved by use of the high Q Z-cavity resonator, mirror M6 was removed from the cavity and the UV output power was measured again. This output power was limited to ~50-60 μW, which demonstrates a factor of 10 power enhancement using the high Q resonator. The power stability of the UV pulse was also measured over a 30 minute duration and can be observed in Fig. 6.11. There was a power deviation of approximately $\pm 5\%$ over this time duration which demonstrates excellent stability considering that no active stabilization equipment was utilized. Finally, a picture of the UV laser beam can be observed in Fig. 6.12.
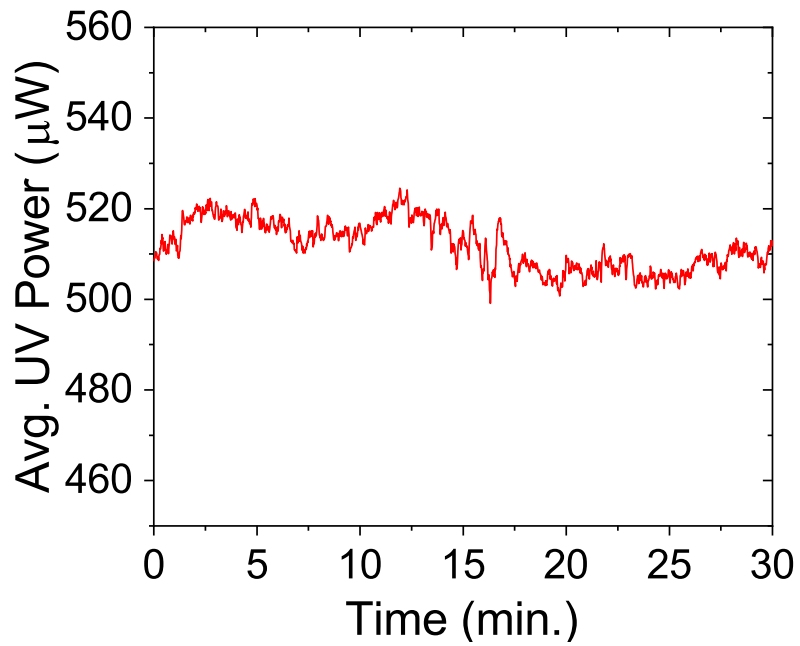
Figure 6.11: Power stability plot of the UV pulse over a 30 minute duration demonstrating a ±5% deviation. This was achieved without the use of any active stabilization equipment.
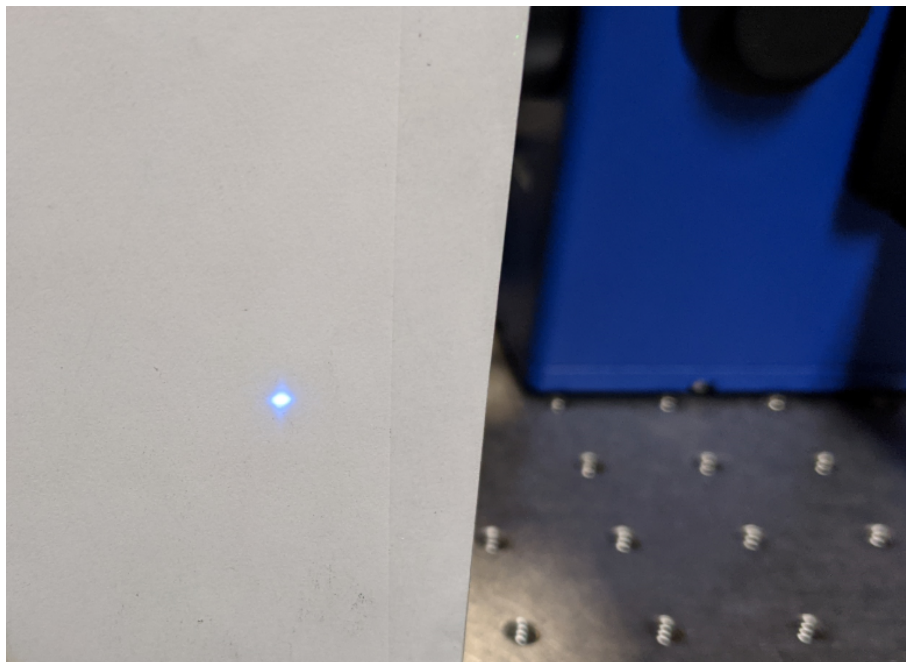
Figure 6.12: Picture of the generated UV laser beam external to the cavity.

This is the first demonstration of a passively mode locked VECSEL utilizing all-intracavity fourth harmonic generation of ultrashort deep UV pulses. Further work could result in substantial improvements to the UV output. The ideal beam diameter at the LBO crystal for highly efficient SHG should be closer to 60 μm, instead of the designed 110 μm. This could result in greater circulating power of second harmonic pulse in the Z-cavity resonator, which would in turn result in greater conversion to the fourth harmonic. Furthermore, the ideal beam size at the BBO crystal is approximately 30 μm. This results in a significant loss of conversion efficiency to the fourth harmonic. All of the mirrors used in this experiment were off-the-shelf. Customized mirrors could result in a cavity design that is able to achieve better mode sizes at the LBO and BBO crystals for increased conversion efficiency and greater UV output power. Another important consideration is that a reduction in the size of the beam at the BBO crystal that boosts conversion efficiency would allow for use of a shorter crystal length to achieve the same output power. This would reduce the pulse broadening effect of GVM. This could result in a trade-off between pulse duration and average output power.

Chapter 7

Ultrafast 1550 nm VECSEL

7.1 Brief History

Passively mode locked VECSELs emitting in the telecom C-band (1530-1565 nm) are of great interest as compact, low-cost laser sources that can provide multi-GHz repetition rates through cavity engineering. These VECSELs utilize quaternary semiconductors based on the InP material system to target the 1550 nm spectral region. Both continuous wave and mode locked 1550 nm VECSELs have seen their performance limited by poor heat dissipation and, until recently, were only capable of delivering tens to hundreds of milliwatts of average output power with temperatures typically near 0°C [25, 53, 95–97].

One of the primary challenges with VECSELs emitting in this spectral region is the size of the distributed Bragg reflector (DBR) mirror required for high reflectivity of the fundamental exceeding 99.8%. As described in Chapter 1, the DBR mirror is a series of $\lambda/4$-layer pairs that, with a specific number of repeats, can result in high reflectivity. However, the large 1550 nm wavelength results in thicker layers which is further compounded by the small index contrast that exists between InP and lattice-matched quaternary structures necessitating a greater number of pairs to achieve high reflectivity. Waste heat extraction through this thick DBR can be inefficient and has led to inclusion of additional heat management techniques, such as heat extraction out of the surface of the gain chip by use of a silicon carbide or diamond heat spreader attached through liquid capillary

bonding.

More recently, a high power 1550 nm CW VECSEL was demonstrated with watt-level output power at 11-15°C [98]. This was made possible by utilizing wafer fusion to bond a AlAs/GaAs DBR to the InAlGaAs/InP gain section which alleviates the constraint of lattice-matching the DBR to InP. A similar metallization and selective chemical wet-etching process as described in Chapter 1 was utilized to bond the chip to a diamond heat sink. However, the process of wafer fusion is complex and was still demonstrated to lead to catastrophic failure of the chip as a result of nonuniform fusion across the entire wafer structure.

For industry telecommunications applications, a 1550 nm VECSEL needs to be robust, compact, and inexpensive. A semiconductor wafer designed for emission at 1550 nm using InGaAsP/InP that avoided the use of strain compensation layers by ensuring that every layer was lattice-matched to the InP substrate. An additional small pump DBR section was included for reflection of any unabsorbed 1210 nm pump photons to prevent absorption in the fundamental DBR which would add additional waste heat to the chip. Finally, etch stop layers were incorporated to enable the use of the same fabrication method outlined in Chapter 1, although with different acids that are selective to InP-based materials. This allows for the utilization of the efficient heat extraction capability of solder-bonded diamond heat sinks while avoiding the additional complexity and expense of wafer fusion. This work was generously funded by the II-VI Foundation.

7.2 Semiconductor Chip Design

7.2.1 Active Region

The first part of the multi-quantum well (MQW) semiconductor structure that was designed was the active region that consists of the quantum wells (gain) and barriers. Both the wells and barriers were designed using $In_{1-x}Ga_xAs_yP_{1-y}$ and lattice-matched to InP. Solving for the energy levels within the quantum well

requires solving the Time Independent Schrödinger Equation (TISE) expressed as

$$\hat{H}\Psi(x) = \hat{E}\Psi(x) \qquad (7.1)$$

where $\hat{H}$ and $\hat{E}$ are the Hamiltonian and energy operators, respectively, and $\Psi(x)$ is the wavefunction. The TISE needs to be solved for both the energy levels in the conduction band well and valence band well. The depth of the potential well will help determine the position of the quantized energy levels and is defined by the band gap offsets ΔE_c and ΔE_v for the conduction and valence band, respectively [99]. These values are in part defined by ΔE_g, which represents the band gap energy difference between the quantum well and barrier. There is significant variation in the literature regarding the energy levels in $In_{1-x}Ga_xAs_yP_{1-y}$ lattice-matched to InP [100–102]. This led to using an energy level equation that is a linear interpolation of certain data sets given by

$$E_g(eV) = 0.74 + 0.61(1 - y) \qquad (7.2)$$

which is valid for room temperature operation [103]. The effective masses of the electron, heavy hole, and light hole, also need to be computed. While the effective mass of the electron in this material system is well defined, it is again not the same case for heavy and light hole effective masses. However, the approximate equations in literature for these parameters are

$$m_e = (0.08 - 0.039y)m_0 \qquad (7.3)$$

$$m_{lh} = (0.120 - 0.099y + 0.030y^2)m_0 \qquad (7.4)$$

$$m_{hh} = 0.46m_0 \qquad (7.5)$$

where m_0 is the free electron mass [99]. These equations focus primarily on the amount of arsenide within the quaternary compound and assumes lattice-matching

to InP. This requires that the amount of gallium to be adjusted based on the amount of arsenide to ensure the lattice matching, which results in

$$x \simeq \frac{0.1849y}{0.4184 - 0.013y} \simeq 0.47y \tag{7.6}$$

where y is the percentage of arsenide in the quaternary.

The energy of fundamental photon is now determined by adding the band gap of the quantum well, energy of the first energy level in the conduction band well, and energy level of the heavy hole in the valence band well. After determination of the material composition of the quantum well and barrier regions to achieve the desired fundamental lasing wavelength, the width of the barrier section is determined to place each quantum well at an antinode of the standing electric field within the microcavity to take advantage of resonant periodic gain [23]. Finally, the number of repeat sections of barrier/wells was determined to be 6 due to the absorption of the barrier region being approximately 5000-10,000 cm^{-1} for the pump wavelength of 1210 nm.

The energy band structure observed in Fig. 7.1 contains energy values calculated for an active region designed for fundamental emission at ~1520 nm. The gain has been detuned by 35 nm to account for thermal effects that will be described later. The barrier band gap is designed for absorption of the 1210 nm pump photons. The major drawback of using a simplified structure with InGaAsP used as both the quantum well and barrier material is that the depth of the quantum well is severely diminished. This can result in thermal excitation of electrons out of the well, which will reduce lasing efficiency and increase the thermal load from radiative recombination.
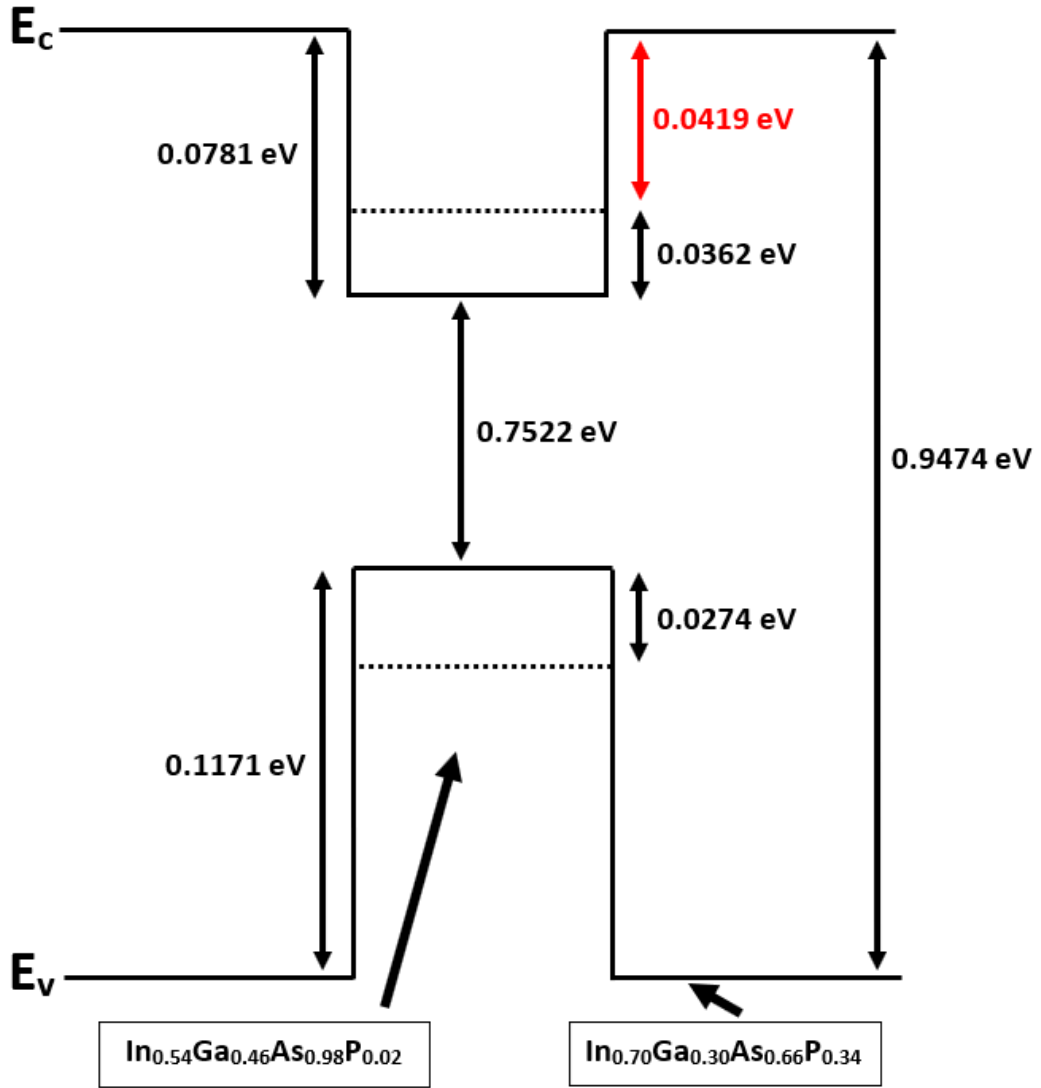
Figure 7.1: Energy band diagram for the active region designed for emission at ~1520 nm. The conduction band well depth of 0.0419 eV between the barrier and first energy level will lead to potential leakage of electrons out of the well.

7.2.2 DBR Mirror

The DBR mirror is designed using a transfer matrix method commonly used for multilayer film design. This approach uses a set of matrices that represent transfer through an interface separating materials i and j and propagation through layer i or j, as observed in Fig. 7.2. The matrices that transfer and propagation can be expressed as
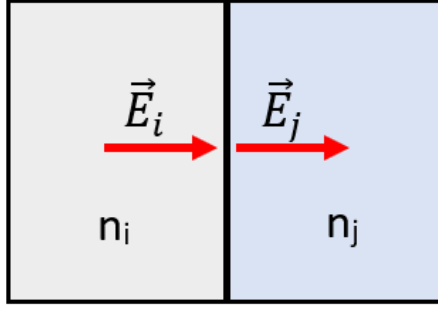
Figure 7.2: Basic schematic of electric field propagation through the two layers n_i and n_j that comprise the DBR structure.

The matrix for transfer through an interface can be expressed as [104]

$$T_{ij} = \frac{1}{t_{ij}} \begin{bmatrix} 1 & r_{ij} \\ r_{ij} & 1 \end{bmatrix} \tag{7.7}$$

where t_{ij} and r_{ij} are given by

$$t_{ij} = \frac{2n_i}{n_i + n_j} \tag{7.8}$$

and

$$r_{ij} = \frac{n_i - n_j}{n_i + n_j} \tag{7.9}$$

where we assume a propagation angle of zero. The matrix for propagation through a specific layer is expressed as

$$T_i = \begin{bmatrix} e^{-j\Phi_i} & 0 \\ 0 & e^{j\Phi_i} \end{bmatrix} \tag{7.10}$$

where Φ_i is given by

$$\Phi_i = \frac{2\pi n_i d_i}{\lambda_0} \tag{7.11}$$

where d_i is the thickness of layer i and λ_0 is the wavelength. A total system matrix T_{sys} is calculated that is the multiplication of each matrix in order,

$$T_{sys} = T_0 T_1 T_{12} T_2 T_{23} T_3 ... T_{N-1} T_{(N-1)N} = \begin{bmatrix} T_{11}^{0N} & T_{12}^{0N} \\ T_{21}^{0N} & T_{22}^{0N} \end{bmatrix} \tag{7.12}$$

From this system matrix we can determine the reflectivity R at a given wavelength λ_0 from

$$r = \frac{T_{21}^{0N}}{T_{11}^{0N}} \tag{7.13}$$

where

$$R = |r|^2. \tag{7.14}$$

As discussed in Chapter 1, a stack of $\lambda/4$ layer pairs should ideally result in high reflectivity >99.8% centered at the fundamental lasing wavelength. The stopband, or wavelength window where high reflectivity is achieved, is a strong function of the index contrast between the two layers. For the wafer designed for operation at 1550 nm, the DBR was designed to have alternating layers of InGaAsP/InP with the InGaAsP lattice-matched to InP. The energy level diagram and material compositions can be observed in Fig. 7.3.

The DBR design requires a stack of 48 layer pairs for high reflectivity and a large stopband, for a total thickness of approximately 11 μm. The reflectivity can be observed in Fig. 7.4.
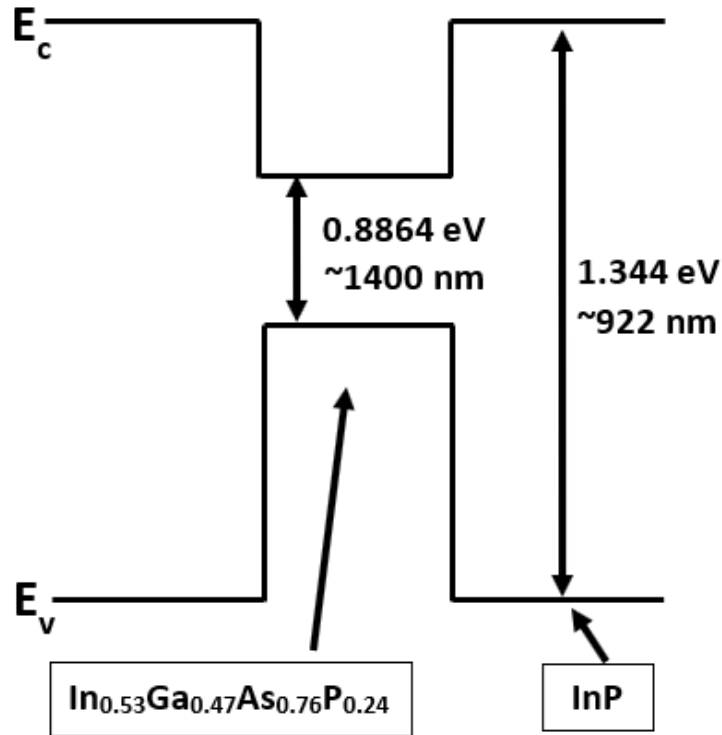
Figure 7.3: Energy level diagram of the DBR section designed for 1550 nm.
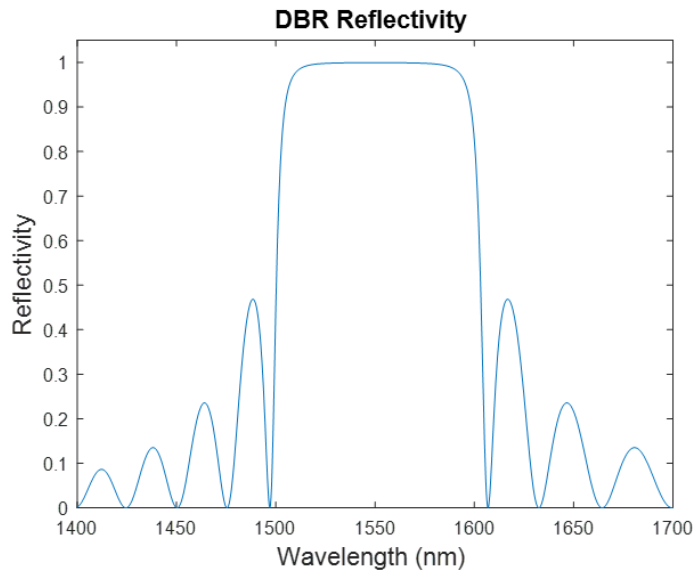
Figure 7.4: DBR reflectivity plot designed for 1550 nm. Note that the stopband is approximately 80 nm wide.

A similar method was used to design another smaller DBR for approximately 10% reflection of the 1210 nm pump photons, observed in Fig. 7.5.
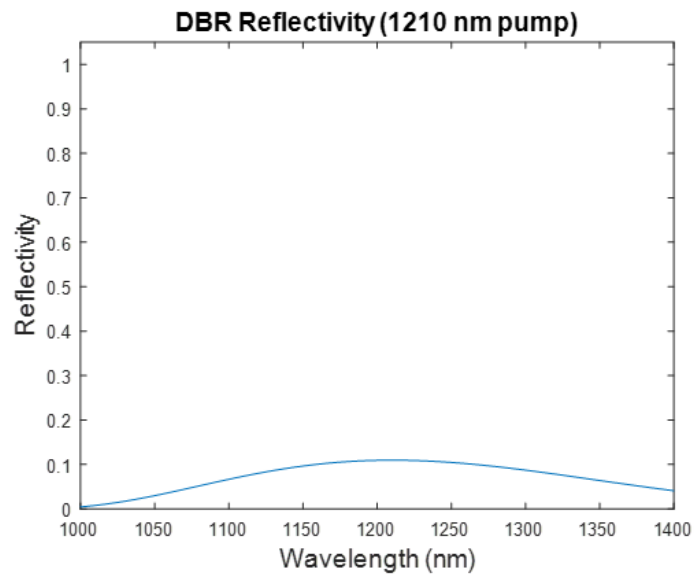
Figure 7.5: DBR reflectivity plot designed for 1210 nm. The maximum reflectivity is approxiomately 10%.

7.2.3 Full Chip Reflectivity and Detuning

As was mentioned previously, the active region was designed for a lasing wavelength of 1520 nm. The gain was detuned by 35 nm to account for red shifting

of the gain peak of 0.3-0.54 nm/K that is expected under thermal load during normal operation [25, 51, 97]. Furthermore, the subcavity was set at 1535 nm to account for a similar, but weaker, red shift of $\sim$0.1 nm/K of the subcavity resonance. At room temperature, it is expected that the gain profile will overlap the subcavity resonance near 1550 nm during lasing operation. The reflectivity of the full structure, which includes the active region and both DBR sections, was modeled and can be observed in Fig. 7.6. The zoomed-in reflectivity curve in Fig. 7.7 demonstrates that the subcavity resonance was correctly set to 1535 nm by the dip in the stopband at this wavelength.
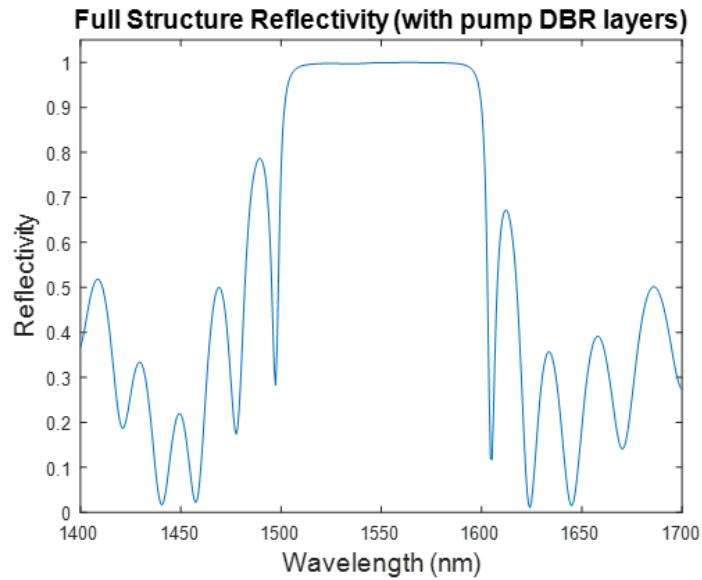
Figure 7.6: Reflectivity plot of the full MQW chip structure.
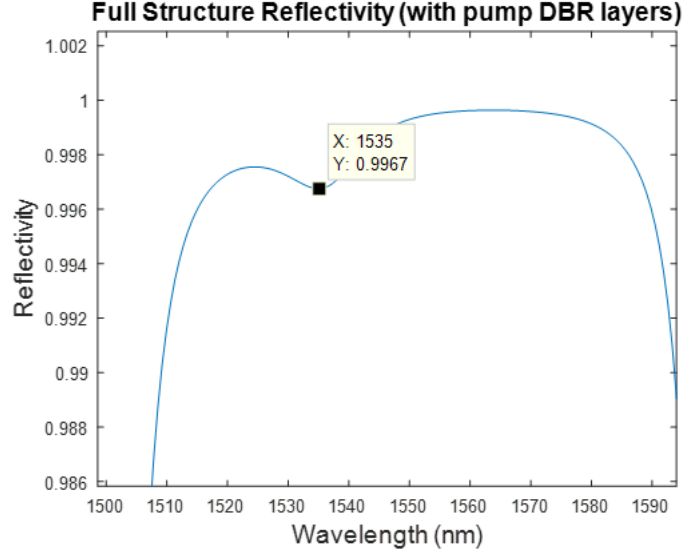
Figure 7.7: Zoomed in view of the reflectivity plot of the full MQW chip structure. The dip at 1535 nm demonstrates that the subcavity was properly set at that wavelength to account for a red-shift under thermal load.

7.3 Z-Cavity Resonator

With the 1550 nm wafer design submitted to industry for eventual growth, attention was paid to designing a resonator cavity that is capable of passive mode locking with this chip. A Z-cavity resonator was modeled using the ABCD matrix code, as observed in Fig. 7.8. Mirror M1 has a 20 cm radius of curvature (RoC), with a 99.35% high-reflectivity (HR) coating from 1400-1700 nm. Mirror M2 has a 5 cm RoC with the same coating as M1. The long arm distance L1+L2 was 13 cm while the short arm distance L3 was 2.5 cm. The SESAM used for this design had a modulation depth ΔR of 2%, nonsaturable loss of 1%, saturation fluence of 180 μJ/cm^2, and a recovery time of 4 ps. If the gain chip is placed 8 cm from M1, it will result in a mode area ratio of $\sim$17, which is in the ideal range for stable mode locking. Finally, pulse stability was also modeled and is observed in Fig. 7.9.
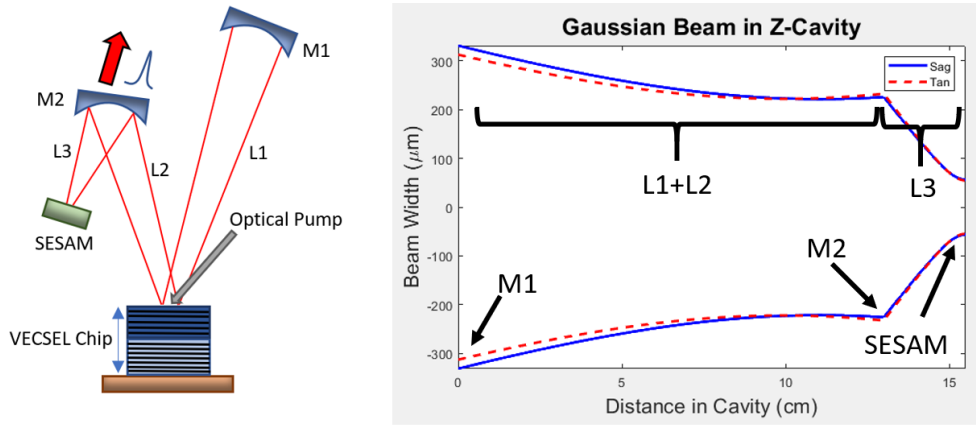
Figure 7.8: Gaussian beam modeled within the Z-cavity designed for the 1550 nm VECSEL.
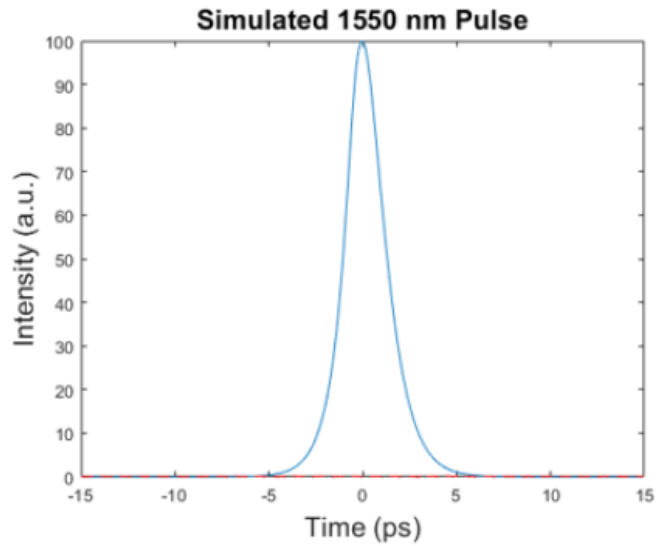
Figure 7.9: Pulse simulation demonstrating a stable pulse for the 1550 nm VEC-SEL.

While it is expected that the new 1550 nm VECSEL chip will be experimentally demonstrated under continuous wave operation, it is still questionable if the chip as designed will result in stable passive mode locking. This is the result of several parameters being approximated within the simulation model, such as the gain bandwidth and saturation fluence. Each of these parameters will have a significant impact on pulse formation. However, the knowledge gained from the first wafer growth will be utilized to adjust parameters and equations within the wafer design model for an optimized second growth that will be able to achieve passive mode locking at 1550 nm in a compact, cost-effective design.

Chapter 8

Generation of Higher Order Hermite-Gaussian and Laguerre-Gaussian Beams in an Ultrafast VECSEL

8.1 Brief History

An interesting area of research and development involving VECSELs is the generation of higher order Hermite-Gaussian (HG) beams for conversion into Laguerre-Gaussian (LG) beams. In recent years, significant effort has been put toward the research and development of encoding information in the orbital angular momentum (OAM) modes of LG laser beams, which have been demonstrated to be capable of delivering optical information through free space [105]. Encoding free space optical (FSO) communications in the OAM of LG beams provides additional physical layer security against eavesdropping which is highly lucrative for defense applications [106, 107]. Individual OAM modes are also orthogonal to any other OAM mode, which can lead to a significant increase in short haul fiber optic channel capacity through mode division multiplexing (MDM) without degradation from crosstalk [108].

Our research group has recently published extensive work detailing how direct

access to the laser cavity in a continuous wave VECSEL enables the creation of any arbitrary HG mode that can be converted into a corresponding LG mode [20, 109, 110]. The creation of specific HG modes can be done by inserting a "mode control element" into the cavity with an obstruction over the nodes of the desired mode, or the use of one (or more) pump lasers displaced from the center axis of the resonator on the chip. This work was expanded upon by using a Z-cavity resonator with a SESAM to generate a pulsed HG beam for mode conversion to an LG beam.

A mode converter placed in the beam path external to the cavity can then convert the HG modes into corresponding LG modes, a schematic of which can be observed in Fig. 8.1. Any higher order HG or LG mode distribution can be described by a superposition of other HG or LG modes with proper phase factors [111]. In the case of Fig. 8.1, the initial HG_{10} mode rotated at 45° can be described as a superposition of an in-phase HG_{10} and HG_{01} mode. The use of a cylindrical lens pair induces different Gouy phase shifts in the tangential and sagittal directions between the pair of lenses. If this phase difference is $\pi/2$ between the exiting HG_{10} and HG_{01} modes, the superposition is now an LG_{10} mode. This method allows for transforming any HG mode into a corresponding LG mode.
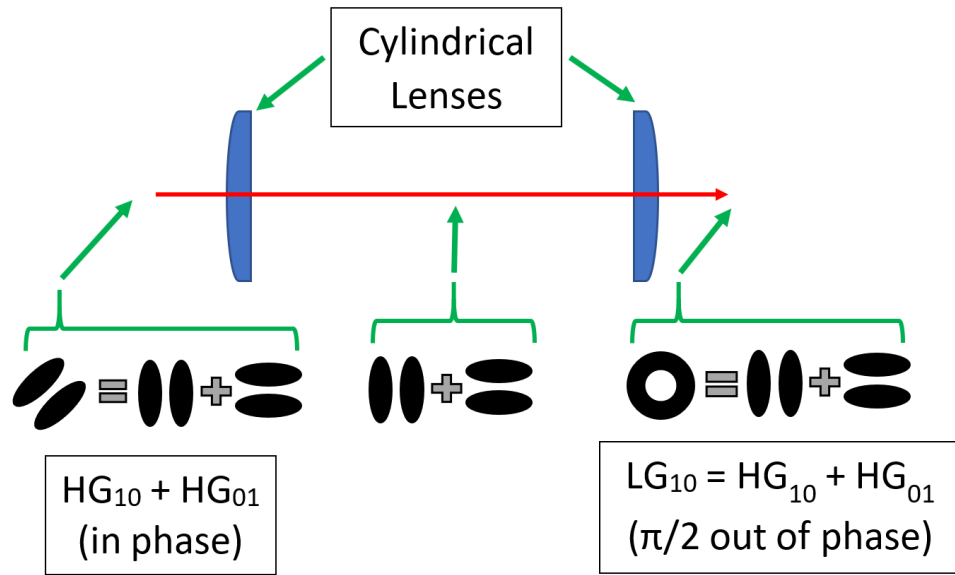
Figure 8.1: Schematic of an astigmatic mode converter with two cylindrical lenses of equal focal length. The tangential and sagittal directions will experience different phase shifts due to the cylindrical lenses only adding optical power in one plane. In the above example, if the exiting HG modes pick up a phase difference of $\pi/2$ after transversing the mode converter, the result is an LG mode.

8.2 Initial Experimental Results

A typical Z-cavity was constructed to test the potential of mode locking high order HG modes, with the addition of a second pump laser for the chip, which can be observed in Fig. 8.2. The SESAM used had a recovery time of 25 ps, a modulation depth ΔR of 6%, and nonsaturable loss of 2%. The fold mirror M2 had a 7.5 cm RoC with a 99% reflectivity coating at 1070 nm. The end mirror M1 had a 30 cm RoC with an HR coating at 1070 nm. The total cavity length was $\sim$28 cm, with L1+L2 being 25 cm long and L3 being $\sim$3 cm long. The cavity was designed for a spot diameter of $\sim$120 μm on the SESAM and $\sim$440 μm on the chip, which results in a mode area ratio of 14. The 1070 nm chip was pumped with two 808 nm fiber-coupled diode lasers with focused spot sizes of $\sim$500 μm. The chip and SESAM were maintained at a temperature of 10°C.
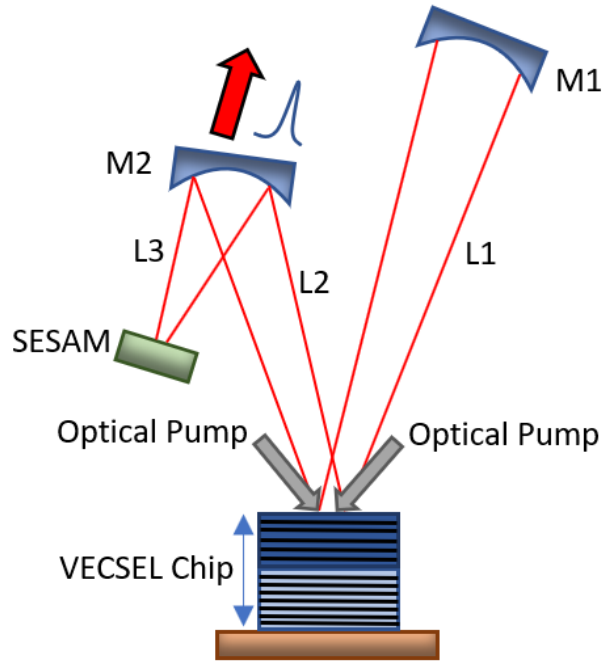
Figure 8.2: Z-cavity VECSEL layout with two optical pump lasers for generation of higher order HG modes.

The two pumps were focused and overlapped on the chip and then displaced horizontally in different directions to induce a higher order mode by changing the gain preference and thus mode profile for the cavity [20]. It was only possible to induce what appears to be a low quality asymmetric HG_{10} mode, as observed in the free space CCD image in Fig. 8.3. The asymmetry is most likely a result of the fold mirror M2 introducing astigmatism into the cavity. An astigmatic mode converter was constructed to convert this "HG_{10}" mode into an "LG_{10}" mode, with the result observed in Fig. 8.4.
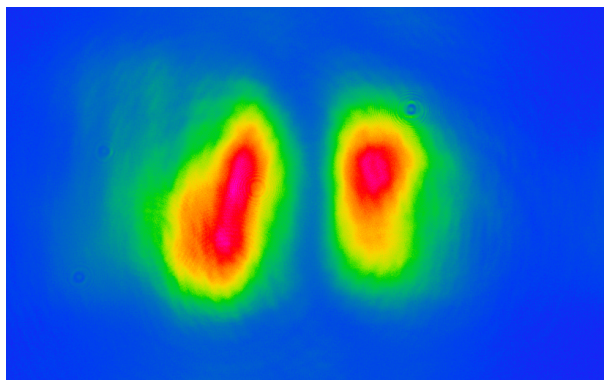
Figure 8.3: Free space image of the potential HG_{10} mode using a CCD camera.
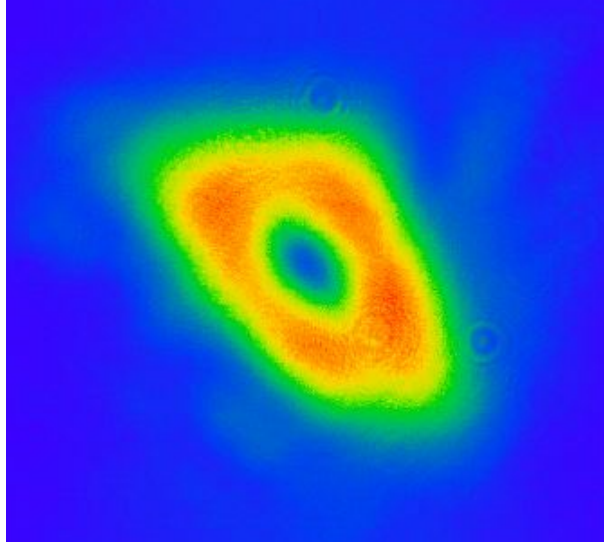
Figure 8.4: Free space image of the potential LG_{10} mode using a CCD camera.

It is not known exactly if stable mode locking had been achieved during operation with the "HG" mode. The pulse was measured, but it was rather weak in comparison to other builds. The measured pulse shape was normalized and fit with a $sech^2$ function which demonstrates a FWHM pulse duration of 1.6 ps, as observed in Fig. 8.5. The RF spectrum was also measured and does indicate a stable mode lock, as indicated by equally-spaced peaks with a separation of 525 MHz, which closely matches the calculated repetition frequency of 535 MHz. The RF spectrum plot, observed in Fig. 8.6, is also absent of any secondary peaks which would indicate instability. Finally, the optical spectrum was measured and is centered near 1068 nm, with a FWHM bandwidth of approximately 1 nm, as seen in Fig. 8.7.

Autocorrelation Signal of 1.6 ps Pulse (HG10)
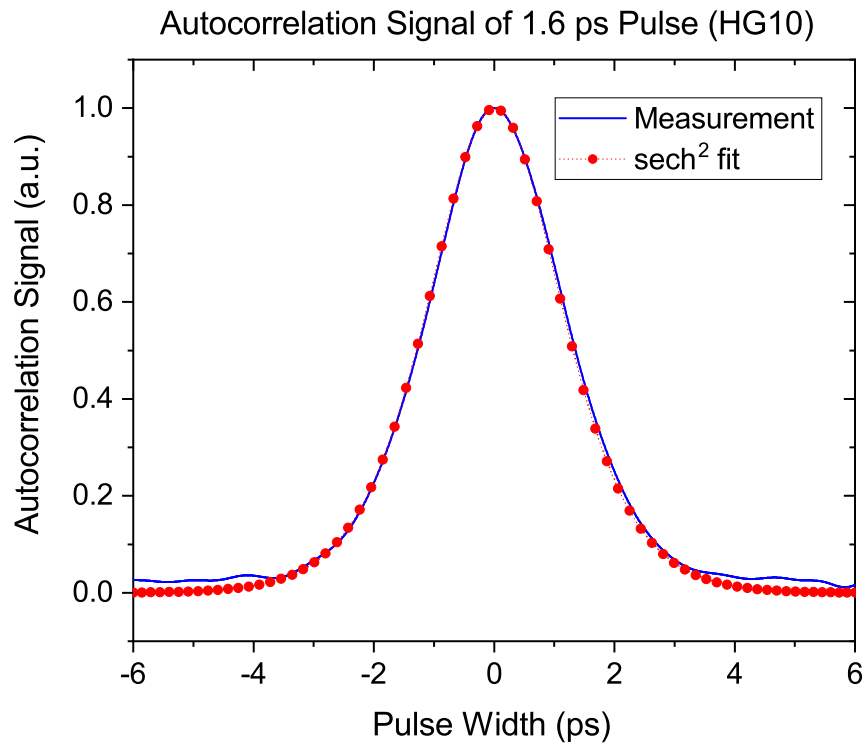
Figure 8.5: Autocorrelation measurement of the fundamental "HG" beam.

RF Frequency of HG10 Pulse
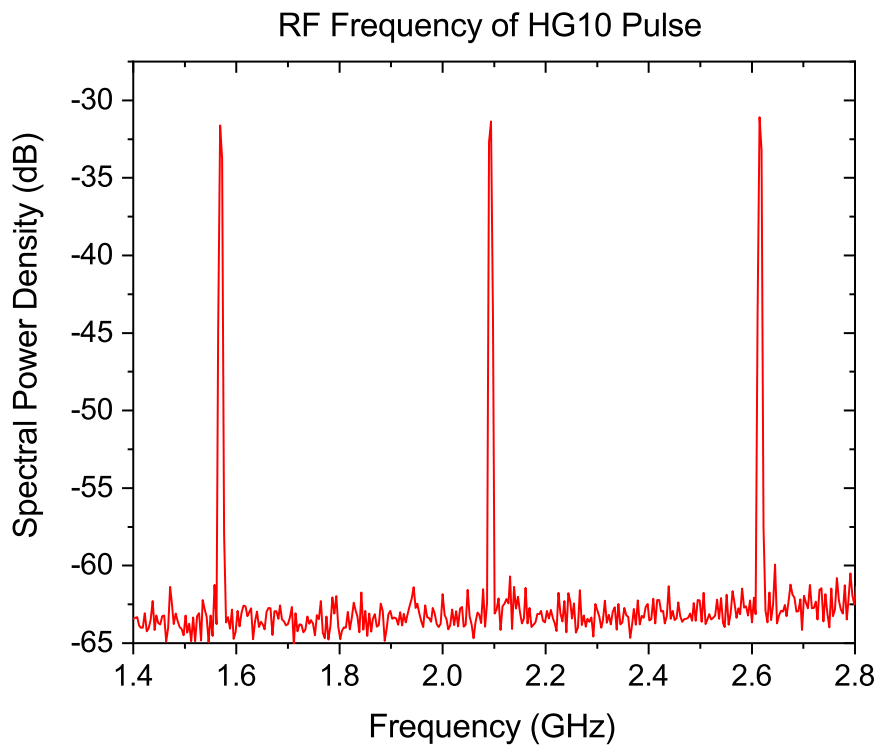
Figure 8.6: RF spectrum of the circulating "HG" beam demonstrating a repetition frequency of 525 MHz.
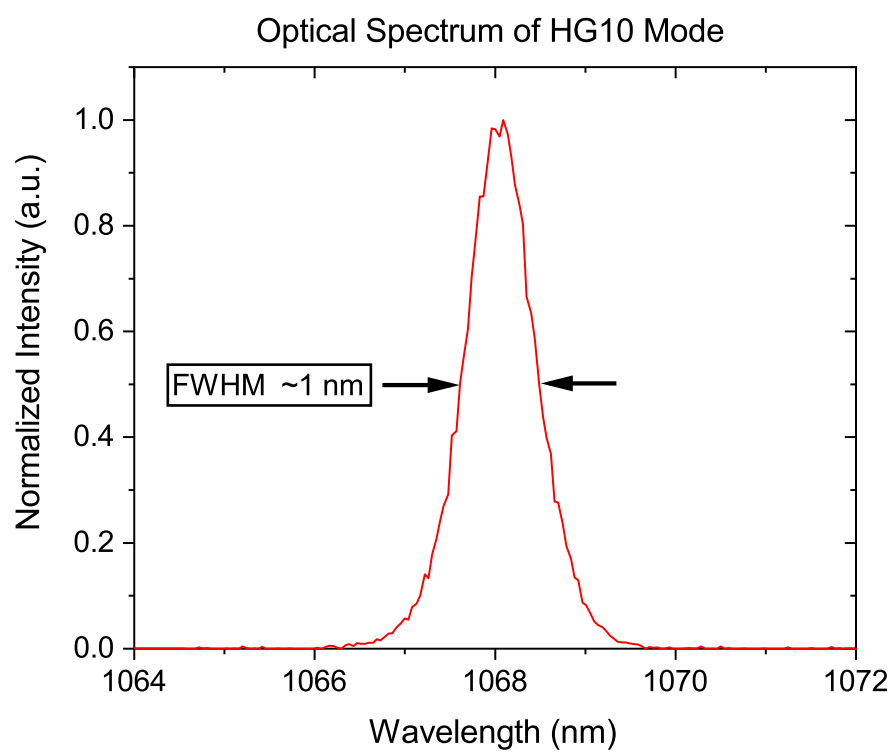
Figure 8.7: Optical spectrum of the "HG" beam centered near 1068 nm with a bandwidth of approximately 1 nm.

8.3 Future Work

There are two remaining questions that are unresolved with the generation of this potential HG_{10} mode: is it a pure HG_{10} mode and is the cavity mode locked during operation? All existing work and models regarding passively mode locked VECSELs assumes a HG_{00} mode. The saturation model of a SESAM also assumes a uniform super Gaussian profile where the same saturation fluence exists across the region of the SESAM spanned by the laser beam. This is not necessarily the case when the circulating beam in the resonator is a higher order mode with asymmetric intensity profiles between the different lobes of the mode. It is possible to imagine a scenario where, in the case of a hypothetical HG_{30} mode, the outer two lobes might saturate differently than the inner two lobes. This might induce a filtering effect by the SESAM, where the portions of the beam that saturate sooner see a gain preference and the rest are simply absorbed without inducing a mode lock. This provides an exciting opportunity to continue to explore the potential for passive mode locking in a VECSEL with higher order modes and discovery of the criteria that governs this process.

Chapter 9

Conclusion

Passively mode locked VECSELs have been developed extensively over the past two decades with excellent results regarding picosecond-femtosecond pulse duration, multi-GHz repetition frequencies, multi-watt average output powers, and kW-level peak pulse powers at the fundamental lasing wavelength. This has been accomplished with novel gain chip and SESAM designs, specialized coatings to eliminate dispersion within the cavity, temperature control of the chip and SESAM, etc. Intracavity nonlinear frequency conversion was also shown to be capable of generating ultrashort pulses at the second harmonic, but with extremely low output power.

An optimized passively mode locked VECSEL in a W-cavity configuration utilizing intracavity second harmonic generation was demonstrated to be capable of generating $\sim$760 fs pulses with 230 mW of average output power at a repetition frequency of $\sim$465 MHz, resulting in a record-setting peak pulse power of 490 W. The key to this breakthrough was separating the nonlinear optical crystal into a separate cavity arm from the SESAM, and optimizing the spot sizes on the SESAM and gain chip for stable mode locking simultaneously with a more ideal spot size on the LBO crystal for efficient second harmonic generation.

The high output power of the "green" pulses generated in an optimized W-cavity was fully enclosed in its own partially-overlapped high Q Z-cavity resonator for power enhancement. With a BBO crystal inserted into the Z-cavity, it was possible to generate ultrashort UV pulses at $\sim$265 nm with a duration of $\sim$3-4 ps, 525 μW average output power, and a repetition rate of 510 MHz, resulting in

111

a peak pulse power of 250-300 mW at the fourth harmonic. This was achieved without any active stabilization and only off-the-shelf components, which greatly reduces the size and cost of the laser package. Customization of the cavity components, such as mirror curvatures and coatings, could push the UV average output power to tens of milliwatts or more, which would result in tens of watts of UV peak pulse power. This opens the door to a new type of ultrafast UV laser source that could be incredibly useful in medical, biological, or industrial applications and has the potential to be tailored to the needs of the end user.

The telecommunications industry has need for ultra-compact, low-cost, efficient laser sources operating in the C-band. A multi-quantum well semiconductor wafer structure was proposed for use in a passively mode locked VECSEL, along with an initial Z-cavity configuration. Future work could see this ultrafast telecom VECSEL scaled down to achieve multi-GHz operation, which would be ideal for information encoding.

Exploration of the potential of generating higher order Hermite-Gaussian modes within a passively mode locked VECSEL is of great interest because it has the capability to bridge different VECSEL technologies together into a single system. The mode locked "HG" mode results presented at ∼1070 nm could be combined with the wafer designed for emission at 1550 nm to provide an ultrafast telecom laser source capable of encoding information in the OAM states for data multiplexing. The flexible length of the external cavity could be minimized to boost the repetition frequency to >10 GHz operation, which would result in high-speed information encoding with picosecond-femtosecond pulses.

The future for the research and development of VECSELs is promising with new avenues being explored as the technology continues to mature. The work presented in this dissertation has demonstrated that the flexibility of the VECSEL will continue to push the boundaries and limitations of conventional laser technology and provide novel solutions for academic and industrial applications.

References

[1] F. Koyama. Recent advances of VCSEL photonics. *Journal of Lightwave Technology*, 24(12):4502–4513, 2006.

[2] M. Kreisler, H. Al Haj, and B. d'Hoedt. Clinical efficacy of semiconductor laser application as an adjunct to conventional scaling and root planing. *Lasers in Surgery and Medicine*, 37:350–355, 2005.

[3] M. Yakshin, C. Hessenius, C. Prasad, and M. Fallahi. A compact, efficient deep UV optically pumped VECSEL. In *Conference on Lasers and Electro-Optics*, page SM3M.4. Optical Society of America, 2017.

[4] J.E. Hastie, S. Calvez, M.D. Dawson, T. Leinonen, A. Laakso, J. Lyytikäinen, and M. Pessa. High power CW VECSEL with linearly polarized TEM_{00} output beam. *Optics Express*, 13(1):77–81, 2005.

[5] R.H. Abram, K.S. Gardner, E. Riis, and A.I. Ferguson. Narrow linewidth operation of a tunable optically pumped semiconductor laser. *Optics Express*, 12(22):5434–5439, 2004.

[6] M. Razeghi. High-performance InP-based mid-IR quantum cascade lasers. *IEEE Journal of Selected Topics in Quantum Electronics*, 15(3):941–951, 2009.

[7] R. Köhler, A. Tredicucci, F. Beltram, H.E. Beere, E.H. Linfield, A.G. Davies, D.A. Ritchie, R.C. Lotti, and F. Rossi. Terahertz semiconductor-heterostructure laser. *Nature*, 417:156–159, 2002.

[8] O.G. Okhotnikov. *Semiconductor Disk Lasers*. Wiley-VCH, Weinheim, 2010.

[9] P.V. Mena, J.J. Morikuna, S.-M. Kang, A.V. Harton, and K.W. Wyatt. A simple rate-equation-based thermal VCSEL model. *Journal of Lightwave Technology*, 17(5):865–872, 1999.

[10] M.-C. Amann and W. Hofmann. InP-based long-wavelength VCSELs and VCSEL arrays. *IEEE Journal of Selected Topics in Quantum Electronics*, 15(3):861–868, 2009.

[11] Holger Moench, Ralf Conrads, Carsten Deppe, Guenther Derra, Stephan Gronenborn, Xi Gu, Gero Heusler, Johanna Kolb, Michael Miller, Pavel Pekarski, Jens Pollmann-Retsch, Armand Pruijmboom, and Ulrich Weichmann. High-power VCSEL systems and applications. In *High-Power Diode Laser Technology and Applications XIII*, volume 9348, pages 267–276. International Society for Optics and Photonics, SPIE, 2015.

[12] M. Kuznetsov, F. Hakimi, R. Sprague, and A. Mooradian. High-power ($>$0.5 W cw) diode-pumped vertical-external-cavity surface-emitting semiconductor lasers with TEM_{00} beams. *IEEE Photonics Technology Letters*, 9(8): 1063–1065, 1997.

[13] W.J. Alford, T.D. Raymond, and A.A. Allerman. High power and good beam quality at 980 nm from a vertical external-cavity surface-emitting laser. *Journal of the Optical Society of America B*, 19(4):663–666, 2002.

[14] L. Fan, M. Fallahi, J.T. Murray, R. Bedford, Y. Kaneda, A.R. Zakharian, J. Hader, J.V. Moloney, W. Stolz, and S.W. Koch. Tunable high-power high-brightness linearly polarized vertical-external-cavity surface-emitting lasers. *Applied Physics Letters*, 88, 2006.

[15] A. Rahimi-Iman. Recent advances in VECSELs. *Journal of Optics*, 18: 093003, 2016.

[16] M. Guina. Optically pumped VECSELs: review of technology and progress. *Journal of Physics D: Applied Physics*, 50:383001, 2017.

[17] J.E. Hastie, L.G. Morton, A.J. Kemp, M.D. Dawson, A.B. Krysa, and J.S. Roberts. Tunable ultraviolet output from an intracavity frequency-doubled red vertical-external-cavity surface-emitting laser. *Applied Physics Letters*, 89:061114, 2006.

[18] M. Lukowski, C. Hessenius, and M. Fallahi. Widely tunable high-power two-color VECSELs for new wavelength generation. *IEEE Journal of Selected Topics in Quantum Electronics*, 21(1):1700208, 2015.

[19] M. Lukowski, C. Hessenius, R. Bedford, and M. Fallahi. Tunable type II intracavity difference frequency generation at 5.4 μm in a two chip vertical external cavity surface emitting laser. *Optics Letters*, 40(17):4174–4177, 2015.

[20] M.L. Lukowski, J.T. Meyer, C. Hessenius, E.M. Wright, and M. Fallahi. High-power higher order Hermite-Gaussian and Laguerre-Gaussian beams from vertical external cavity surface emitting lasers. *IEEE Journal of Selected Topics in Quantum Electronics*, 25(6):1500406, 2019.

[21] A. Aschwanden, D. Lorsenser, H.J. Unold, R. Paschota, E. Gini, and U. Keller. 2.1-W picosecond passively mode-locked external-cavity semiconductor laser. *Optics Letters*, 30(3):272–274, 2005.

[22] Y. Arakawa and H. Sakaki. Multidimensional quantum well laser and temperature dependence of its threshold current. *Applied Physics Letters*, 40 (11):939–941, 1982.

[23] M.Y.A. Raja, S.R.J. Brueck, M. Osiński, C.F. Schaus, J.G. McInerney, T.M. Brennan, and B.E. Hammons. Resonant periodic gain surface-emitting semiconductor lasers. *IEEE Journal of Quantum Electronics*, 25(6):1500–1512, 1989.

[24] L. Fan, J. Hader, M. Schillgalies, M. Fallahi, A.R. Zakharian, J.V. Moloney, R. Bedford, J.T. Murray, S.W. Koch, and W. Stolz. High-power opti-

cally pumped VECSEL using a double-well resonant periodic gain structure. *IEEE Photonics Technology Letters*, 17(9):1764–1766, 2005.

[25] H. Lindberg, M. Strasner, J. Bengtsson, and A. Larsson. High-power optically pumped 1550-nm VECSEL with a bonded silcon head spreader. *IEEE Photonics Technology Letters*, 16(5):1233–1235, 2004.

[26] M. Kuznetsov, F. Hakimi, R. Sprague, and A. Mooradian. Design and characteristics of high-power ($>$0.5-W cw) diode-pumped vertical-external-cavity surface-emitting semiconductor lasers with circular TEM_{00} beams. *IEEE Journal of Selected Topics in Quantum Electronics*, 5(3):561–573, 1999.

[27] Y. Qi, W. Li, S. Liu, and X. Ma. Comprehensive design and simulation of a composite reflector for mode control and thermal management of a high-power VECSEL. *Journal of the Optical Society of America B*, 37(11): 3487–3495, 2020.

[28] A.J. Kemp, A.J. Maclean, J.E. Hastie, S.A. Smith, J.-M. Hopkins, S. Calvez, G.J. Valentine, M.D. Dawson, and D. Burns. Thermal lensing, thermal management and transverse mode control in microchip VECSELs. *Applied Physics B*, 83:189–194, 2006.

[29] P. Zhao, B. Xu, R. van Leeuwen, T. Chen, L. Watkins, D. Zhou, P. Cao, G. Xu, Q. Wang, and C. Ghosh. Compact 4.7 W 18.3% wall-plug efficiency green laser based on an electrically pumped VECSEL using intracavity frequency doubling. *Optics Letters*, 39(16):4766–4768, 2014.

[30] A. Härkönen, A. Bachmann, S. Arafin, K. Haring, J. Viheriälä, M. Guina, and M.-C. Amann. 2.34-μm electrically pumped VECSEL with buried tunnel junction. In *Semiconductor Lasers and Laser Dynamics IV*, volume 7720, pages 255–261. International Society for Optics and Photonics, SPIE, 2010.

[31] R. Kreuter, B. Witzigmann, D.J.H.C. Maas, Y. Barbarin, T. Südmeyer,

and U. Keller. On the design of electrically pumped vertical-external-cavity surface-emitting lasers. *Applied Physics B*, 91:257–264, 2008.

[32] P.W. Milonni and J.H. Eberly. *Laser Physics*. John Wiley and Sons, Inc., Hoboken, 2010.

[33] E.A. Wachter, M.G. Petersen, , and H.C. Dees. Photodynamic therapy with ultrafast lasers. In *Commercial and Biomedical Applications of Ultrafast Lasers*, volume 3616, pages 66–74. International Society for Optics and Photonics, SPIE, 1999.

[34] F.H. Loesel, R.M. Kurtz, C. Horvath, S. Sayegh, G. Mourou, J.F. Bille, and T. Juhasz. Ultra-precise medical applications with ultrafast lasers: corneal surgery with femtosecond lasers. In *Medical Applications of Lasers in Dermatology, Cardiology, Ophthalmology, and Dentistry II*, volume 3564, pages 86–93. International Society for Optics and Photonics, SPIE, 1999.

[35] E.G. Gamaly, A.V. Rode, and B. Luther-Davies. Ultrafast ablation with high-pulse-rate lasers. part I: Theoretical considerations. *Journal of Applied Physics*, 85(8):4213–4221, 1999.

[36] E.G. Gamaly, A.V. Rode, and B. Luther-Davies. Ultrafast ablation with high-pulse-rate lasers. part II: Experiments on laser deposition of amorphous carbon films. *Journal of Applied Physics*, 85(8):4222–4230, 1999.

[37] X. Liu, D. Du, and G. Mourou. Laser ablation and micromachining with ultrashort laser pulses. *IEEE Journal of Quantum Electronics*, 33(10):1716, 1997.

[38] S. Backus, C.G. Durfee, M.M. Murnane, and H.C. Kapteyn. High power ultrafast lasers. *Review of Scientific Instruments*, 69(3):1207–1223, 1998.

[39] C. Hönniger, R. Paschotta, F. Morier-Genoud, M. Moser, and U. Keller. Q-switching stability limits of continuous-wave passive mode locking. *Journal of the Optical Society of American B*, 16(1):46–56, 1999.

[40] L. Krainer, R. Paschotta, G.J. Spühler, M. Moser, and U. Keller. 29 GHz modelocked miniature Nd:YVO4 laser. *Electronic Letters*, 35(14), 1999.

[41] S. Hoogland, S. Dhanjal, A.C. Tropper, J.S. Roberts, R. Häring, R. Paschotta, F. Morier-Genoud, and U. Keller. Passively mode-locked diode-pumped surface-emitting semiconductor laser. *IEEE Photonics Technology Letters*, 12(9):1135–1137, 2000.

[42] U. Keller and A.C. Tropper. Passively modelocked surface-emitting semiconductor lasers. *Physics Reports*, 429(2), 2006.

[43] K.G. Wilcox, A.C. Tropper, H.E. Beere, D.A. Ritchie, B. Kunert, B. Heinen, and W. Stolz. 4.35 kW peak power femtosecond pulse mode-locked VECSEL for supercontinuum generation. *Optics Express*, 21(2):1599–1605, 2013.

[44] D. Lorenser, D.J.H.C. Maas, H.J. Unold, A.-R. Bellancourt, B. Rudin, E. Gini, D. Ebling, and U. Keller. 50-GHz passively mode-locked surface-emitting semiconductor laser with 100-mW average output power. *IEEE Journal of Quantum Electronics*, 42(8):838–847, 2006.

[45] A. Garnache, S. Hoogland, A.C. Tropper, I. Sagnes, G. Saint-Girons, and J.S. Roberts. <500-fs soliton pulse in a passively mode-locked surface-emitting laser with 100-mW average power. In *Summaries of Papers Presented at the Lasers and Electro-Optics. CLEO '02. Technical Digest*, pages 586–587, 2002.

[46] A.H. Quarterman, K.G. Wilcox, V. Apostolopoulos, Z. Mihoubi, S.P. Elsmere, I. Farrer, D.A. Ritchie, and A. Tropper. A passively mode-locked external-cavity semiconductor laser emitting 60-fs pulses. *Nature Photonics*, 3:729–731, 2009.

[47] M. Hoffmann, O.D. Sieber, V.J. Wittwer, I.L. Krestnikov, D.A. Livshits, Y. Barbarin, T. Südmeyer, and U. Keller. Femtosecond high-power quantum

dot vertical external cavity surface emitting laser. *Optics Express*, 19(9): 8108–8116, 2011.

[48] D. Waldburger, S.M. Link, M. Mangold, C.G.E. Alfieri, E. Gini, M. Golling, B.W. Tilma, and U. Keller. High-power 100 fs semiconductor disk lasers. *Optica*, 3(8):844–852, 2016.

[49] R. Bek, H. Kahle, T. Schwarzbäck, M. Jetter, and P. Michler. Mode-locked red-emitting semiconductor disk laser with sub-250 fs pulses. *Applied Physics Letters*, 103:242101, 2013.

[50] S. Ranta, A. Härkönen, T. Leinonen, L. Orsila, J. Lyytikäinen, G. Steinmeyer, and M. Guina. Mode-locked VECSEL emitting 5 ps pulses at 675 nm. *Optics Letters*, 38(13):2289–2291, 2013.

[51] A. Kahdour, S. Bouchoule, G. Aubin, J.-C. Harmand, J. Decobert, and J.-L. Oudar. Ultrashort pulse generation from 1.56 μm mode-locked VECSEL at room temperature. *Optics Express*, 18(19):19902–19913, 2010.

[52] A. Rutz, V. Liverini, D.J.H.C. Maas, B. Rudin, A.-R. Bellancourt, S. Schön, and U. Keller. Passively modelocked GaInNAs VECSEL at centre wavelength around 1.3 μm. *Electronics Letters*, 42(16), 2006.

[53] H. Lindberg, M. Sadeghi, M. Westlund, S. Wang, A. Larsson, M. Strassner, and S. Marcinkevičius. Mode locking a 1550 nm semiconductor disk laser by using a GaInNAs saturable absorber. *Optics Letters*, 30(20):2793–2795, 2005.

[54] M. Guina, A. Härkönen, J. Paajaste, J.-P. Alanko, S. Suomalainen, C. Grebing, and G. Steinmeyer. Passively mode-locked GaSb-based VECSELs emitting sub-400-fs pulses at 2 µm. In *Vertical External Cavity Surface Emitting Lasers (VECSELs) II*, volume 8242, pages 21–26, 2012.

[55] H.A. Haus. Mode-locking of lasers. *IEEE Journal of Selected Topics in Quantum Electronics*, 6(6):1173–1185, 2000.

[56] G.J. Spühler, K.J. Weingarten, R. Grange, L. Krainer, M. Haiml, V. Liverini, M. Golling, S. Schön, and U. Keller. Semiconductor saturable absorber mirror structures with low saturation fluence. *Applied Physics B*, 81:27–32, 2005.

[57] U. Keller, K.J. Weingarten, F.X. Kártner, D. Kopf, B. Braun, I.D. Jung, R. Fluck, C. Hönniger, N. Matuschek, and J. Aus der Au. Semiconductor saturable absorber mirrors (SESAMs) for femtosecond to nanosecond pulse generation in solid-state lasers. *IEEE Journal of Selected Topics in Quantum Electronics*, 2(3):435–453, 1996.

[58] M.E. Barnes, Z. Mihoubi, K.G Wilcox, A.H. Quarterman, I. Farrer, D.A. Ritchie, A. Garnache, S. Hoogland, V. Apostolopoulos, and A.C. Tropper. Gain bandwidth characterization of surface-emitting quantum well laser gain structures for femtosecond operation. *Optics Express*, 18(20):21330–21341, 2010.

[59] M. Mangold, V.J. Wittwer, O.D. Sieber, M. Hoffmann, I.L. Krestnikov, D.A. Livshits, M. Golling, T. Südmeyer, and U. Keller. VECSEL gain characterization. *Optics Express*, 20(4):4136–4148, 2012.

[60] R. Paschotta and U. Keller. Passive mode locking with slow saturable absorbers. *Applied Physics B*, 73:653–662, 2001.

[61] D. Lorenser, H.J. Unold, D.J.H.C. Maas, A. Aschwanden, R. Grange, R. Paschotta, D. Ebling, E. Gini, and U. Keller. Towards wafer-scale integration of high repetition rate passively mode-locked surface-emitting semiconductor lasers. *Applied Physics B*, 79:927–932, 2004.

[62] C. Hessenius, M. Lukowski, J. Moloney, and M. Fallahi. Wavelength tuning of VECSELs by cavity geometry. In *Vertical External Cavity Surface Emitting Lasers (VECSELs) II*, volume 8242, pages 68–75. International Society for Optics and Photonics, SPIE, 2012.

[63] D.J.H.C. Maas, A.-R. Bellancourt, B. Rudin, M. Golling, H.J. Unold, T. Südmeyer, and U. Keller. Vertical integration of ultrafast semiconductor lasers. *Applied Physics B*, 88:493–497, 2007.

[64] B. Rudin, V.J. Wittwer, D.J.H.C. Maas, M. Hoffmann, O.D. Sieber adn Y. Barbarin, M. Golling, T. Südmeyer, and U. Keller. High-power MIXSEL: an integrated ultrafast semiconductor laser with 6.4 W average power. *Optics Express*, 18(26):27582–27588, 2010.

[65] M. Mangold, M. Golling, E. Gini, B.W. Tilma, and U. Keller. Sub-300-femtosecond operation from a MIXSEL. *Optics Express*, 23(17):22043–22059, 2015.

[66] R. Paschotta. *Field Guide to Laser Pulse Generation*. SPIE Press, Bellingham, 2008.

[67] H. Kogelnik and T. Li. Laser beams and resonators. *Applied Optics*, 5(10):1550–1567, 1966.

[68] B.E.A. Saleh and M.C. Teich. *Fundamentals of Photonics*. John Wiley and Sons, Inc., Hoboken, 2 edition, 2007.

[69] K-H. Lin, Y. Lai, and W.-F. Hsieh. Simple analytical method of cavity design for astigmatism-compensated Kerr-lens mode-locked ring lasers and its applications. *Journal of the Optical Society of America B*, 12(3):468–475, 1995.

[70] M. Nakazawa, H. Kubota, A. Sahara, and K. Tamura. Time-domain ABCD matrix formalism for laser mode-locking and optical pulse transmission. *IEEE Journal of Quantum Electronics*, 34(7):1075–1081, 1998.

[71] P.A. Bélanger. Beam propagation and the ABCD ray matrices. *Optics Letters*, 16(4):196–198, 1991.

[72] R. Paschotta. Haus Master Equation. `https://www.rp-photonics.com/haus_master_equation.html`, Unknown. Accessed: Mar. 3, 2021.

[73] R. Paschotta, R. Häring, A. Garnache, S. Hoogland, A.C. Trooper, and U. Keller. Soliton-like pulse-shaping mechanism in passively mode-locked surface-emitting semiconductor lasers. *Applied Physics B*, 75:445–451, 2002.

[74] C.H. Henry. Theory of the linewidth of semiconductor lasers. *IEEE Journal of Quantum Electronics*, 18(2):259–264, 1982.

[75] A.M. Weiner. *Ultrafast Optics*. John Wiley and Sons, Inc., Hoboken, 2009.

[76] P.A. Franken, A.E. Hill, C.W. Peters, and G. Weinreich. Generation of optical harmonics. *Physical Review Letters*, 7(4):118–120, 1961.

[77] G.A. Rines, H.H. Zenzie, R.A. Schwarz, Y. Isyanova, and P.F. Moulton. Nonlinear conversion of Ti:Sapphire laser wavelengths. *IEEE Journal of Selected Topics in Quantum Electronics*, 1(1):50–57, 1995.

[78] D. Bauer, I. Zawischa, D.H. Sutter, A. Killi, and T. Dekorsy. Mode-locked Yb:YAG thin-disk oscillator with 41 uJ pulse energy at 145 W average infrared power and high power frequency conversion. *Optics Express*, 20(9): 9698–9704, 2012.

[79] D. Richter, A. Fried, B.P. Wert, J.G. Walega, and F.K. Tittel. Development of a tunable mid-IR difference frequency laser source for highly sensitive airborne trace gas detection. *Applied Physics B*, 75:281–288, 2002.

[80] R.W. Boyd. *Nonlinear Optics*. Elsevier Inc., Oxford, 3 edition, 2010.

[81] P.P. Ho, D. Ji, Q.Z. Wang, and R.R. Alfano. Temporal behavior of cross-phase-modulated second-harmonic generation of ultrashort laser pulses in nonlinear-optical media. *Journal of the Optical Society of America B*, 7(3): 276–284, 1990.

[82] P.E. Powers. *Field Guide to Nonlinear Optics.* SPIE Press, Bellingham, 2013.

[83] M.L. Lukowski. *Novel cavities in vertical external cavity surface emitting lasers for emission in broad spectral region by means of nonlinear frequency conversion.* PhD thesis, The University of Arizona, 2016.

[84] R. Paschotta. *Group Velocity Mismatch*, 2021. `https://www.rp-photonics.com/group_velocity_mismatch.html` [Accessed: April 20, 2021.].

[85] O. Casel, D. Woll, M.A. Tremont, H. Fuchs, R. Wallenstein, E. Gerster, P. Unger, M. Zorn, and M. Weyers. Blue 489-nm picosecond pulses generated by intracavity frequency doubling in a passively mode-locked optically pumped semiconductor disk laser. *Applied Physics B*, 81:443–446, 2005.

[86] R. Bek, S. Baumgärtner, F. Sauter, H. Kahle, T. Schwarzbäck, M. Jetter, and P. Michler. Intra-cavity frequency-doubled mode-locked semiconductor disk laser at 325 nm. *Optics Express*, 23:19947–19953, 2015.

[87] J.T. Meyer, M.L. Lukowski, C. Hessenius, E.M. Wright, and M. Fallahi. High peak power, sub-ps green emission in a passively mode locked VECSEL. *Optics Express*, 28(4):5794–5800, 2020.

[88] M. Oppermann, B. Bauer, T. Rossi, F. Zinna, J. Helbing, J. Lacour, and M. Chergui. Ultrafast broadband circular dichroism in the deep ultraviolet. *Optica*, 6(1):56–60, 2019.

[89] S. Orthaus, M. K"onig, T. Schönau, V. Buschmann, S. Tannert, C. Lauritsen, F. Koberling, U. Ortmann, and R. Erdmann. Crossing the limit towards deep uv. *Trends in Microscopy*, pages 33–36, 2013.

[90] K. Jain, C.G. Willson, and B.J. Lin. Ultrafast deep UV lithography with Excimer lasers. *IEEE Electron Device Letters*, 3(3):53–55, 1982.

[91] F. Rotermund and V. Petrov. Generation of the fourth harmonic of a femtosecond Ti:sapphire laser. *Optics Letters*, 23(13):1040–1042, 1998.

[92] S.C. Kumar, J.C. Casals, E.S. Bautista, K. Devi, and M. Ebrahim-Zadeh. Yb-fiber-laser-based, 1.8 W average power, picosecond ultraviolet source at 266 nm. *Optics Letters*, 40(10):2397–2400, 2015.

[93] N.A. Chaitanya, S.C. Kumar, K. Devi, G.K. Samanta, and M. Ebrahim-Zadeh. Ultrafast deep UV lithography with Excimer lasers. *Optics Letters*, 41(12):2715–2718, 2016.

[94] A.S. Rao, N. A. Chaitanya, and G.K. Samanta. High-power, high repetition-rate, ultrafast fibre laser based source of DUV radiation at 266 nm. *OSA Continuum*, 2(1):99–106, 2019.

[95] S. Hoogland, A. Garnache, I. Sagnes, B. Paldus, K.J. Weingarten, R. Grange, M. Haiml, R. Paschotta, U. Keller, and A.C. Tropper. Picosecond pulse generation with 1.5 μ m passively modelocked surface-emitting semiconductor laser. *Electronics Letters*, 39(11):846–847, 2003.

[96] C. Symonds, J. Dion, I. Sagnes, M. Dainese, M. Strassner, L. Leroy, and J.-L. Oudar. High performance 1.55 μ m vertical external cavity surface emitting laser with broadband integrated dielectric-metal mirror. *Electronics Letters*, 40(12), 2004.

[97] Z. Zhao, S. Bouchoule, L. Ferlazzo, A. Sirbu, A. Mereuta, E. Kapon, E. Galopin, J.-C. Harmand, J. Décobert, and J.-L. Oudar. Cost-effective thermally-managed 1.55-μm VECSEL with hybrid mirror on copper substrate. *IEEE Journal of Quantum Electronics*, 48(5):643–650, 2012.

[98] A. Mereuta, K. Nechay, A. Caliman, G. Suruceanu, P. Gallo, M. Guina, and E. Kapon. 1550-nm wavelength wafer-fused OP-VECSELs in flip-chip configuration. In *Vertical External Cavity Surface Emitting Lasers (VEC-*

SELs) IX, volume 10901, pages 1–8. International Society for Optics and Photonics, SPIE, 2019.

[99] S. Adachi. *Physical Properties of III-V Semiconductor Compounds*. John Wiley and Sons, Inc., New York, 1992.

[100] S. Adachi. Material parameters of $In_{1-x}Ga_xAs_yP_{1-y}$ and related binaries. *Journal of Applied Physics*, 53:8775–8792, 1992.

[101] R.E. Nahory, M.A. Pollack, W.D. Johnston, and R.L. Barns. Band gap versus composition and demonstration of Vergard's law for $In_{1-x}Ga_xAs_yP_{1-y}$ lattice matched to InP. *Applied Physics Letters*, 33:659–661, 1978.

[102] S. Seifert and P. Runge. Revised refractive index and absorption of $In_{1-x}Ga_xAs_yP_{1-y}$ lattice-matched to InP in transparent and absorption in IR-region. *Optical Materials Express*, 6(2):629–639, 2016.

[103] G.P. Agrawal and N.K. Dutta. *Long-Wavelength Semiconductor Lasers*. Van Nostrand Reinhold Company, New York, 1986.

[104] Photonics Research Group. Thin films. `http://fotonica.intec.ugent.be/download/ocs129.pdf`, Unknown. Accessed: 10-1-2019.

[105] F. Zhu, S. Huang, W. Shao, J. Zhang, M. Chen a nd W. Zhang, and J. Zeng. Free-space optical communication link using perfect vortex beams carrying orbital angular momentum (OAM). *Optics Communications*, 396:50–57, 2017.

[106] X. Sun and I.B. Djordjevic. Physical-layer security in orbital angular momentum multiplexing free-space optical communications. *IEEE Photonics Journal*, 8(1), 2016.

[107] T.-L. Wang, J.A. Gariano, and I.B. Djordjevic. Employing Bessel-Gaussian beams to improve physical-layer security in free-space optical communications. *IEEE Photonics Journal*, 10(5), 2018.

[108] R. Chen, H. Zhou, M. Moretti, X. Wang, and J. Li. Orbital angular momentum waves: generation, detection, and emerging applications. *IEEE Communications Surveys and Tutorials*, 22(2):840–868, 2020.

[109] M.L. Lukowski, J.T. Meyer, C. Hessenius, E.M. Wright, and M. Fallahi. Generation of high-power spatially structured beams using vertical external cavity surface emitting lasers. *Optics Express*, 25(21):25504–25514, 2017.

[110] M.L. Lukowski, C. Hessenius, J.T. Meyer, E.M. Wright, and M. Fallahi. High power two-color orbital angular momentum beam generation using vertical external cavity surface emitting lasers. *Applied Physics Letters*, 112, 2018.

[111] M. Padgett, J. Arlt, N. Simpson, and L. Allen. An experiment to observe the intensity and phase structure of Laguerre-Gaussian laser modes. *American Journal of Physics*, 64(1):77–82, 1996.